UNIVERSITY
OF LATVIA

FACULTY OF PHYSICS, MATHEMATICS AND OPTOMETRY

Annamarija Trausa

PROBING METAL AND METAL OXIDE NANOWIRE PHYSICAL PROPERTIES USING *IN SITU* MICROSCOPY NANOMANIPULATION TECHNIQUES

DOCTORAL THESIS

Submitted for the degree of Doctor of Science (Ph.D.) in Natural Sciences
Field of Physics and Astronomy
Subfield of Materials Physics

Scientific advisor:
Dr. phys. **Edgars Butanovs**

Riga 2024

The doctoral thesis was carried out at the Institute of Solid State Physics of University of Latvia and Institute of Physics of University of Tartu, from year 2020 to 2024.

UNIVERSITY
OF LATVIA

Form of the thesis: dissertation in Physics and Astronomy, subfield of Materials Physics.

Supervisor: Dr. phys. **Edgars Butanovs**, University of Latvia, Institute of Solid State Physics, Latvia.

Reviewers:

1) Dr. phys. **Jana Andzane**, University of Latvia, Latvia;
2) Dr. **Tadas Malinauskas**, University of Vilnius, Lithuania;
3) Dr. **Dirk Dietzel**, Justus-Liebig-Universität Giessen, Germany.

The thesis is available at the Library of the University of Latvia, Raina blvd. 19.

Chairman of the Doctoral Committee: Dr. habil. phys. Uldis Rogulis
Secretary of the Doctoral Committee: Sintija Silina

ISBN 978-9934-36-302-3
ISBN 978-9934-36-303-0 (PDF)

ABSTRACT

This Dissertation is dedicated to understanding the mechanical properties and thermal behaviour of one-dimensional nanostructures by implementing diverse nanomanipulation techniques in combination with electron and atomic force microscopies. Key findings include the first-time demonstration of post-synthesis kinking in non-metallic nanowires, determination of the elastic modulus of individual β-Ga_2O_3 nanowires using two different techniques, and exploring Au and Ag nanowire thermal stability under different heating schemes, including Au nanowire heat-induced fragmentation for surface enhanced Raman spectroscopy substrate application. These investigations contribute to a better understanding of the mechanical properties and thermal behaviour of nanowires, highlighting the importance of different manipulation methods and substrate interactions in determining their properties and potential applications.

Keywords: nanowires; nanomanipulations; scanning electron microscopy; atomic force microscopy; heat-induced fragmentation

CONTENTS

LIST OF ABBREVATIONS

0D	Zero-dimensional
1D	One-dimensional
2D	Two-dimensional
3D	Three-dimensional
AFM	Atomic force microscopy
AFS	Atomic force spectroscopy
AM-AFM	Amplitude modulation atomic force microscopy
CTAB	Hexadecyltrimethylammonium bromide
DI	Deionised
EF	Enhancement factor
FEM	Finite element method
FFT	Fast Fourier transformation
MD	Molecular dynamics
MEMS	Microelectromechanical system
NEMS	Nanoelectromechanical system
NP	Nanoparticle
NW	Nanowire
QTF	Quartz tuning fork
SAED	Selected area electron diffraction
SD	Standard deviation
SEM	Scanning electron microscopy
SERS	Surface-enhanced Raman scattering
SPM	Scanning probe microscope
TEM	Transmission electron microscopy
TMAH	Tetramethylammonium hydroxide
VLS	Vapor-liquid-solid
VSS	Vapor-solid-solid
XRD	X-ray diffraction

1. INTRODUCTION

1.1. Motivation

Nanomaterials, characterized by at least one dimension between 1 and 100 nm, represent a remarkable class of materials that exhibit unique properties and behaviours distinct from their bulk counterparts [1]. Through the fabrication of nanostructures, such as nanowires (NWs), nanomaterials achieve exceptionally large surface areas, enabling the development of materials with outstanding mechanical, optical, electrical, magnetic, and catalytic capabilities [2]. These properties make nanomaterials essential across diverse industries, including biomedicine, electronics, energy, and materials science, driving the rapid advancement of nanotechnology [3].

Furthermore, NWs have attracted significant interest due to their potential applications in various fields, including nanophotonics, electronics, and sensing [4]. The emergence of flexible electronics has underscored the importance of characterizing NWs to ensure the reliability of the flexible electronic components [5]. Understanding the mechanical properties and thermal stability of NWs is important for their effective use in these applications, necessitating precise characterization techniques [6]. From a fundamental physics perspective, the small size and excellent material properties of NWs make them an ideal platform for investigating new physical phenomena at nanoscale which are challenging to observe in other types of materials [7].

Despite the challenges posed by their small-scale size, methods such as scanning electron microscopy (SEM) and atomic force microscopy (AFM) manipulations offer valuable insights into NW properties [8]. These imaging and manipulation techniques allow to closely examine the structural and mechanical characteristics of NWs, revealing details that are critical for understanding their behaviour. Additionally, networks of NWs, including those composed of noble metals like Au and Ag, exhibit intriguing phenomena such as spheroidization due to Rayleigh instability induced by heating [9]. Theoretical models and experimental studies aimed at exploring the complexities of NW behaviour are essential for advancing our understanding of nanomaterials and driving innovations in nanotechnology and materials science [10].

Metal and metal oxide NW compounds such as Ga_2O_3, CuO, Ag, and Au have physical properties that are not thoroughly studied and fully understood yet. Investigating these characteristics is essential for the materials applicability thus this Dissertation focuses on studying the physical properties of these promising NW compounds to uncover their full potential and enable their use in diverse applications.

1.2. Objective and tasks

The main **objective** of this work is to investigate mechanical and thermal behaviours of selected material NWs using electron microscopy nanomanipulation techniques and heating experiments.

Tasks have been outlined as follows:

1. To study post-synthesis kink formation in CuO NWs with different mechanical nanomanipulation techniques.
2. To determine elastic modulus of β-Ga_2O_3 NWs using in situ SEM resonance and three-point bending in AFM;
3. To determinate the behaviour of heat-induced fragmentation in Au and Ag NWs under different heating schemes.
4. To study the differences in heat-induced fragmentation between freestanding Ag NWs and those adhered to a substrate.

All the research described in this Dissertation was carried out in Institute of Solid State Physics of University of Latvia and Institute of Physics of University of Tartu.

1.3. Scientific novelty

This Dissertation focuses on understanding the mechanical behaviour of nanostructures through manipulation techniques and observing how heat affects the morphology of nanostructures, providing insights into their behaviour in different conditions. The following findings can be highlighted:

1. Demonstration of post-synthesis kinking in covalent NWs through various manipulation scenarios;
2. Investigation of the elastic modulus of individual β-Ga_2O_3 NWs through two different techniques: *in situ* SEM resonance and three-point bending in AFM;
3. Use of heat-induced fragmentation in Au NWs for surface-enhanced Raman scattering (SERS) substrate applications, supplemented by AFM manipulations to confirm nanoparticle (NP) adhesion to the substrate;
4. Investigation how heat treatment affects pentagonal Ag NWs partially in contact with a substrate, revealing contrasting behaviours between suspended and adhered parts during heating, showing substrate-induced effects beyond Rayleigh instability.

1.4. Contribution of the Author

The direct contribution of the Author is as follows: in **Paper I**, the Author characterised and manipulated CuO NWs using a scanning electron microscope. The Author engaged in discussions and contributed to the analysis of the observed experimental data. Furthermore, in **Paper II**, the Author wrote the main body of the article, characterised NWs and conducted *in situ* SEM resonance measurements, analysed the data and was the corresponding author. Similarly, in **Paper III**, the Author wrote the main body of the article, conducted SEM characterization, and analysed the data, also conducted sample heating experiments with various heating schemes and was the corresponding author of the article. Lastly, in **Paper IV**, the Author contributed to transmission electron microscopy and SEM measurements and participated in heating experiments.

Interpretation of all the obtained results was performed in collaboration with Author's supervisor and all colleagues who were co-authors in aforementioned scientific papers.

1.5. Outline of the Dissertation

This Dissertation is structured in seven chapters. **Chapter 1** is dedicated to outline motivation, the main aim and tasks, scientific novelty and contribution of the Author. **Chapter 2** introduces to the field of nanomaterials, NWs and their mechanical and thermal properties. In **Chapter 3**, various experimental techniques, including electron microscopy and nanomanipulations, are discussed. **Chapter 4** provides information of synthesis of NWs used in this Dissertation along with experimental parameters and equations employed. **Chapter 5** presents the results and discussions, highlighting different manipulation techniques and proposing hypotheses for observed phenomena. **Chapter 6** summarizes the conclusions drawn from all the results, while **Chapter 7** focuses on the Theses. This is followed by a list of publications, summer school and conference attendance, references, and acknowledgements.

2. NANOMATERIALS AND THEIR PROPERTIES

2.1. Nanomaterials

A wide variety of materials with at least one dimension between 1 and 100 nm represent the remarkable class of materials known as nanomaterials [1]. By creating nanostructures, exceptionally large surface areas can be attained. It is possible to create nanomaterials with outstanding mechanical, optical, electrical, magnetic, and catalytic capabilities that differ significantly from their bulk counterparts. By precisely adjusting the size, shape, synthesis parameters, and suitable functionalization, the properties of the nanomaterial can be specifically tailored to the desired results and applications [2]. Nanomaterials are used in a wide range of industries, including biomedicine, agriculture, electronics, energy, coatings, materials, food engineering, telecommunication, transportation, cosmetics, and mechanical engineering. The development, engineering, and use of nanostructures are all included in the scientific field known as nanotechnology. Nanotechnology has drawn a lot of attention throughout the years because of the fascinating and inventive uses of nanomaterials for the future industrial generation [3].

Nanostructures can be categorized based on their dimensions (Figure 2.1.), referring to the number of dimensions at the nanoscale. The classification includes zero-dimensional (0D), one-dimensional (1D), two-dimensional (2D), and three-dimensional (3D) nanomaterials [11].

0D materials are either non-dimensional outside of the nanometric range or have all three dimensions (x, y, and z) within the nanoscale range. This category includes quantum dots, fullerenes, and NPs, which display a diverse variety of forms and geometries, including metallic or ceramic compositions [3, 12].

1D materials have one dimension outside the nanometric range, but two of their three dimensions are within the nanoscale range. This type of nanomaterials includes NWs, nanotubes, whiskers and nanofibers. Moreover, they can be chemically pure or impure and may be embedded within other materials like metallic, ceramic, or polymeric matrices, allowing for the formation of polymeric, ceramic, or metallic 1D nanostructures [3, 13].

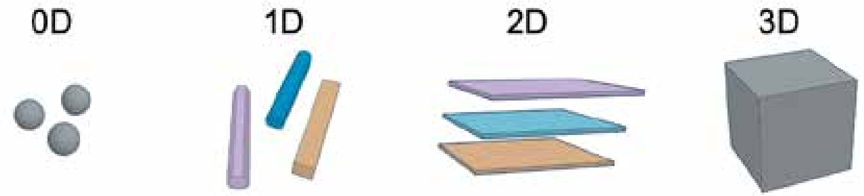

Figure 2.1. Classification of nanostructures based on their dimensions.

2D nanomaterials feature plate-like forms with two dimensions outside the nanometre range. This category encompasses a variety of materials such as coatings, thin-film multilayers, nanosheets, nanowalls, free particles, tubes, fibres, ultrafine-grained layers, and platelets. It is possible for 2D nanomaterials to consist of diverse chemical compositions. Additionally, they can be coated onto substrates, integrated into surrounding matrix materials, and exist in metallic or polymeric forms [3, 14].

Materials that are not limited to the nanoscale in any dimension or range of dimensions are known as 3D nanomaterials. Although each dimension of a 3D material lies beyond the nanoscale or surpasses 100 nm, it encompasses various structural elements, including dispersed NPs, bundles of NWs and nanotubes, and multi-nano layers. These materials exhibit interfaces formed by the interaction of 0D, 1D, and 2D components. 3D nanomaterials encompass diverse forms such as free NPs with varied morphologies, and thin films characterized by atomic-scale porosity [3, 15].

2.2. Nanowires

NWs represent a class of nanostructures that has attracted significant interest in research over the past few decades [16]. Typically, a NW is a structure that is quite restricted in the other two directions and extends in the longitudinal direction [17]. NWs can be classified as metallic, semiconducting, or dielectric based on their chemical compositions and electronic characteristics. Metallic and dielectric NWs are good for plasmonic and photonic waveguiding applications, while semiconducting NWs show promise for light production and sensing applications [18, 19], nanophotonics [4], electronics [20] and many more. Furthermore, from a fundamental physics perspective, the small size and excellent material properties of NWs make them an ideal platform for investigating new physical phenomena at nanoscale which are challenging to observe in other types of materials [7].

Considerable research endeavours have been dedicated to understanding NW growth at the atomic scale and accurately managing various aspects such as NW dimensions, crystal structure, composition, growth pattern, and structural or compositional complexity [19]. NWs can be fabricated using “top-down” methods like conventional lithography, but they are more commonly grown through “bottom-up” approaches such as solution growth, template-guided synthesis, and the vapor-liquid-solid (VLS) process, which are typically more cost-effective [21].

The most common way for achieving anisotropic growth on the nanoscale involves using metal NP catalysts, which can exist in either the solid or liquid phase during NW growth conditions. Gaseous precursors, supplied in molecular or atomic form, are selectively adsorbed and decomposed by these metal NPs. As the NPs reach supersaturation, the precursor components precipitate beneath them. The continuous transport of precursor components from the gas phase through the catalysts to the growing solid crystals below results in the formation of NWs, with their diameters determined by the size of the catalyst. The state of the NP catalyst, whether liquid or solid, dictates whether growth occurs via the VLS or vapor-solid-solid (VSS) mechanisms [4].

VLS method involves three key stages: alloying, nucleation, and growth [19]. In the VLS process, a seed particle accumulates atoms and guides the nucleation of crystalline material. Adjusting the delivery of growth species or conditions allows for compositional and structural manipulation [22]. However, numerous challenges persist: certain desired structures are currently beyond reach, and even for achievable ones, the parameter range (such as temperatures and pressures) is often limited. Nonetheless, the flexibility of VLS growth allows for the fabrication of various functional devices [23].

2.2.1. Ga_2O_3 nanowires

Expected to be key in future electrical and optoelectronic devices, semiconducting NWs offer a platform for investigating nanoscale phenomena [7]. Metal oxide NWs represent a pivotal group of semiconductor NWs due to their significant electrical, optical, and chemical sensing properties [24]. In recent years, significant advancements have been made in the field of both material and device technologies concerning monoclinic gallium oxide (β-Ga_2O_3) [25–27]. The attention of researchers has been directed towards it due to its outstanding properties [28] such as chemical stability and ultra-wide band gap (4.4–4.9 eV) [29, 30]. Ga_2O_3 is a promising candidate for power devices and optoelectronics [31–34], visible-blind UV-light sensors [28], memory devices [33] and gas sensors [35]. These applications can be downscaled to the nanoscale, including flexible nanodevices, aligning with the current trend in electronic technologies emphasizing the development of adaptable electronic devices [36, 37]. Consequently, understanding the mechanical properties of β-Ga_2O_3 NWs becomes crucial. However, minimal research has been dedicated to exploring and understanding the mechanical properties of β-Ga_2O_3 NWs. In the current literature, only a single NW and nanoribbon of β-Ga_2O_3 have been measured to determine the bending modulus, exhibiting a value of approximately 300 GPa, highlighting the need for further measurements [38].

2.2.2. CuO nanowires

Metal oxide NWs like copper oxide (CuO), known for their high optical absorption coefficient and the lowest band gap energy among metal oxides, hold promise as materials for visible light photodetectors, offering transparency and flexibility. The optoelectrical properties of CuO, such as its bandgap range and surface depletion layer for charge capturing, can be tailored for specific applications due to the ease of nanofabrication of the material. This makes CuO NWs suitable for a wide range of uses, including multispectral detection and molecular/thermal imaging. Additionally, the inherent chemical and mechanical stability, along with cost-effectiveness, make CuO a reliable choice for industrial applications [39].

P-type CuO NWs are widely acknowledged as catalysts and have attracted significant interest for various applications, including sensors and nanoelectronics [40]. Studies have revealed that mechanical properties of CuO NWs have been found to be predominantly elastic up to a critical strain, beyond which they undergo brittle fracture [41, 42]. Moreover, investigations have uncovered more unique mechanical properties, such as the anelastic behaviour observed in axially twinned CuO NWs during bending tests within a TEM. This behaviour has been attributed to the cooperative motion of atoms associated with twinning [43]. However, no previous research has explored plastic deformation through mechanical manipulation of initially straight, thermally grown CuO NWs post-synthesis. This represents a new area of study, highlighting the potential for discovering additional unique mechanical behaviours in CuO NWs.

2.2.3. Au and Ag nanowires

Metal nanostructures, such as Ag and Au, including NWs, are a topic of intense interest. Surface plasmons, or collective electronic oscillations, are the primary optical property of these noble metal nanostructures [44]. Au NWs stand out among various materials due to their easy synthesis, precise geometry, and outstanding electrical, optical, and chemical properties. They are employed in numerous applications, including biosensors, catalysts, gas sensors, mechanical energy storage and release, flexible electrodes, and SERS [45].

One of the applications of noble metal NWs in plasmonics, is in the fabrication of substrates for SERS. It is an ultrasensitive detection method, capable of providing fingerprint information of small molecules and even single molecule detection [46]. When compared to regular Raman signals, SERS significantly boosts Raman signals by a factor of up to 10^{14}. Due to this remarkable enhancement caused by the strong light-induced electric field at certain regions within the metallic nanostructured space, sometimes referred to as "hot spots", SERS is an appealing high-sensitivity and selectivity detection technique for the target analytes [47]. Numerous nanofabrication techniques have been utilized to create highly ordered SERS substrates, including electron beam lithography, electro-oxidation lithography, UV photolithography, nanoimprint lithography, and self-assembly [28]. However, exploring alternative methods to utilize metal NWs and their thermal behaviour could offer new opportunities for creating cost-effective SERS substrates.

Metal NWs also offer both electrical conductivity and sufficient transparency when arranged on a transparent substrate in the form of a low-density mesh. The growing demand for transparent conductive materials has prompted extensive research efforts focused on the design, synthesis, and characterization of such materials [48, 49]. Among the various materials investigated for NW-based transparent electrodes, Ag NWs stand out as one of the most extensively studied due to their ability to be synthesized in large quantities with precise control over their length and diameter [50, 51]. Ag NW networks find application in highly flexible transparent film heaters [52] and have also attracted interest as a fundamental component in neuromorphic computing devices in recent years [53]. In the context of the applications above, Ag NWs experience increased temperatures due to Joule heating [54]. Besides, elevated temperatures can lead to the fragmentation of NWs into shorter segments, often explained by Rayleigh instability and energy minimization through spheroidization [55, 56]. A deeper understanding of the heat-induced behaviour of Ag NWs under different conditions and on various substrates could enhance control over cost-effective production methods for novel applications involving arrays of metal nanostructures.

2.3. Structure

Almost every aspect of a material, including its qualities, prospective uses, and performance in those uses, is determined by its structure, or the configuration of its internal components. The amount of information needed to explain a substance is reflected in how simple or complex its structure is [57]. Translational symmetry – also known as "periodicity" or "long-range order" – determines the length scale over which atoms are related to one another in single crystal, polycrystalline, and amorphous solids. Amorphous materials lack long-range order, polycrystals have local periodicity, and single crystals have infinite periodicity. The structural differences between these three kinds of solids can be used to explain a wide range of typical material properties, including mechanical, optical, magnetic, and electronic behaviour [58].

A single crystal is produced in a crystalline solid when the periodic and repeating arrangement of atoms is perfect or continuous throughout the specimen. Every unit cell has the same orientation and interlocks in the same way. Although they can be created artificially, single crystals can also be found in nature. Usually, they are challenging to develop since the atmosphere needs to be properly managed. If the extremities of a single crystal are allowed to develop unhindered by any external force, the crystal takes on a regular geometric shape with flat faces – this shape is representative of the crystal structure. In recent years, single crystals have gained significant importance in numerous modern technologies, especially electrical microcircuits that utilize Si and other semiconductor single crystals [59].

A crystalline defect refers to an irregularity within the lattice structure, typically spanning one or more dimensions approximately equivalent to an atomic diameter. These imperfections are commonly classified based on the geometry or dimensionality of the defect. Various imperfections exist within crystalline structures, including point defects, which involve one or two atomic positions, linear defects of a one-dimensional nature, and interfacial defects, also known as boundaries, which manifest in two dimensions. Structural defects are inherent in real materials regardless of chemical impurities. Point defects in crystalline lattices are common imperfections. They typically manifest as vacancies, where an atom site within the crystal lattice is unoccupied, or as interstitials, where an atom occupies a site not usually filled or an extra atom is inserted into the lattice [59]. Point defects, such as oxygen vacancies, have the potential to impact the mechanical properties of one-dimensional nanomaterials. Specifically, oxygen vacancies can lead to an increase in the average bond length, consequently resulting in a decrease in the elastic modulus [6, 60, 61].

One-dimensional linear defects, known as dislocations, are closely associated with mechanical deformation. Edge and screw dislocations represent the two extremes of linear defect structure, although actual materials often contain mixed forms of linear defects. Additionally, the finite quantity of material available is bounded by surface boundaries, which themselves disrupt the atomic arrangement. Among these disruptions are planar defects, such as twin boundaries and stacking faults, which are two-dimensional in nature. Twin boundaries, for instance, divide crystalline regions that mirror each other structurally [59], and are prevalent in metallic. Twin boundaries are formed through processes like deformation twinning, annealing, growth, or phase transition [62]. A stacking fault is a type of planar defect characterized by atomic layers with modified stacking sequences, typically observed in crystal structures with close-packed arrangements of atoms. Recent research indicates that a significant rise in the density of stacking faults can notably impact the mechanical properties of metallic or ceramic materials, often exerting a dominant influence in certain scenarios [63].

A specific type of defects – referred to as kinks – are abrupt shifts in a NW's axial growth orientation [64], and commonly consist of a twin boundary. Kinking commonly occurs in the synthesis of NWs using methods that employ metal catalyst NPs for one-dimensional growth, such as chemical vapor deposition, molecular beam epitaxy, and laser ablation. These kinds of procedures involve the introduction of gaseous precursors, either molecular or atomic, into the reactor, where they accumulate and, in the case of a molecular precursor, break down on metal NPs [22].

NW growth direction is determined by surface free energy, favouring directions that minimize it. Various factors like pressure, temperature, and chemical composition of the reactor atmosphere influence growth direction during synthesis. Kinking can result in a uniform or altered crystallographic orientation of the NW. Typically, kinks occur between growth directions specific to the material's one-dimensional forms. For instance, Si NWs have many possible growth directions, leading to a wide range of specific kinking angles, however, all these can be linked to different combinations of {111} twins [65].

Generally, the properties and functionalities of NWs can undergo modification through the introduction of various defects such as dopants, oxygen vacancies, nanotwins, and kinks. Kinked NWs, in particular, are gaining increasing attention due to their potential applications as building blocks in electronic and nanomechanical devices, alongside their reported enhancement in mechanical durability. Advanced synthesis techniques for semiconductor NWs provide substantial control over the occurrence and number of kinks by fine-tuning growth parameters like temperature, gas pressure, and composition [66].

Kinks, much like other defects, can considerably worsen the fundamental characteristics of NWs, making straight and defect-free NWs generally preferred for the majority of applications. However, kinks can also provide an additional means of controlling NW properties and can even introduce entirely novel characteristics. Recently, kinked NWs have attracted growing interest in due to their potential applications in integrated electronic devices, nanoelectronic bioprobes, nanoscale springs, and more [22]. Kinking frequently occurs in semiconductor NWs such as Si, GaAs, GaSe, and Ge during synthesis rather than post-synthesis, leading to changes in their properties, thereby holding practical significance [67]. In contrast, metal NWs commonly exhibit a reversible cyclic deformation mechanism involving twinning and detwinning under tensile and compressive loading, respectively, which can occur post-synthesis and accommodates large strains, enabling ultra-high strength and ductility [68, 69].

The closest experiments related to the kinking of NWs include recent findings in structural defects and mechanical behaviour of nanoscale covalent materials, which have revealed unique and fascinating mechanical properties not observed in their bulk forms [70]. For instance, Östlund et al. [71] discovered the ductility of micromachined Si pillars comparable to that of metals in compression tests at room temperature, with Si sample sizes reduced below 300 nm. Similarly, Wu et al. [72] reported a transition from brittleness to plasticity during compressive deformation at room temperature in monoclinic β-Ga_2O_3 single crystals, with pillar sizes reduced below 800 nm.

The crystallographic orientation of the micropillars was found to be crucial for observing plasticity at small scales. Additionally, Mignerot et al. [73] observed plastic deformation of InSb micro-sized pillars during micro-compression tests at room temperature, leading to stress-induced nano-twin formation. These studies represent significant advancements in understanding plastic deformation in non-metallic materials at the micro- and nanoscale, providing a foundation for future research and application. To further reduce specimen size, a convenient alternative is the direct synthesis of nanostructures, particularly NWs.

2.4. Mechanical properties

As particle size approaches atomic dimensions, certain physical and chemical characteristics of matter can undergo significant transformations. For instance, materials that appear opaque at the macroscopic level may become transparent at the nanoscale. Some solids may transition into liquids, chemically stable substances can become combustible, and electrical insulators may transform into conductors. Additionally, properties within the nanoscale domain often depend on size. These effects stem from a combination of quantum mechanics and surface phenomena – as particle size decreases, the proportion of atoms located on surface sites increases substantially [59].

The characteristics of materials to diverse external stresses and conditions are referred to as their mechanical properties. The mechanical properties of different materials vary. In conventional materials, strength, brittleness, plasticity, toughness, hardness, elasticity, fatigue strength, rigidity, ductility, and yield stress are the ten primary components of mechanical properties in metals. The majority of non-metallic inorganic materials are brittle, lacking attributes like elasticity, toughness, ductility, and plasticity. Furthermore, certain organic materials lack stiffness and brittleness and are flexible instead [74].

Nanomaterials find wide-ranging applications across various domains, with these applications extending down to the nanoscale, including the development of flexible nanodevices and nanoelectromechanical systems (NEMS). Various types of NWs hold promise for deployment on bendable substrates, aligning with the prevailing trends in electronic technologies that emphasize the advancement of flexible electronic devices. Consequently, comprehending the mechanical properties of NWs emerges as a crucial undertaking. For example, precisely determining the elastic modulus is vital for the design of semiconductor NW-based nanomechanical resonators or flexible field-effect transistors [75–78].

Researchers are focusing their experimental efforts on altering nanomaterials, and enhancing their mechanical characteristics [74]. Property improvements are anticipated in areas like impact resistance, fracture, bending strength, Young's modulus, and tensile strength. A thorough examination of the mechanical properties of nanomaterials requires consideration of various factors that directly influence them, including surface structure, porosity, functionalization, fabrication techniques, chemical treatments, and more. Additionally, the underlying material composition and its defects also impacts the mechanical characteristics [75].

For nanostructures to continue to perform as multifunctional materials, their structural integrity must be retained [75]. Over the last decades, various methods have emerged to analyse the mechanical properties of NWs, with certain approaches becoming widely adopted. These techniques encompass direct measurements like bending, uniaxial loading, and indenting, alongside indirect approaches such as vibration. Unlike testing bulk materials, assessing NWs relies heavily on the experimental arrangement, with the manipulation process posing notable challenges due to their diminutive size [6]. For instance, the elastic properties of NWs can be assessed using various conventional techniques for mechanical characterization of 1D nanostructures. These methods include the tensile test, resonance method, cantilevered beam bending, three-point bending, nanoindentation, buckling, and contact resonance AFM (see *Figure 2.2*) [79].

AFM offers the capability to measure the force-displacement response of a small probe in contact with a surface with exceptionally high resolutions. Consequently, AFM has emerged as a valuable tool for assessing the mechanical properties of NWs. Direct AFM-based measurements, such as AFM bending and contact resonance tests, have seen widespread usage in characterizing the mechanical properties of NWs in recent times [6]. For instance, the AFM three-point bending technique has been widely employed due to its convenient manipulation for determining the Young's modulus of 1D nanostructures [80–82]. In the AFM three-point bending technique, a NW is secured across a trench using either a polymer adhesive, an electron beam-induced deposition process, or through self-adhesion between the wire and substrate. The AFM tip applies force to the midpoint of the suspended NW. The wire's Young's modulus is determined by recording the applied force and the accompanying deflection, or displacement in the z direction, at the halfway point [80].

Furthermore, incorporating an AFM, a nanoindenter, nanomanipulator, or microelectromechanical system (MEMS) device into an electron microscope, either SEM or

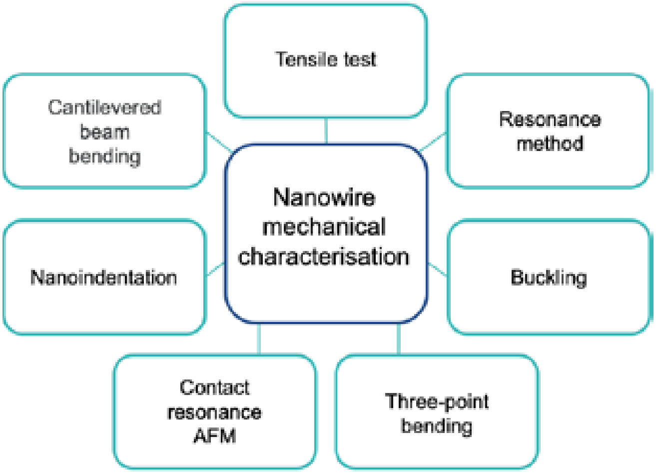

Figure 2.2. Experimental test methods for mechanical characterisation of NWs.

transmission electron microscopy (TEM), enables the visual monitoring of the testing process. These systems, known as *in situ* electron microscope testing setups, facilitate the real-time observation of atomic-scale deformation of NWs under load. Therefore, *in situ* techniques serve as powerful tools for comprehending the mechanical properties of NWs [6].

2.4.1. Elasticity

The way a material reacts or deforms when subjected to an external force or load is indicative of its mechanical behaviour. If a load remains constant or changes gradually over time, and is evenly distributed across a materials cross-section or surface, the mechanical response can be evaluated through a straightforward stress-strain test. Load application typically occurs in one of three primary modes: tension, compression, or shear [59].

One of the frequently conducted mechanical stress-strain tests involves tension. In this test, a specimen is subjected to deformation, often until it fractures, by applying a gradually increasing tensile load along the longitudinal axis of the specimen in a uniaxial manner. A compression test is conducted similarly to a tensile test, with the difference being that the force is compressive, causing the specimen to contract along the direction of the stress. Shear occurs when forces are applied parallel to an object's or material's surface, causing material layers to slide past one another and deform the object. However, when forces are applied in a way that causes an object to twist or rotate about its longitudinal axis, this is known as torsion [59].

Comprehending the elastic behaviour of nanostructures holds significance not only for potential applications but also for providing insights into the structure of NWs obtained through various synthesis methods. Several approaches have been employed to investigate the mechanical behaviour of NWs, including AFM three-point bending tests and nanoindentation. Among these methods, *in situ* techniques stand out due to their capability of real-time monitoring of the elastic response of NWs. Bending tests utilizing external force sensors, tensile deformation, as well as mechanical and thermal resonance, have all proven effective in determining mechanical properties. These techniques enable the measurement of elastic parameters such as hardness and Young's modulus, as well as the exploration of individual NWs' plasticity [83].

Characterizing the mechanical properties of NWs poses challenges due to the need for precise manipulation at the nanoscale. Evaluating the Young's moduli requires precise measurement of individual NWs, as they may demonstrate size-dependent behaviour due to defects and surface stress. Although it is difficult to measure the mechanical properties of NWs directly, there are a number of indirect techniques that can be used to gain insightful knowledge. For example, *in situ* electron microscopy offers the capability to determine Young's moduli through mechanical resonance, while AFM enables the use of bending tests to assess individual NW properties. These techniques are invaluable for advancing understanding of NW mechanical behaviour and properties [8].

2.4.2. Adhesion

Adhesion involves the molecular interactions between materials at their interfaces. Adhesion essentially describes the coming together of an adherend and an applied adhesive, forming an intervening interface. This combination defines what is known as an adhesive joint, which often comprises multiple interfaces, adding complexity to the joint structure. Adhesion or cohesion can be classified based on the physical, chemical, and/or mechanical bonding mechanisms contributing to the strength of the interface in the assembly. It's important to note that bonding occurs within the adherend, within the adhesive, and between the two at the interface [84].

Physical bonding forces are typically weak, while chemical bonding is strong but challenging to achieve uniformly across an interface. Physical adhesion or bonding, although inherently weak, is consistently present. Therefore, while van der Waals forces are prevalent at every interface, they are frequently reinforced by stronger bonds, such as those originating from permanent dipoles, in addition to the van der Waals-induced dipoles. Chemical bonding, on the other hand, encompasses options such as covalent, ionic, and metallic bonding [84].

Adhesion is a critical factor for nanostructures, especially in situations like the adherence of NWs to substrates post optical or laser processing, which is vital for the device fabrication [85]. Moreover, it is widely recognized that the adhesion and static friction of metal nanostructures decrease notably after annealing, primarily due to the rounding and reduction of the contact area with the substrate. The application of AFM manipulation techniques proves effective in assessing the magnitude of adhesion/static friction and estimating the portion of movable NPs. For instance, during the drop-casting of the chemical solution under investigation, these NPs may be displaced or removed due to capillary forces. This understanding becomes crucial, particularly when exploring methods like heat-induced NW fragmentation, which holds potential for the creation of SERS substrates [86].

Adhesion also plays a critical role in flexible electronics for the components to remain reliable and intact [5]. The emergence of flexible electronics has opened up a wide range of possibilities for their extensive integration into various sectors of smart electronics, such as artificial e-skin, flexible touch sensors, health monitoring systems, implantable devices, and more [87]. Flexible electronics encompass a distinct category of thin-film electronic devices capable of maintaining relatively consistent electrical performance even under mechanical bending, folding, twisting, compression, and stretching [5].

A typical experimental configuration for evaluating the adhesion and mechanical characteristics of nanomaterials involves applying controlled pressure with a hard, spherical probe onto a soft, flat sample using AFM. This setup allows for the measurement of interaction force and probe displacement. As the probe approaches the sample, the interaction force between the probe and sample remains constant at zero. Upon penetration of the sample by the probe, a circular deformation occurs at the contact point, which amplifies with external loading. Force-increasing (indentation) curves yield insights into the mechanical properties of the sample. During the retracting phase, the probe remains attached to the surface until the pull-off force exceeds the adhesion force. This pull-off force can serve as an indicator of adhesion strength. Typically, the measured data is simplified to the magnitudes of preload and pull-off forces. It's worth noting that the attractive force on the probe as it approaches the surface is often much lower than the pull-off force, attributed to the non-adiabatic conditions of the experiment [88].

2.5. Thermal properties

Thermal properties, encompassing thermal expansion and heat capacity, describe how materials react to temperature changes. When solids absorb heat, their temperature rises, causing expansion, while temperature variations within the material can lead to mechanical stresses, heat transfer and potential melting. These properties are essential for the practical application of solids [59]. When discussing the thermal treatment of nanostructures, it is crucial to note that the behaviour of metal nanostructures at elevated temperatures varies considerably from that of their bulk counterparts, being dependent not only on material but also on size and shape [89, 90].

It is widely recognized that the melting point of metal nanostructures decreases as their size and dimensionality reduce, often reaching much lower temperatures compared to bulk materials [91]. Over time, surface diffusion can cause drastic morphological changes in nanostructures even at moderate temperatures. For example, a 5 nm Au NP begins to melt at approximately 830 °C, whereas particles over 10 nm melt at temperatures comparable to bulk values (1064 °C). Additionally, processes like surface diffusion and Rayleigh instability can lead to the fusion and fragmentation of Au nanostructures at temperatures as low as 200 °C. This behaviour is crucial for applications where NWs are exposed to high temperatures or require thermal treatment, such as in the preparation of NW-based transparent conductive coatings [92].

When heated, Au and Ag NWs can spheroidize due to Rayleigh instability, a phenomenon observed in both fluids and specific metallic nanostructures, driven by the minimization of surface area through surface tension. It leads to fragmentation of NWs into NPs [9]. This instability, initially studied in fluids and extended to solid NW systems, explains morphological changes in NWs, with surface curvature playing a critical role in predicting breakdown and shape alterations [10]. Studies have validated applicability of this model by annealing Cu NWs on Si substrates, aligning with the model's predictions of the beading phenomenon [93].

Recent studies investigating the thermal behaviour of Au NPs, have revealed that when subjected to annealing experiments at progressively higher temperatures, these NPs undergo a notable transformation in shape, transitioning from irregular faceted shapes to more rounded ones. This phenomenon is believed to occur due to a process driven by diffusion, aiming to minimize the surface energy of the particles. Additionally, experiments using AFM to manipulate these particles have shown that higher annealing temperatures generally lead to increased particle mobility [94]. This could pose a significant challenge to the long-term reliability of NW-based components, prompting the exploration of various methods to mitigate Rayleigh instability. Conversely, if the morphological changes driven by instability can be controlled, they could offer a promising nano-patterning approach [95].

3. EXPERIMENTAL TECHNIQUES

3.1. Scanning electron microscopy

3.1.1. Principles of electron microscopy

The resolution of optical microscopy is typically restricted by the wavelength of light that strikes the substrate. Since these wavelengths are on the order of hundreds of nanometres, even in the ultraviolet, electron beams have long been used as an alternative to examine structural detail at the smallest scale. Electrons are quite good at spatial resolution, but they cannot be compressed in time as a light pulse. For this reason, electron microscopy has historically been a somewhat static characterization technique [96]. A thorough knowledge of the structure of materials has been made possible by electron microscopy, which goes beyond the diffraction limit of light microscopy. Due to the strong interaction between accelerated electrons and matter, electron microscopy requires imaging under high vacuum conditions [97].

Focused accelerated electrons are used in electron microscopy to look through samples and scan materials on a very small and fine scale. This process yields higher magnification, resulting in images with superior resolution [98]. When the electron beam interacts with the specimen, it reveals important details about its composition, crystalline structure, size and shape of features, and surface characteristics. As it is schematically shown in *Figure 3.1,* the electron beam interacts with the specimen in various ways. One way is interaction with secondary electrons – the incident electrons will transfer part of their energy to the specimen electrons, primarily in the K-shell, if they approach the atom closely enough. As a result, these electrons change their trajectory and ionize the electrons in the atoms of the sample. The ionized electrons will go toward the specimen's surface, where they will collide inelastically and elastically until they dissipate their energy. However, because of their low energy of about 5 eV, only electrons that are near the surface (less than 10 nm) would be able to escape, making them detectable and useful for imaging the specimen's topography. Another mechanism involves the interaction with backscattered electrons, where electrons are reflected or backscattered upon directly striking an atom. As the atomic number of the specimen changes, different atomic types will cause varied rates of backscattered electrons, which will change the contrast of the image. Generally, atoms with higher atomic numbers will seem brighter than those with lower atomic numbers. Lastly, transmitted electrons, which are utilized to create an image of a thin specimen, are those that are created when incident electrons travel through a specimen without interacting with their atoms. Elastic scattering is a different type of scattering where electrons retain their energy and can be used to gather information about the arrangement and orientation of atoms [99, 100].

The excitation of an atom occurs when incident electrons collide with it, causing the release of electrons from the atom. To return to its ground state, the atom must dissipate the excess energy. Three relaxation mechanisms include cathodoluminescence, X-rays, and Auger electrons. Using a method known as energy dispersive X-ray

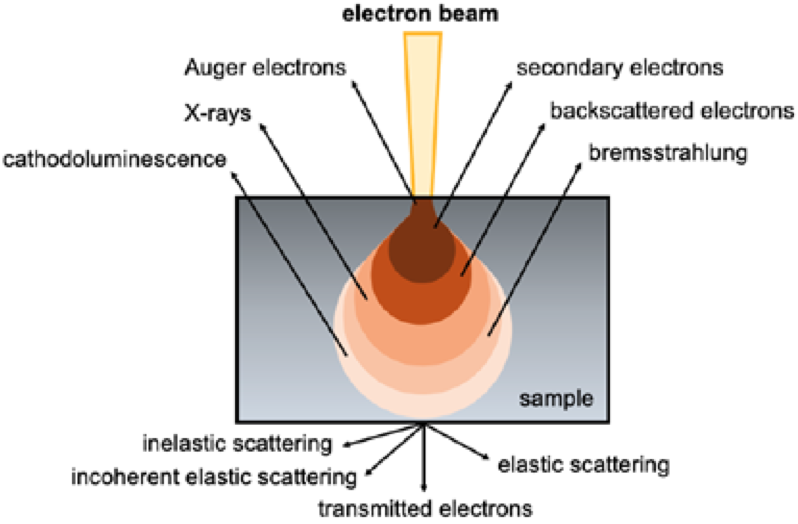

Figure 3.1. Electron beam interaction with matter. Adapted from [101].

analysis, the elements and their concentrations in the specimen are determined by x-ray analysis. Auger electrons can be used for chemical analysis [99].

An SEM is a specific type of electron microscope that uses a concentrated electron beam to scan a surface and create images of the material. The sample's atoms and electrons interact to produce a variety of signals that reveal details about the sample's composition and surface topography. An image is created by combining the intensity of the detected signal with the position of the electron beam as it scans in a raster scan pattern [99].

3.1.2. Nanomanipulations

Micro/nanomanipulation and assembly encompass applications ranging from the micrometre to submicrometric and nanometre scales. These crucial techniques have seen widespread utilization over the past decade in various fields such as micro/nanostructure assembly and material characterization [102]. Nanoscale manipulation experiments serve two primary objectives. They facilitate the exploration of material frictional, mechanical, and other properties at the nanoscale. Simultaneously, these experiments offer practical benefits by enabling precise 2D positioning and assembly of nanostructures, which are crucial for various nanotechnological applications such as nanoelectronics, NEMS, digital information storage, and more [103]. Manipulations are achievable in both electron microscopes as well as AFM setups.

Micromanipulation involves either transporting pre-existing objects, which were created using other techniques, for investigation purposes, or assembling complex structures from basic components. This category of micromanipulation techniques pertains to manipulation within electron microscopes. Unlike optical tweezers or scanning probe microscopes, electron microscopes don't have the same limitations. Micromanipulation in SEMs and TEMs enables the handling of individual micro-objects and nanoobjects with nanometer precision, with both the process and results of manipulation visible in high resolution and real-time. Furthermore, we can categorize micromanipulation techniques involving electron microscopes into three main groups. Mechanical manipulation involves the use of micromanipulators within the electron microscope chamber, where a probe tip makes mechanical contact or adhesion with the object. Electrostatic manipulation relies on the electrostatic interaction between objects charged under electron beam illumination. Electromagnetic manipulation, on the other hand, utilizes the impact of an electromagnetic force produced by a passing electron beam [104].

Manipulations can also be conducted in AFM. However, AFM manipulations encounter specific constraints. Firstly, there's a lack of real-time visual feedback regarding the contact geometry or the particle's position and behaviour during manipulation (such as rolling or sliding). Conclusions can only be drawn indirectly based on the shape of force curves. Additionally, many AFM experiments are conducted under ambient conditions, where a significant amount of water is present on all investigated surfaces, complicating the interpretation of forces [103].

Another challenge arises from the "ageing" of samples when exposed to ambient conditions, leading to particle sticking to the substrate. This adhesion progressively intensifies over time, which is particularly problematic during time-consuming AFM manipulation experiments, where adhesion may even increase within a single experimental series. To address these challenges, manipulation experiments should ideally be conducted in a vacuum environment with real-time visual monitoring. One effective approach involves employing dynamic mode within an SEM, utilizing a quartz tuning fork (QTF)-based force sensor mounted on a 3D nanomanipulator [103, 105, 106].

3.1.2.1. Stepper motors and piezoelectric actuators

Manipulator drives incorporate stepper motors that execute continuous motion in response to a series of electrical pulses for control. One notable characteristic of these motors is their ability to position without requiring feedback sensors. Despite their advantages, step drives come with limitations that considerably constrain their utility, including issues such as vibration, resonance, limited dynamics, locking torque, high temperatures, reduced efficiency, and lower positioning accuracy [107].

Research indicates that when a stepper motor operates under real-world conditions with a load and lacks a position sensor, the control system lacks accurate knowledge of the rotor's current position. This discrepancy can result in the actual position deviating from the preset position due to step skipping. In systems without feedback, to mitigate step skipping, a strategy of smooth acceleration and braking with a significant safety margin is employed. However, this approach limits the potential dynamic capabilities of the drive [108].

The motor windings remain energized even in the absence of a load, leading to increased energy consumption, reduced efficiency, and higher operating temperatures. To address this challenge associated with step drives and meet new movement accuracy requirements, a novel control method called vector control has gained popularity. The occurrence of step skipping is addressed by integrating a position sensor into the drive. The fundamental principle of vector control is to maintain a consistent rotor flux linkage vector. This involves applying voltage to both phases A and B, where the phase currents generate the resultant stator current. Accurate calculation of the current angle and precise current control are crucial, requiring the use of an electronic processor operating at a high frequency [107].

Piezoelectric positioning components find widespread use in precision displacement applications, notably in devices like SEM [109]. Piezoelectric actuators find extensive application across scientific and technical domains due to their swift responsiveness, substantial range of motion, fine resolution, and easy manageability. Nevertheless, the occurrence of backward motion, a common issue in various piezoelectric actuators such as inertial impact, stick-slip, and parasitic motion, imposes limitations on their further advancement for both scientific and industrial purposes. This phenomenon may diminish the accuracy and stability of positioning in piezoelectric actuators and could potentially lead to operational malfunctions when applied in real-world scenarios like cell manipulation and microelectrode implantation [110].

Stick-slip actuators typically rely on piezoelectric materials. These micro-positioners or micro-actuators equipped with stick-slip actuators can operate in two distinct modes: the stepping mode and the scanning mode (see *Figure 3.2*) [104].

The stepping mode involves applying a sawtooth voltage to the micropositioner, causing it to move step by step across a large range (in mm) at high velocity within the workspace. On the other hand, the scanning mode allows for smooth and precise elongation but is limited to a shorter range (a few μm). To achieve coarse positioning over a wide range combined with fine positioning over a short range, a stick-slip principle can be utilized based on inertia and friction. In this principle, a moving part is connected to a fixed piezoelectric actuator via a friction contact. During slow deformation of the actuator, the moving part follows it (the stick phase), while during abrupt contraction of the actuator, the moving part slips and remains stationary (the slip phase). This alternating sequence of stick and slip phases, resembling scanning and stepping regimes, enables coarse positioning over a wide range, while the stick phase itself enables fine positioning over a shorter range. The sudden movements

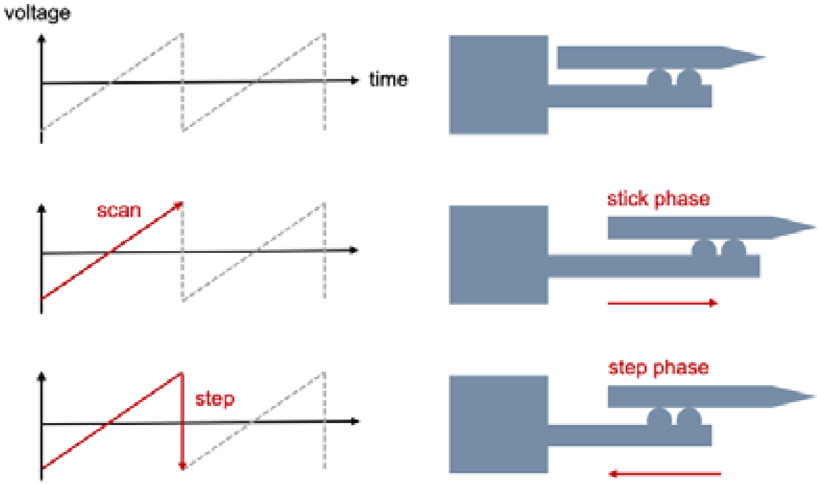

Figure 3.2. Schematic representation of stick-slip actuator working principle. Adapted from [111].

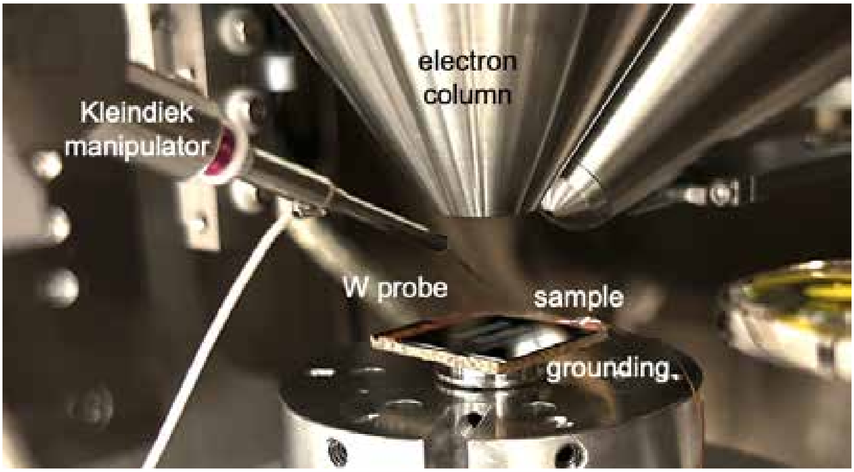

Figure 3.3. The Kleindiek MM3A-EM micromanipulator in SEM Tescan Lyra chamber.

during the step motion induce rapid, decaying oscillations in the manipulator-probe system, with amplitudes comparable to the displacement range of the scan mode [111].

In recent years, several companies like Physik Instrumente, NanoControl, and Nanomotion have introduced novel piezoelectric-based actuators tailored for precise positioning at the micrometer and nanometer scale. Additionally, more products employing inertial drives or walking mechanisms, such as SmartAct and Piezomotor, have entered the market. The Kleindiek MM3A-EM, shown in *Figure 3.3*, stands out as one of the commercial manipulators utilizing piezoelectric stick-slip actuators.

However, a significant challenge in micromanipulation lies in controlling these piezoelectric stick-slip actuators due to their discrete step nature. Consequently, achieving continuous motion for the end-effector mounted on the manipulator is not feasible by sending a continuous signal. Instead, the input must specify the number of steps for each joint movement. Complicating matters further, these actuators' step sizes are not fixed – they vary based on factors such as external loads on the nanomanipulator, the mass of its links, environmental conditions, and other variables. Moreover, these devices commonly lack sensor feedback, making it challenging to control the system's behaviour in a closed-loop manner [112].

3.1.2.2. Quartz Tuning Fork

Advancements in AFM sensing technology led to the adoption of a QTF as an AFM probe in 1989, primarily due to its inherent self-sensing capabilities and high-quality factor (Q-factor) value [113]. Acoustic resonators known as tuning forks feature two prongs (or tines) and are commonly found as quartz components in various electronic applications. A commercial QTF is typically enclosed in a vacuum-sealed canister and stimulated into an anti-phase oscillation mode by two electrodes. While QTFs can also be mechanically excited, this method presents drawbacks in terms of dissipation and control over oscillation amplitude [114].

In contrast to a cantilever probe in AFM, which has only one arm, a QTF possesses two highly symmetrical arms. Typically, a quartz-based probe consists of a QTF and

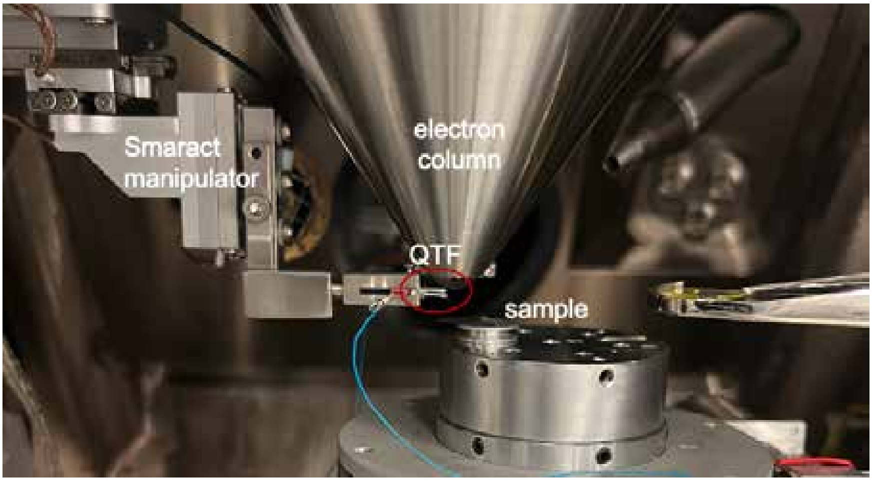

Figure 3.4. QTF integrated in Smaract manipulator system in SEM Tescan Lyra.

tip(s) adhered to one or both QTF arms. When only one tip is affixed to one arm of the QTF, the probe's symmetry is compromised, resulting in a reduction of the Q-factor [115]. The QTF can be integrated into the Smaract manipulator system and other systems in the SEM, as illustrated in *Figure 3.4*.

Quartz tuning forks are available with resonance frequencies up to 200 kHz in their fundamental mode. The limitation of their resonance frequency is determined by optimizing their geometric parameters and the dimensions achievable through industrial fabrication techniques [114]. The Q-factor, often known as quality factor, quantifies the efficiency of an oscillating system. It shows the proportion of energy dissipated per cycle to energy stored in the system. A system with a higher Q-factor will have a sharper resonance peak and better frequency stability because it can store energy for longer periods of time and loses less energy every cycle. A greater Q-factor indicates improved sensitivity and resolution in surface interaction detection [116].

3.1.2.3. Akiyama probe

The Akiyama probe stands out from most cantilevers as it operates as both a self-sensing and self-actuating probe, eliminating the need for a laser to sense tip-surface interaction. This probe integrates a microfabricated Si cantilever with a standard QTF. Vibrations of the tuning fork induce corresponding vibrations in the Si cantilever. Upon contact with the surface, the tip-surface interaction alters the resonance frequency of this combined system. This frequency shift is detected by a phase-locked-loop system using the same electrical contacts that drive the tuning fork vibration. By maintaining a constant shift through a feedback loop, the cantilever tip accurately follows the surface [117, 118]. A SEM micrograph displaying the Akiyama probe integrated into the Smaract manipulator setup is depicted in *Figure 3.5*.

The Akiyama probe has dimensions of approximately 3 mm in length and one-fifth of that in width, with no detection system mounted above it. This slim design enables various applications that are challenging to perform with standard cantilevers and detection systems, such as integration with optical or electron microscopy or

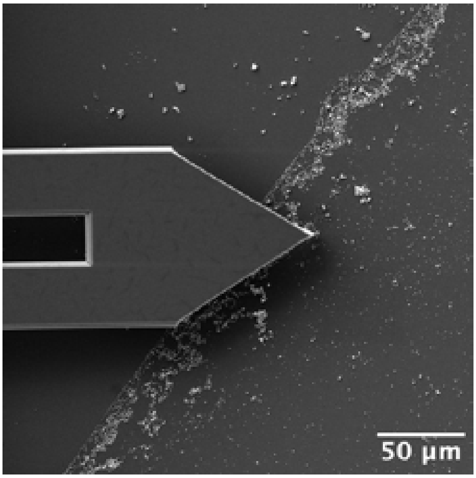

Figure 3.5. SEM micrograph of Akiyama probe integrated into the Smaract manipulator setup above the sample of interest.

measurements within confined spaces. Its lack of optical detection makes it suitable for measuring light-sensitive samples. Comparative studies on numerous commercial and custom-built setups have demonstrated that the Akiyama probe can provide results comparable to those obtained with standard probes in terms of precision and resolution. With a Si cantilever boasting a spring constant of around 5 N/m, it is nearly ten times softer than typical dynamic mode cantilevers, potentially reducing tip damage and extending tip lifespan [119].

3.2. Transmission electron microscopy

TEM is a method of microscopy where an image is created by passing an electron beam across a sample. Most frequently, the specimen is a suspension on a grid or an ultrathin slice that is less than 100 nm thick. As the beam passes through the specimen, the interaction of the electrons with the sample creates an image. The instrument may also generate electron-diffraction patterns, which are helpful for examining the characteristics of crystalline materials [120, 121].

An electron-optical system including an electron gun (which generates the electron beam) and multiple magnetic lenses stacked vertically to form a lens column allows for this total versatility. Three components of the instrument can be easily separated for convenience. The electron gun and two or more condenser lenses, which concentrate the electrons onto the specimen, provide the illumination system. The final TEM image's intensity level and the diameter of the electron beam – also referred to as the illumination – at the specimen are determined by the device's design and operation. The specimen stage allows the insertion or removal of specimens from the TEM as well as the holding of specimens fixed or purposefully moved. A key element in defining the TEM image's spatial resolution is its mechanical stability. The imaging system contains at least three lenses that together produce a magnified image or a diffraction pattern of the specimen on a fluorescent screen, for immediate viewing or for recording by an electronic camera system. How then imaging lenses are operated determines the magnification of the TEM image, while their design specifications largely determine the spatial resolution that can be obtained from the microscope [120]. The comparison between SEM and TEM is shown in *Figure 3.6*.

A set of atoms' planes can scatter an electron beam quite powerfully. These planes result in a diffracted beam when they are properly positioned in relation to the beam. A second set of planes within the same specimen can then re-diffract this diffracted beam, and so on. The strong Coulomb force interaction between the electron beam and the crystal's atoms is the physical cause of this dynamical, or repeating, diffraction. A diffraction pattern can be generated by changing the magnetic lenses so that the back focal plane of the lens – rather than the imaging plane – is positioned on the imaging device. When applied to crystalline samples, this results in a picture that shows a sequence of rings for polycrystalline or amorphous solid materials, or a pattern of dots for single crystals. The orientation of the specimen and the sample's structure that the electron beam illuminates determine the diffraction pattern in the single-crystal scenario. The information in this image gives the investigator insight into the orientation of the crystal with respect to the beam route as well as the space group symmetries within the crystal [121].

Utilizing an electron beam on a vacuum-sealed sample offers an ideal method for achieving high-resolution observations. Indeed, the electron beam serves as a versatile tool for *in situ* studies. Nevertheless, to investigate the overall properties of materials for practical applications with high resolution, researchers aim to incorporate heating,

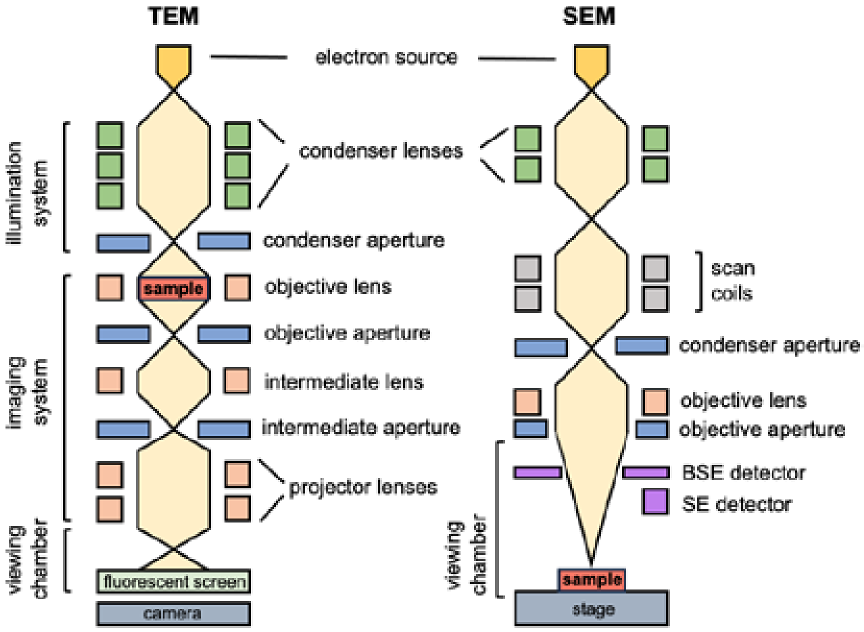

Figure 3.6. Comparison between electron microscopes. Adapted from [122].

cooling, electrical, optical, mechanical, and environmental variables into TEM experiments [123, 124]. *In situ* TEM experiments offer a viable option for temperature-dependent research. Typically, specialized TEM holders are utilized for such experiments. These holders include a heating holder, which features an electrical wire or a MEMS chip, and a cooling holder equipped with a copper rod situated between the specimen and a liquid nitrogen tank. Additionally, the cooling holder includes a heating unit for temperature control [125].

Heating holders in conventional TEM setups can reach temperatures up to 1300 °C, as measured by a thermocouple attached to the holder. In heating experiments, preventing eutectic alloy formation between the specimen and holder material is essential to avoid lower melting points, which could result in material deposition onto the lens or screen if the microscope is properly aligned. The cooling holder for TEM is designed to operate at either liquid nitrogen or liquid helium temperatures. They are particularly valuable for *in situ* investigations of superconducting materials and are well-suited for studies involving polymers or biological tissue [121].

3.3. Atomic force microscopy

The AFM is part of the wider family of devices known as the scanning probe microscopes (SPMs). All SPM techniques share the use of a sharp probe that is scanned across a surface of interest. Depending on the technique and probe tip sharpness, this interaction can produce an extremely high-resolution image of the sample, possibly down to the sub-nanometre scale. A high-resolution three-dimensional topographic image of the surface is produced by the AFM's probe, a stylus that interacts directly with the surface to explore the repulsive and attractive forces that exist between the probe and the sample surface [126]. *Figure 3.7* illustrates the relationship between the force exerted between the tip and the sample and the distance separating them.

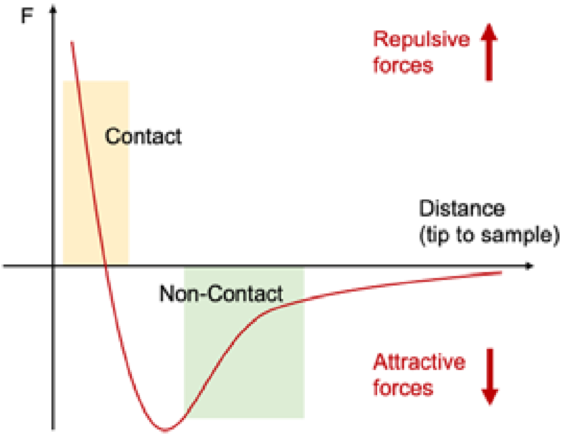

Figure 3.7. Dependence of the force between tip and the sample on distance between them. Adapted from [127].

The AFM is a conceptually straightforward instrument. A sharp-tipped, micrometre-scale cantilever (diameter: 10–50 nm) is scanned across a sample at a few nm distance. The cantilever senses the interatomic forces between the tip and the sample, and a laser and photodetector are typically used to measure the deflection of the cantilever. The tip-sample separation causes a nonlinear variation in the force applied to the tip. When operating in contact mode, the tip is in the repulsive zone of the curve, and a feedback circuit that keeps an eye on the photodetector signal maintains a consistent force throughout the scan. When in contact mode, a tip applies a significant lateral force in addition to a reasonably big normal force to the sample. As a result, tips often wear out quickly and fragile samples get damaged. Furthermore, low-pass noise is present in the process and the deflection signal. The tip oscillates above the sample in the attractive force regime when operating in non-contact mode. Whereas during each oscillation cycle in the tapping contact mode, the tip makes brief (or "taps") contact with the sample [128]. The basic set-up of a typical AFM is shown in *Figure 3.8*.

Cantilevers are typically formed like a V, or like a rectangular "diving board". A sharp tip at the free end of the cantilever serves as an interaction probe. Most frequently, this probe takes the shape of a cylindrical cone or a pyramid with a square base. The most common materials used in commercially produced probes and cantilevers are Si and Si nitride (Si_3N_4, although the exact stoichiometry might vary depending on the production process). Usually, a thin reflective surface made of either aluminium or gold is applied to the cantilever's upper surface, which is opposite to the tip [128]. Different diameters and geometries can be found in the probes used in AFM studies. The AFM probe should be as sharp as feasible if obtaining surface topography with the highest resolution is the intention. However, using probes with a spherical particle attached to the tip or directly to the cantilever is frequently preferred for adhesion measurements [130].

A wide variety of modifications on this fundamental method, depending on the sample's characteristics and the information to be collected, are employed to

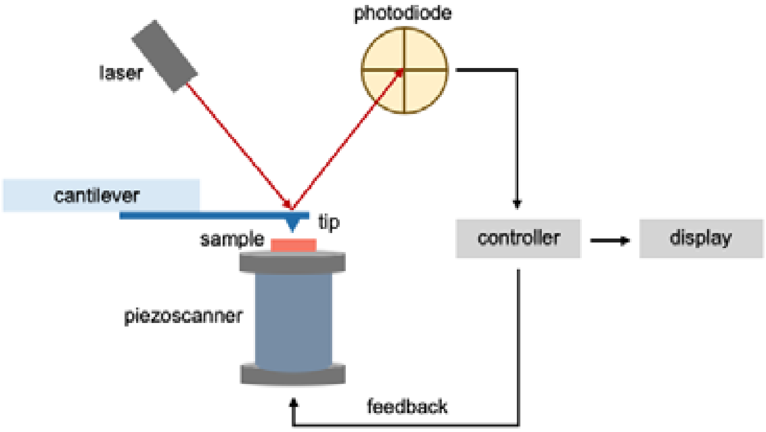

Figure 3.8. AFM operation principle. Adapted from [129].

image surfaces using the AFM. These variations include static methods, such as contact mode, in which the probe makes continuous contact with the sample, and dynamic modes, like intermittent or non-contact modes, in which the cantilever oscillates [126]. Dynamic methods, or dynamic AFM, have been beneficial since the invention of the AFM. They have made it possible to apply mild stresses to samples with great resolution and have established ways to measure conservative and dissipative forces at the nanoscale [131].

Amplitude modulation AFM (AM-AFM), commonly referred to as tapping mode AFM, is widely considered the primary method for characterizing surfaces at the nanometre scale in both air and liquids. In AM-AFM, the cantilever-tip ensemble is stimulated at a fixed frequency, typically close to or at its free resonance frequency, while the oscillation amplitude serves as a feedback parameter to regulate the microscope's operation. The nonlinear nature of the interaction forces between the tip and surface often results in the coexistence of two oscillation states under the same external conditions. This intrinsic nonlinear dynamic behaviour of the AFM is formally depicted through the coexistence of two oscillation branches: one characterized by low amplitude and the other by high amplitude. However, it is more common and intuitive to describe this phenomenon in terms of two dominant interaction regimes: attractive and repulsive. In the attractive interaction regime, a net attractive force predominates the amplitude reduction ($F_{ts} \leq 0$), whereas in the repulsive regime, the amplitude reduction is driven by a net repulsive force ($F_{ts} \geq 0$). Dissipation originates from two distinct sources. First, from the hydrodynamic damping caused by the cantilever's motion interacting with the surrounding molecules of the medium, and second, from the loss of mechanical energy within the cantilever due to interactions with the surface via the tip. It is this latter energy dissipation that is of primary relevance in this context [132].

It has also become increasingly common to use AFM to probe adhesion of various materials at the micro and nano-levels. The foundation of adhesion measurements in nanoindentation tests is the acquisition of force-distance curves, which provide information on the sample's adhesion, hardness, and elastic moduli by measuring the forces between the sample and the probe as a function of their mutual separation in a manner akin to that of macroscopic adhesion tests. Sometimes this technique is called atomic force spectroscopy (AFS). There is zero force applied as the probe approaches the sample. The primary distinction from macroscopic adhesion tests is that, at a specific distance determined by the cantilever's stiffness, the attractive Van der Waals interaction causes the probe to spring into contact. The force then increases as the probe penetrates the material, revealing details about its mechanical characteristics. The probe won't separate from the surface during the retracting cycle unless the force applied to remove the tip from the surface is greater than the adhesion force holding it together. This pull-off force can be used to measure the adhesion [130].

4. MATERIALS AND METHODS

4.1. CuO nanowire synthesis and characterisation

CuO NWs were grown by annealing a copper foil at 400 °C for 2 h at ambient atmosphere. Thermal action was carried out in a tube furnace [111]. The initial morphological analysis of the as-grown CuO NWs on the original substrate was performed by SEM Helios NanoLab 600. All NWs were straight and without kinks. Their length reached up to 5–10 µm, with diameters in the range of 50–200 nm. The image in *Figure 4.1* exhibits as-synthesized CuO NWs on the native substrate.

SiO_2/Si(100) wafers (Semiconductor Wafer, Inc.) with 50 nm thermal oxide were used as substrates for conducting further experiments with individual NWs. Using standard Si micromachining methods, micropatterned Si substrates featuring regular rows of pyramidal holes were fabricated. Initially, SU-8 negative photoresist was spin-coated onto an oxidized Si wafer, followed by exposure using a Heidelberg µPG 101 direct-write micropattern generator. Subsequently, the photoresist was developed, and a hard-baking procedure was performed. The unprotected Si oxide layer was then etched using ammonium fluoride buffered HF, after which the exposed Si was etched in a 25% tetramethylammonium hydroxide solution (TMAH) at 95 °C. Finally, residual photoresist was removed using hot resist remover. The resulting micropatterned substrates underwent immersion in concentrated HF to etch away any remaining Si oxide and were rinsed in deionized water. Consequently, the substrate featured numerous cavities in the shape of inverted pyramids of various sizes, ideal for conducting mechanical tests on suspended NWs [45].

Partially suspended CuO NWs were mechanically manipulated on sample substrate by pushing the suspended end of the NW with a sharp tungsten probe attached to

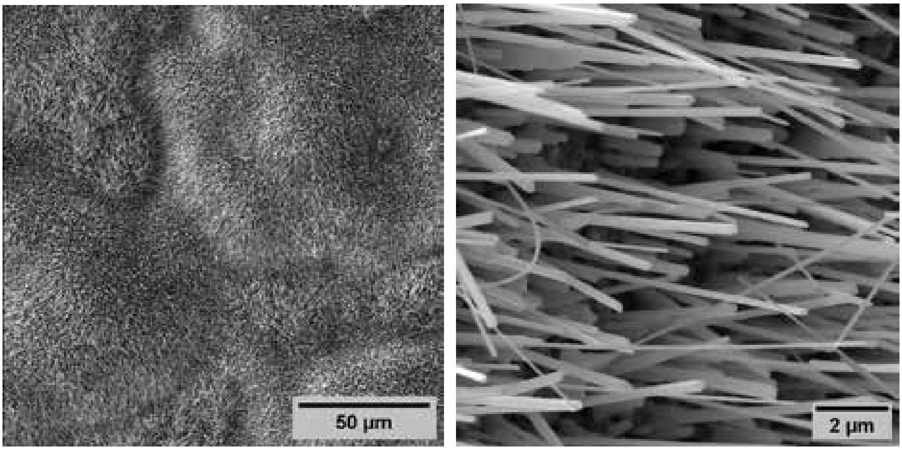

Figure 4.1. As-synthesized CuO NWs on native substrate.

a micromanipulator Kleindiek MM3A-EM. Experiments were conducted inside SEM Tescan Lyra XM. The adhesion between the CuO NWs and Si was high enough to hold the adhered part of the NW during manipulation without the need of additional fastening.

4.2. Ga_2O_3 nanowire synthesis and characterisation

Ga_2O_3 NWs were synthesized using atmospheric pressure chemical vapor transport within a horizontal quartz tube reactor with an inner diameter of 18 mm. The process involved loading a ceramic boat with 0.15 g of Ga_2O_3 powder (Alfa Aesar) at the center of the quartz tube. Oxidized Si wafers SiO_2/Si (100), coated with Au NPs with a diameter of 100 nm in a water suspension (Alfa Aesar), were positioned in a lower-temperature region approximately 10 cm away from the center of the furnace. These Au NPs acted as catalysts for the VLS growth mechanism. The reactor was then heated to 1010 °C (in the high-temperature zone) under a carrier gas mixture of Ar/H_2 5%, maintaining this temperature and gas flow for 30 minutes to facilitate NW growth. Subsequently, the reactor was allowed to naturally cool to room temperature. Ga_2O_3 NWs, reaching lengths of up to 100 μm and diameters in the range of 50–190 nm, were observed to grow on SiO_2/Si substrates downstream in the low-temperature zone, which was maintained at around 850–900 °C.

TEM (Tecnai GF20, FEI) at an accelerating voltage of 200 kV provided information on the crystalline structure of the NWs. Fast Fourier transformation (FFT) was performed on the obtained TEM images to determine crystalline orientations. The structure was also analyzed using X-ray diffraction (XRD) on Rigaku MiniFlex 600 X-ray powder diffractometer. The measurements were conducted in Bragg-Brentano θ-2θ geometry, using a 600W Cu anode (Cu Kα radiation, $\lambda = 1.5406$ Å) X-ray tube. The morphology of as-grown NWs was examined using SEM Helios 5 UX DualBeam. The measurements were performed at an acceleration voltage of 5 keV and a beam current of 25 pA.

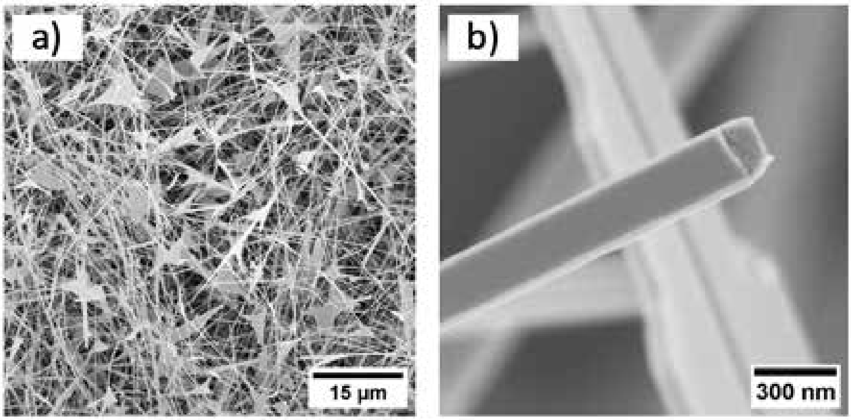

Figure 4.2. SEM micrographs of: (a) the as-grown Ga_2O_3 NWs on Si substrate; (b) an individual Ga_2O_3 NW.

Figure 4.2 presents SEM micrographs of the as-grown Ga_2O_3 NWs on a Si substrate, with depicting the as-grown NWs on the Si substrate as well as an individual NW.

Patterned Si substrates with grooves and inverted pyramids were created from (100) Si wafers (Semiconductor Wafer, Inc.) with a 50 nm thermal oxide similarly to the substrates used for CuO manipulation experiments. Two types of substrates were produced: one with rectangular grooves approximately 10 μm deep for resonance measurements, and another with inverted pyramid holes ranging from hundreds of nm to a few μm deep for three-point bending experiments.

The synthesized NWs were mechanically placed onto the etched Si wafers. Specifically, NWs, especially those partially suspended over the groove with one end free, were chosen for mechanical examinations in SEM. NWs suspended over the inverted pyramid with both ends secured were chosen for three-point bending assessments in AFM.

Resonance measurements were conducted employing a Kleindiek MM3A-EM micromanipulator equipped with a finely pointed tungsten probe. Resonance within the NWs for *in situ* SEM resonance measurements was induced by administering a sinusoidal AC signal between the NW and the tungsten probe, serving as the electrode. Schematics of Si substrates used for mechanical resonance and three-point bending tests are shown in *Figure 4.3*.

The excitation signal comprised a 4V AC component along with a 2V DC component, both generated by a waveform generator (RIGOL DG4162). The DC was used to induce a static deflection or tension in the NW, while the AC was used to drive the NW into mechanical resonance. The AC voltage was chosen to be 4V to be sufficient enough to drive the NW into detectable oscillations without causing damage. The DC was chosen to be 2V because it was enough to create a significant electric field for controlling the NW. Each NW was observed under SEM Tescan Lyra to visually confirm resonance at its fundamental frequency. If the applied frequency aligned with the natural vibration frequency, mechanical resonance occurred, driven by an electric-induced charge on the NW's tip oscillating at the voltage frequency.

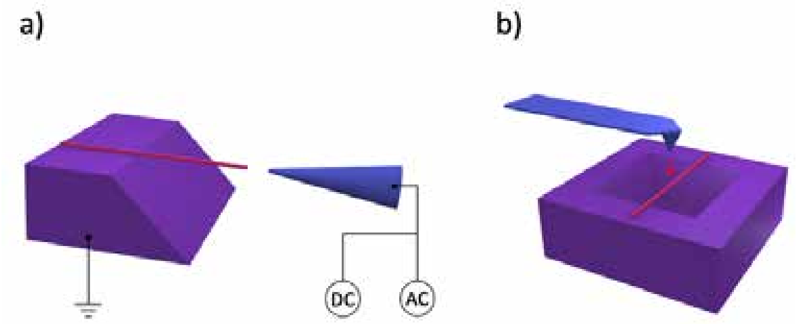

Figure 4.3. Schematics of Si substrates used for mechanical resonance and three-point bending tests: (a) NW suspended above the etched trench with one end immobilized and a tungsten needle applying potential for resonance measurements in SEM; (b) NW suspended over the inverted pyramid with both ends secured for three-point bending measurements in AFM. The red arrow signifies the direction of the applied force.

In SEM, selecting straight and horizontally oriented NWs involved a focus test – if a NW remained in focus across its entire length, it was considered to be in a single plane. This assumption implies that the NW maintains a consistent horizontal alignment without deviating from a straight path. Additionally, to confirm the secure attachment of NWs to the substrate, seven NWs were "welded" to the substrate in SEM using Pt deposition via a gas injection system to test the NW adhesion to the substrate. Resonance frequencies were compared before and after the "welding" process, with no significant difference in resonance frequency values observed, indicating strong fixation of NWs on the Si substrate without requiring additional anchoring. Therefore, continued experiments were conducted with unwelded NWs, as their adhesion to the substrate was sufficient.

When conducting resonance measurements on NWs using *in situ* SEM, the elastic modulus can be determined from the observed resonance frequencies as follows [133]:

$$E_{res} = \frac{48\pi^2\rho}{\beta_n^4}\frac{L^4}{W^2}f_n^2, \tag{4.1}$$

where E_{res} is the elastic modulus, β_i is a constant for the i-th harmonic (for the first harmonic (i = 1), $\beta_1 \approx 1.875$), W is the width of the NW, ρ is the density of the bulk material, v is the NW resonance frequency, and L is the length of the NW.

The Young's modulus of a NW was calculated using the three-point beam bending theory for a beam with two fixed endpoints in the following way [134]:

$$E_{tpb} = \frac{F \cdot L^3}{192 \cdot \delta \cdot I}, \tag{4.2}$$

where F is the applied force, L is the suspended length, δ is the displacement of the NW and I is the second area moment of inertia [135]. The second area moment of inertia for a rectangular beam is given by:

$$I = \frac{w \cdot h^3}{12}, \tag{4.3}$$

where w is the width of the NW and h is the height of the NW. Width of individual NWs was measured from SEM images, using the Fiji ImageJ2 software.

4.3. Au nanowire synthesis and characterisation

Au nanostructures were synthesized using a three-step process. All chemicals were procured from Sigma-Aldrich. Initially, a seed solution was prepared in a 25 mL glass bottle by combining 19.8 mL of 0.025 M sodium citrate solution in deionized (DI) water with 0.2 mL of 0.00025 M $HAuCl_4$ solution. Simultaneously, an ice-cold 0.01 M $NaBH_4$ solution was prepared separately. Subsequently, 0.6 mL of the $NaBH_4$ solution was added to the sodium citrate solution while vigorously stirring, resulting in an immediate orange-red colour change. The growth solution was then prepared by mixing 240 mL of DI water with 0.2 M hexadecyltrimethylammonium bromide (CTAB) and 10 mL of 0.0001 M $HAuCl_4$, followed by the addition of 1.5 mL of 0.1 M ascorbic acid. The growth solution was divided into two 25 mL glass bottles labelled "A" and "B", while 200 mL was placed in vessel "C" (a flat-bottom conical flask).

To vessel “C”, 0.25 mL of concentrated HNO_3 was added. Next, 0.2 mL of the citrate-stabilized Au seed NPs solution was added to bottle “A” and stirred for 1 min. Subsequently, 0.2 mL of the solution from bottle “A” was transferred to bottle “B” and stirred for 1 min. Finally, 0.2 mL of the solution from bottle “B” was transferred to vessel “C” and stirred. The “C” solution was maintained at a temperature of 25 °C for 12 h (note that crystallization of CTAB may occur if the solution temperature drops below 25 °C). The precipitates of Au NPs were observed at the bottom of the vessel after the reaction. The supernatant was decanted from the solution, and the precipitated Au NWs were redispersed in 5 mL of DI water. The synthesized NWs were a few μm long with a diameter of approximately 50 nm [86]. The *Figure 4.4* illustrates synthesized Au NWs on a Si substrate.

SEM studies were performed using the Helios 5 UX DualBeam with an acceleration voltage of 5 keV and a beam current of 25 pA. The examination of Au NWs involved measuring approximately 90 individual NPs using Fiji ImageJ2 software. Measurements were executed utilizing the Analyze-Measure function, with NW dimensions selected based on SEM micrograph background contrast, facilitating precise identification of start and end points for each NW.

The removal of surfactants from the Au NW solution followed a 5-cycle procedure shown in *Figure 4.5*. Each cycle entailed 20 minutes of sonication followed by 20 minutes of centrifugation at 5000 rpm, using distilled water as the solvent for sonication. Following centrifugation, excess solution was replaced with distilled water, with this process being repeated 5 times to ensure thorough surfactant removal. The method involved depositing 5 droplets of 2.5 μL each of the Au NW solution onto a Si substrate heated at 90 °C, resulting in a film of Au NWs.

In this work, the manipulation of NPs was conducted using an AFM Dimension Edge Bruker equipped with a rectangular AFM cantilever (NCHR, Bruker) characterized by a force constant of k = 42 and a resonance frequency of 320 kHz. All imaging and manipulation scans were conducted in tapping mode. Initially, an overview image covering a 20 × 20 μm area was captured. Subsequently, a series of manipulation scans were conducted over a 10 × 10 μm scan range, progressively increasing the force

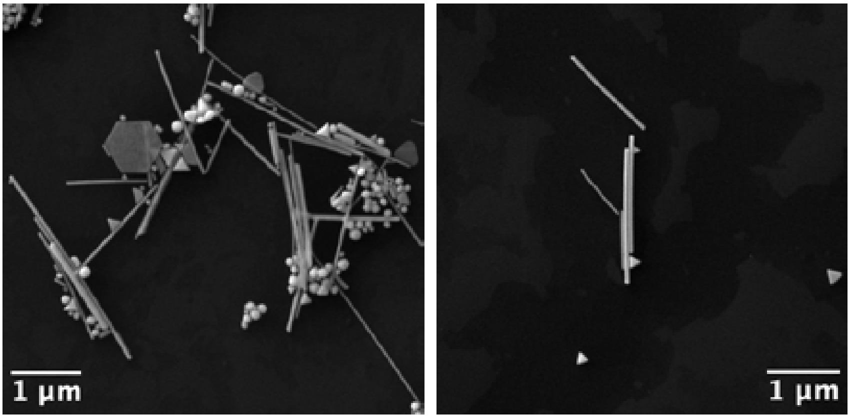

Figure 4.4. Au NWs and nanostructures on Si substrate.

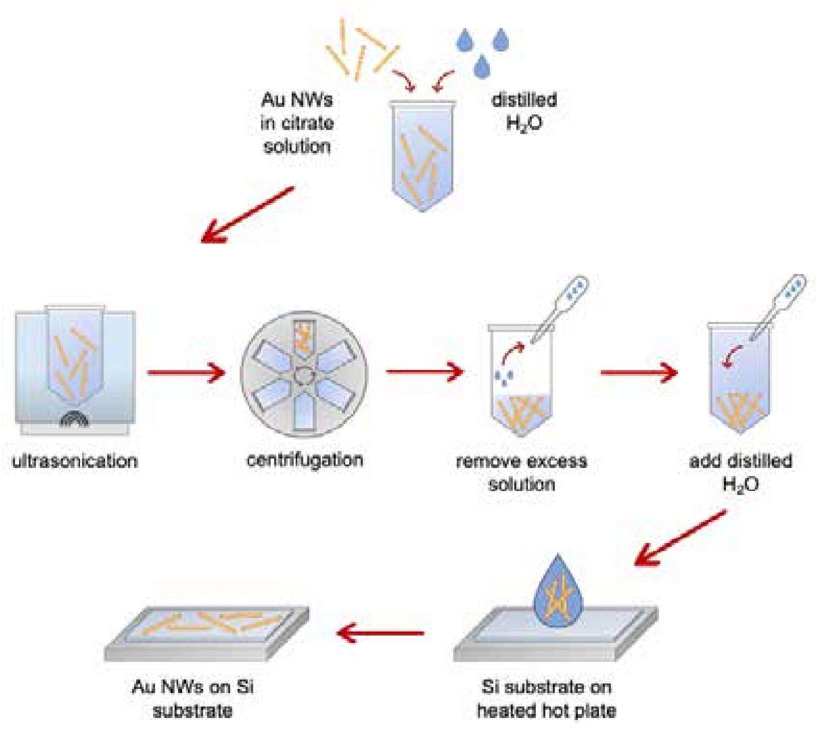

Figure 4.5. Surfactant removal from Au NWs and sample preparation process by droplet evaporation method.

applied by the tip to the surface in each scan. Following the manipulations, another overview image spanning 20 × 20 µm was acquired. The comparison of the pre- and post-manipulation images facilitated the enumeration of movable and immovable NPs. Manipulation was carried out in a total of five different areas. The formula developed by Anczykowski et al. [136] was used to calculate the dissipated power:

$$P = k \cdot f_0 \cdot (A_{set} \cdot A_{piezo} \cdot \sin\theta - A_{set}^2/Q), \tag{4.4}$$

where k is the cantilever's force constant, f_0 is the cantilever's resonance frequency, A_{set} is the setpoint amplitude, A_{piezo} is the driving amplitude, θ is the phase signal, and Q is the quality factor of the AFM cantilever. The phase signal was extracted from tapping mode phase images using the Gwyddion software (version 2.63) [86].

Samples were examined with Raman spectroscopy both before and after heating. 5 µL of 6.1×10^{-5} M Rhodamine B was applied by drop-casting. Rhodamine B is frequently used in SERS due to its strong Raman scattering properties. It can be detected and analyzed at very low concentrations, making it an excellent probe for evaluating the sensitivity and effectiveness of SERS substrates. Raman spectroscopy was conducted using the Princeton Instruments TriVista CRS Confocal Raman Microscope (TR777), equipped with three monochromators and a microscope featuring diffraction gratings with line densities of 600, 900, and 1800 lines/mm, and a focal length of

750 mm. The microscope's slit aperture was set at F/9.8. Excitation was achieved using a Laser2000 diode laser with a 785 nm wavelength and a maximum output power of 200 mW. The laser had a diameter of approximately 20 µm, covering around 5–10 NWs in the measurement area. Five spots from each sample were examined, with exposure times and laser power matched across all measurements. Spectral intensities were maintained in relative units, and background extraction was performed in Origin software by spline approximation of the fluorescence spectrum and subsequent subtraction from the total spectrum, yielding the isolated Raman spectrum.

The enhancement factors (EFs) for Rhodamine B molecules were calculated with respect to a pure Rhodamine B powder spectrum at the 1358 cm^{-1} peaks according to the equation [137]:

$$EF = \frac{I_{SERS}/C_{SERS}}{I_{RS}/C_{RS}}, \tag{4.5}$$

where I_{SERS} is the Raman intensity and C_{SERS} is the concentration of Rhodamine B used in SERS measurements; I_{RS} is the Raman intensity and C_{RS} is the concentration of Rhodamine B used in routine Raman measurements.

4.4. Ag nanowire characterisation

Silver NWs measuring approximately 120 nm in diameter and tens of µm in length were procured from Blue Nano, Inc. SEM images were captured using an FEI Nanosem 450. The examination of Ag NWs was conducted on individual NWs with Fiji ImageJ2 software. Measurements were carried out using the Analyze-Measure function, where NW dimensions were determined based on the background contrast in SEM micrographs The *Figure 4.6* illustrates Ag NWs applied on Si substrate.

For heat-treatment investigations, samples were prepared by drop-casting the Ag NWs onto the patterned substrates from a solution similarly to Au NWs. Patterned Si substrates featuring grooves and inverted pyramids were fabricated

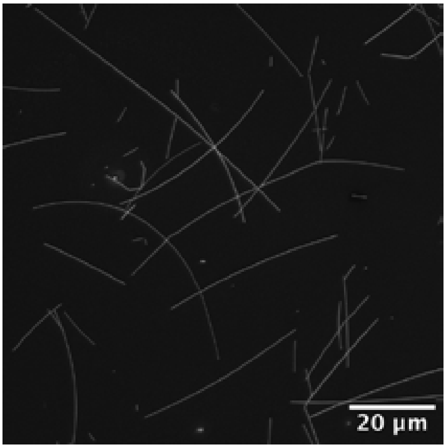

Figure 4.6. Ag NWs applied on Si substrate.

from (100) Si wafers (Semiconductor Wafer, Inc.) with a 50 nm thermal oxide layer, similar to those used in CuO and Ga_2O_3 manipulation experiments. The substrates included inverted pyramid holes, ranging in depth from hundreds of nanometres to a few micrometres. Given that the width and period of the holes were intentionally made significantly smaller than the average length of NWs, numerous NWs spanned multiple holes simultaneously. This setup offers significant advantages, allowing for the examination of substrate effects on the same NW by contrasting the behaviour of suspended versus adhered segments.

A distinct set of experiments was conducted on Ag NWs within a TEM to investigate the impact of heat treatment on the internal structure of the NWs. For the Ag NW heating experiments, Cu TEM grids with a 20 nm Al_2O_3 layer were used to ensure heat resistance of the grid. Two TEMs, Tecnai GF20 by FEI and the JEOL model ARM-200F, were utilized, operating at an accelerating voltage of 200 kV [138].

5. RESULTS AND DISCUSSION

5.1. Post-synthesis kinking in CuO nanowires

The properties and functionalities of NWs can be altered by introducing different defects, such as nano-twins [139, 140] and kinks [141]. Kinked NWs are gaining interest for their potential applications in electronics [141–143] and nanomechanical devices [144, 145], as well as for their reported enhancement in mechanical durability [146].

In this section, three different manipulation scenarios leading to post-synthesis kinking are described in detail. Furthermore, the experiments demonstrate the possibility of reversible plasticity in CuO NWs, as evidenced by the complete unkinking of a single NW in one instance. Molecular dynamics (MD) simulations support the experimental findings and elucidate a mechanism of reversible deformation-induced crystal twinning. The findings presented in this section have been published in **Paper I**.

5.1.1. CuO nanowire transfer onto substrates

CuO NWs employed in this study were synthesized through the annealing of a Cu foil. Subsequently, the as-grown CuO NWs were examined on their initial growth substrate using SEM. The NWs appeared straight and devoid of any kinks, exhibiting lengths ranging from 5 to 10 µm and diameters spanning 50 to 200 nm. The cross-sections of the NWs displayed an irregular shape typical of monoclinic crystal systems (see *Figure 5.1*).

The NWs were mechanically transferred onto three distinct types of Si substrates through manual manipulation. This process involved pressing and then shearing the Cu foil, along with the attached NWs, against the substrates, as illustrated in *Figure 5.2*.

Type I substrates consisted of unetched Si wafers, where the NWs lay flat on the surface. Type II substrates featured square-shaped etch pits with dimensions on the order of a few micrometers in length and the depth in the range of several hundreds of nanometers. Lastly, type III substrates comprised parallel trenches with a width of 3 µm, separated by planes of unetched Si measuring 900 nm wide. The sidewalls of the pits and trenches had a slope relative to the main surface of Si at an angle of 54.7 degrees, corresponding to the angle between the (111) and (001) planes in Si wafer. Consequently, some NWs were partially exposed above the etch pits and trenches on the type II and III Si substrates.

5.1.2. Kinking by mechanical transfer

Upon examining the CuO NWs that underwent mechanical transfer onto the Si sample substrates or the Si TEM grid, as illustrated in *Figure 5.3(a)*, it was noted that a considerable portion exhibited deformations resembling “kinks”. These deformations entailed an abrupt change in orientation while maintaining their structural integrity.

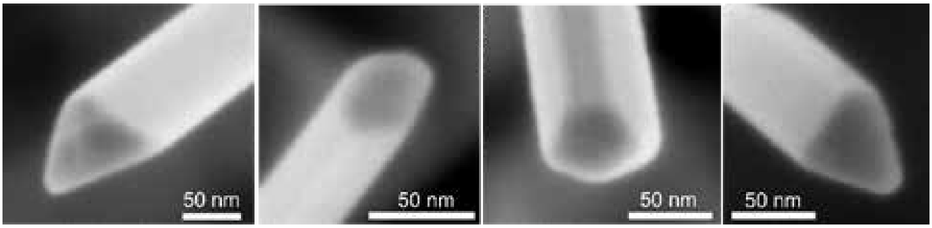

Figure 5.1. SEM images of CuO NWs cross-section profiles.

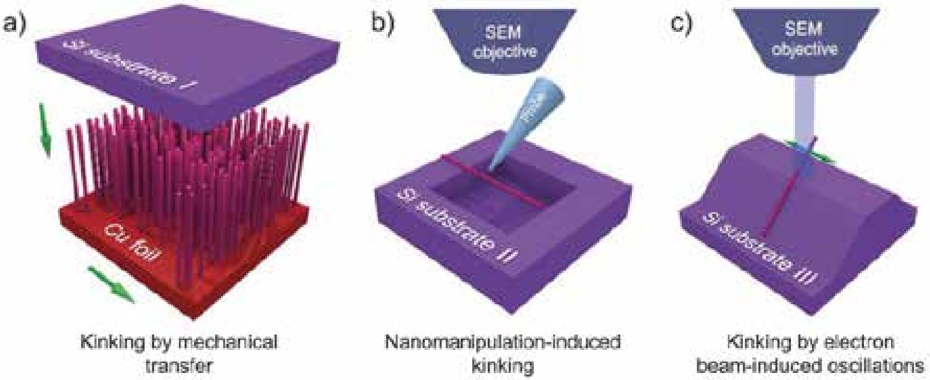

Figure 5.2. Schematic representation of the sample substrates, the positioning of the CuO NWs on them, and the manipulation operations that induced kinking.

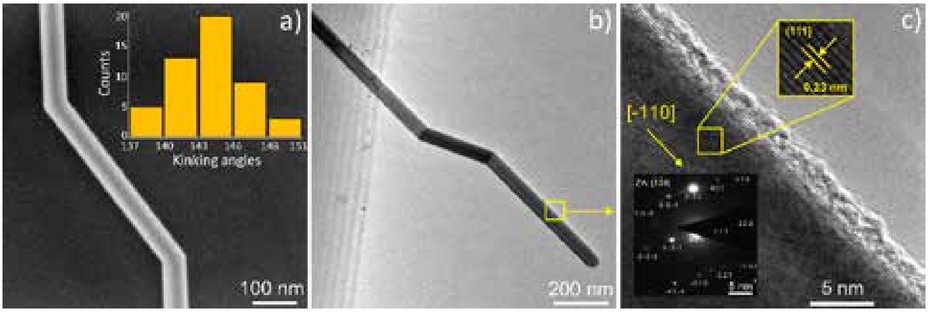

Figure 5.3. (a) SEM micrograph of a CuO NW kinked after mechanical transfer on a flat Si substrate. The inset presents a histogram displaying the distribution of kinking angles measured across 50 kinked NWs from SEM images; (b) TEM image capturing a CuO NW with kinks following mechanical transfer onto a TEM grid made of Si; (c) TEM image of the same NW at higher magnification alongside its corresponding selected area electron diffraction (SAED) pattern. The arrow denotes the growth direction of the NW, which is $[\bar{1}10]$.

Notably, no kinked NWs were observed on the original growth substrate, suggesting that this transformation occurred during the mechanical transfer process. The kinking angles of the CuO NWs appeared to fall within a very narrow range, as depicted in the inset of *Figure 5.3(a)*, with a median value of 143.2 ± 2.9 degrees. This measurement was derived from the analysis of SEM images of fifty kinked NWs on the type I (flat) sample substrate, as shown in *Figure 5.2(a)*. The uniformity of these angles implies a direct correlation between the observed deformation and the structure of the CuO crystal, rather than being a random defect. Furthermore, with few exceptions, which could likely be attributed to post-kinking fracture, the kinked NWs consistently exhibited a double kink that divided the NW into three segments, as depicted in *Figure 5.3*. Additionally, in most cases, NWs with multiple double kinks were observed.

5.1.3. Nanomanipulation-induced kinking and unkinking

A series of nanomanipulation tests were conducted on partially suspended CuO NWs transferred onto a structured Si wafer (Substrate type II) to investigate their response to external mechanical loading. A tungsten probe attached to a nanomanipulator was used to push the NWs (see *Figure 5.2(b)*). The experiments were carried out within SEM, allowing real-time visual feedback. The movement of the nanomanipulator occurred either smoothly within the "scan mode" of the piezo scanner, with a limited range of a few microns, or abruptly within the "step mode", based on the stick-slip motion of the piezoelectric actuator. This abrupt movement induced fast-decaying oscillations in the manipulator-probe system with an amplitude on the order of several micrometers. It was observed that abrupt movement of the probe could cause kinking in CuO NWs protruding over the etch pit of the Si substrate sample. However, the timescale of kinking events was below the temporal resolution of the SEM scanning rate, allowing only pre- and post-event image observation.

Figure 5.4(a–e) depicts the sequence of mechanical nanomanipulations aimed at inducing kinking in a single CuO NW. The CuO NW is partially suspended over the etch pit of the Si sample substrate (the darker area represents the bottom of the pit).

Initially, the nanomanipulator probe is positioned near the NW, and then it pushes the NW against the sidewalls of the pit. At a certain point (see *Figure 5.4(c)*), the manipulator executes an abrupt movement ("step"), resulting in the kinking of the NW. In most cases where kinking was achieved, the kinked region was near the sharp edge or corner of the pit. Twenty-three kinking events were recorded during nanomanipulation experiments, although brittle fracture of NWs was a more common outcome of manipulation in "step mode". No kinking was observed during manipulation in the scan mode of the nanomanipulator, indicating that mechanically induced kinking requires specific conditions to occur. During bending in scan mode, the NWs remained fully elastic until reaching the ultimate strength limit, resulting in brittle fracture. Quantitative measurements of the bending strength of these NWs were conducted in another study, yielding high values of 8.2 ± 2.7 GPa, indicative of pristine single crystals with low concentrations of critical defects [41]. This aligns with the structural analysis.

By pushing the already kinked NWs, it was observed that they exhibit considerable durability and elastic behaviour, maintaining the angle of the kink even in the absence

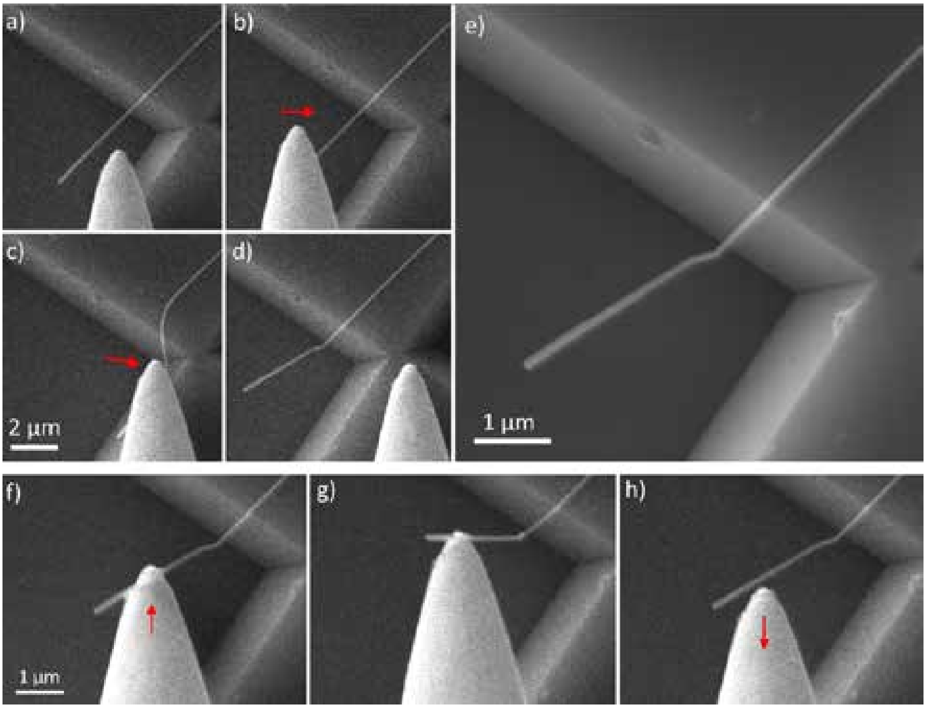

Figure 5.4. Kinking induced by nanomanipulation in a CuO NW.

of external force. Under conditions of severe deformations or due to abrupt movements of the manipulator, the NWs may experience breakage at the kink. However, in the majority of instances, fractures occur at random points outside the kinked region, suggesting that there is no significant weakening of the crystal at the kink. Selected frames from a single nanomanipulation experiment performed on a previously kinked CuO NW are illustrated in *Figure 5.4(f–h)*. These frames depict the same NW as observed in *Figure 5.4(a–e)*. The probe of the nanomanipulator maneuvers beneath the CuO NW (see *Figure 5.4(f)*) and then gradually shifts it sideways and upward (see *Figure 5.4(g)*). Upon retraction of the probe, the NW promptly restores its original shape without experiencing any additional deformation (see *Figure 5.4(h)*), thereby preserving both the kink location and kinking angles.

Another series of nanomanipulation experiments involved “welding” of NWs onto a Si substrate in SEM using Pt deposition via a gas injection system. The goal was to secure the NWs to the substrate and observe any effects on inducing kinks. The welded rectangle in *Figure 5.5(a)* has dimensions 0.64 × 1.38 µm.

In *Figure 5.5(b)*, manipulation with the probe caused a kink in one part of the NW. No significant differences were observed between the behaviour of NWs that were welded to the substrate and those that were not. However, it was noted that the welded NWs showed a greater frequency of breakages. This was attributed to one part of the NW being well adhered to the substrate, leaving no space for movement and slipping away, leading to increased stress concentration and subsequent breakages during manipulation.

In a single instance, a CuO NW was successfully kinked and subsequently straightened back to its initial profile (see *Figure 5.6*). The probe was positioned closely above the NW and then moved using a coarse nanomanipulator motion (see *Figure 5.6(b)*). As the probe was retracted, the NW appeared to be kinked (see *Figure 5.6(c, d))*.

Subsequently, the kinked NW was pushed and displaced by the probe (see *Figure 5.6(e, f)*) to assess if it would break at the kink. Unexpectedly, upon retracting the probe, the NW appeared not only intact but also straightened (see *Figure 5.6(g, h)*).

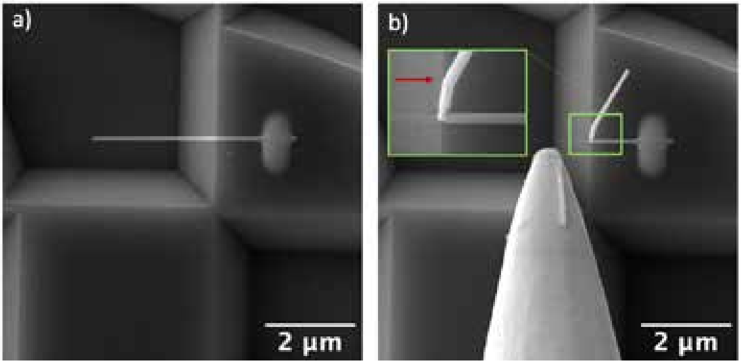

Figure 5.5. An example of kinking induced by nanomanipulation in a CuO NW welded on a Si substrate.

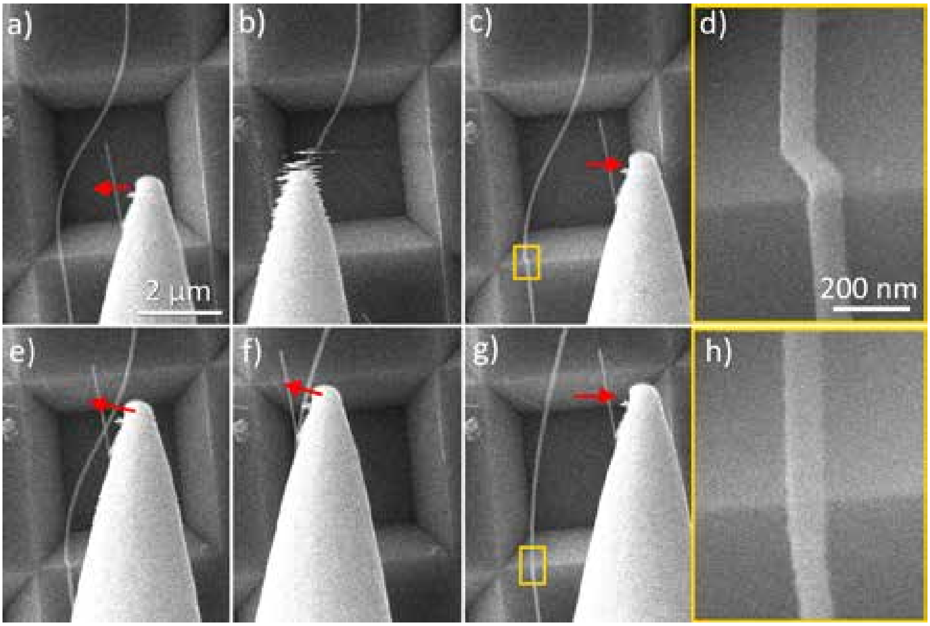

Figure 5.6. The manipulation of a single CuO NW to induce both kinking and subsequent unkinking.

This reversal of the kinking process appears to necessitate even more specific conditions compared to the initial kinking, as similar outcomes were not achieved with other NWs. It appears that a crucial factor is the suspension of a sufficiently long NW over the pit, maintaining its suspended state.

5.1.4. Electron-beam-induced oscillation followed by kinking

It was observed that kinking of CuO NWs can also be achieved through electron-beam induced oscillations of the free-standing portion of a NW. This phenomenon was noted for NWs transferred onto the type-III patterned Si sample substrate (see *Figure 5.2(c)*). It occurred at a slow e-beam scanning speed, inducing auto-oscillations in the protruding part of the NW. An instance of this is illustrated in *Figure 5.7*.

Initially, to sacrifice image quality, the NW is imaged at a high scan rate (few frames per second) to prevent the electron flux from inducing oscillations (see *Figure 5.7(a)*). Subsequently, the NW is imaged at a slower scanning speed, leading to self-oscillations in the NW. These oscillations are noticeable by the smeared appearance of the NW part above the red arrow in *Figure 5.7(b)*, as SEM imaging progresses line by line (horizontally) from the top left corner to the bottom right corner.

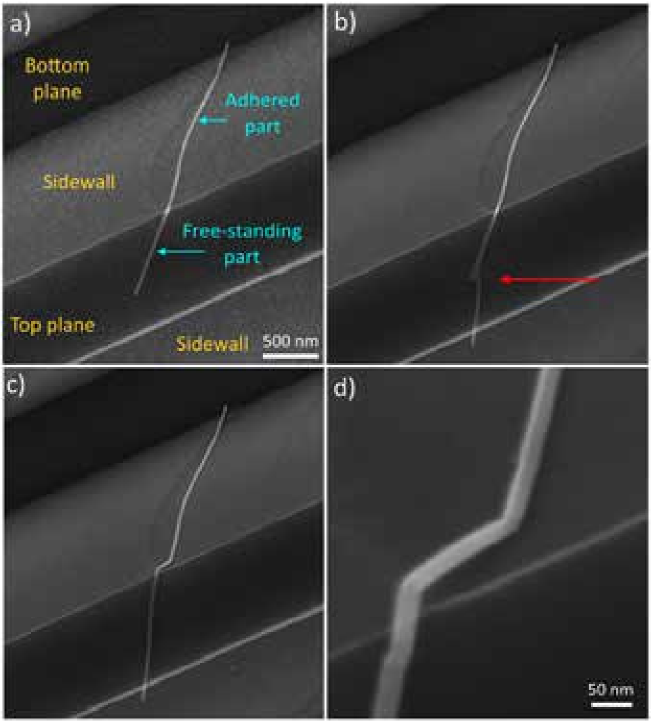

Figure 5.7. Oscillation induced by electron beam, subsequently resulting in kinking of the CuO NW situated on the structured Si substrate. The accelerating voltage of the electron beam is 10 kV.

When the beam reaches the position marked by the red arrow in *Figure 5.7(b)*, the oscillating segment makes contact with the substrate. Consequently, *Figure 5.7(b)* displays partial data from two states of the NW in a single image. The upper portion above the red arrow corresponds to an oscillating NW, while the lower part depicts the NW resting against the top plane of the Si structure. By this juncture, a kinking event has already occurred. The outcome of the oscillation-induced kinking is illustrated at various magnifications in *Figure 5.7(c, d).*

The occurrence of a kinking event triggered by e-beam-induced oscillations was exceedingly rare, with only a few cases observed per thousands of CuO NWs protruding above the substrate. Furthermore, in an even smaller number of instances (three cases out of a few hundred experiments where significant NW oscillations were observed), the e-beam-induced oscillations appeared to cause the melting of CuO NWs. This phenomenon was characterized by the abrupt transformation of the oscillating portion of the NW into a sphere.

5.1.5. Structural characterization of the kinked CuO nanowires

In order to understand the kinking mechanism, a detailed examination of the exact crystallographic structure of the NWs at the kink area was needed. To accomplish this, CuO NWs were mechanically transferred on Si TEM grids and high-resolution TEM imaging was conducted on several CuO NWs that were kinked by the transfer. *Figure 5.8(a)* presents a TEM image depicting a kinked NW precisely at the kinked area. In *Figure 5.8(b)*, a closer examination of the kink is performed to observe its precise crystallographic structure. Additionally, *Figure 5.8(c)* displays the corresponding SAED image of the same kink region.

Figure 5.8(b) strongly indicates that the kink is formed by a twin boundary. The deeper investigation of its exact crystallographic structure starts with the hypothesis that the twinning plane is the $(\bar{1}10)$, i.e., parallel to [110], [112], and [001], and the growth direction is $[\bar{1}10]$, as indicated in *Figure 5.8(b)*. Observations reveal that

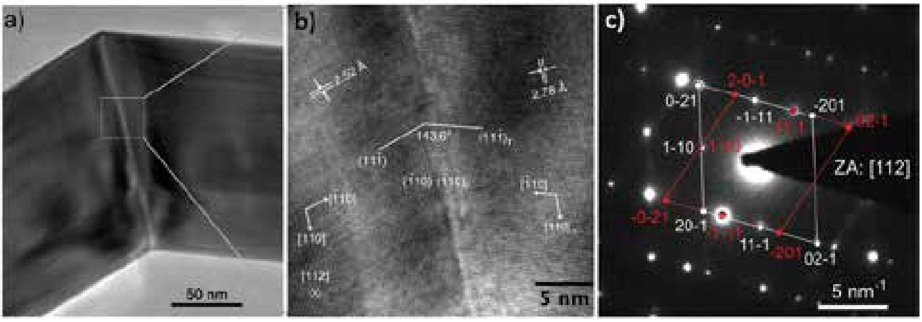

Figure 5.8. (a) TEM micrograph capturing the kinked segment of the CuO NW; (b) High-resolution TEM image of the region specified in (a). (c) SAED image of the identical kink region, demonstrating excellent alignment with the zone axis of the image denoted as [112]. The SAED image integrates reflections from both the left and right portions of the NW (before and after kinking), with corresponding sets of reflections indicated by white and red rhombi.

the SAED image exhibits a good alignment with the zone axis, identified as [112]. To precisely assess the crystallographic structural features depicted in the TEM image, an analysis of its periodicities was conducted through two-dimensional Fourier analysis. The complete kink angle predicted theoretically by the hypothesis, i.e., two times the angle between the direction $[\bar{1}10]$ and the plane $(\bar{1}10)$ is 142.9°, with its projection on the image plane being slightly higher at 143.12°. These values are in excellent agreement with the corresponding value extracted from the Fourier analysis of the TEM image being 143.6°, as well as with the average kinking angle (143.2° ± 2.9°) found upon measuring many kinked NWs using SEM. Hence, the hypothesis on the crystallographic structure of the kink is confirmed by the experimental data.

5.1.6. Molecular dynamics modelling

In collaboration with Institute of Technology, University of Tartu, a simulation to comprehend the dynamics of the kinking and unkinking process, was conducted on an infinite CuO crystal. This simulation involved introducing a nano-twinned band comprising 4 monoatomic Cu layers, with the twin plane designated as the $(\bar{1}10)$, as illustrated in the inset (a) of *Figure 5.9*.

The simulations revealed that when subjected to shear loading (imposed strain) directed towards the projection of the growth direction $[\bar{1}10]$ on the twin plane $(\bar{1}10)$, depicted in the schematics above *Figure 5.8*, the twinned band expands as the twin planes shift layer by layer. *Figure 5.9* illustrates the progression of the total applied shear strain (in green, right axis) and the corresponding stress (in blue, left axis). The plane of deformation (image plane of the schematics) is defined by the $[\bar{1}10]$ vector and the normal vector of $(\bar{1}10)$. When a positive strain is applied as designated in inset (a) of the *Figure 5.9*, the twinned band expands by four Cu layers. Subsequently, the system is

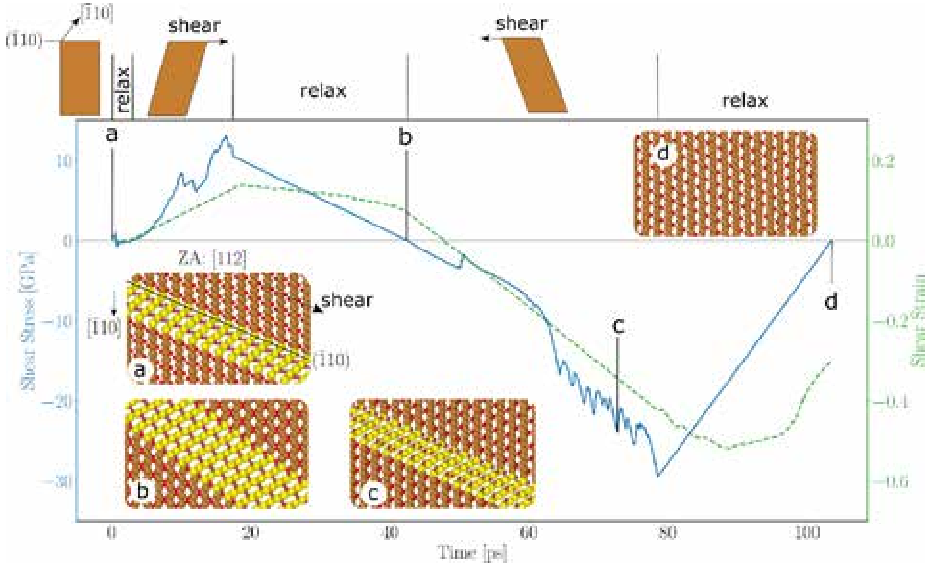

Figure 5.9. Evolution of shear stress and strain in the simulated CuO crystal.

allowed to relax, leaving the atomic system in the deformed state depicted in inset (b) of the *Figure 5.9*, with the twinned band larger than initially. Following this, a shear strain is enforced in the opposite direction, resulting in the negative shear stress depicted in the figure. As straining continues, more stress accumulates, subsequently released through a series of shifts of the twin planes that contract the twin band, accompanied by a few $(\bar{1}10)$ plane slips. These sequences of plastic deformations are noticeable as oscillations on the stress curve, leaving the crystal in the state depicted in inset (c) of the *Figure 5.9*. Subsequently, immediately after (c), a series of atomic rearrangements occurs, completely eliminating the twin band and resulting in an almost pristine crystal. The system is then relaxed to zero pressure, reaching the final state depicted in inset (d) of the *Figure 5.9*, which corresponds to a defect-free CuO crystal. Atomic rearrangements eliminate the twinned band, resulting in a defect-free CuO crystal, demonstrating how shear stresses induce and eliminate twinned band defects.

5.1.7. Hypothesis of the observed phenomena

In this study, kinking occurred post-synthesis in initially straight NWs under distinctly different experimental conditions. This phenomenon was observed during the mechanical transfer of numerous free-standing NWs between substrates, induced by oscillations caused by in-situ electron-beam irradiation, and through in-situ mechanical nanomanipulation of partially suspended NWs. Across all these scenarios, the same plastic deformation, characterized by double kinking with an angle of approximately 143 degrees, was observed.

Reproducing nanomanipulation and e-beam induced kinking consistently proved to be challenging. In the nanomanipulation case, the process is driven by the coarse motion of the nanomanipulator, while in the e-beam induced kinking, momentum and charge transfer from the beam to the NW are the driving forces. However, in neither case is mechanical loading well controllable. Moreover, the adhered NWs exhibit various parameters such as differing lengths of adhered and protruding parts, diameters, and cross-sections, which could significantly influence the outcome of manipulation experiments. Thus, inducing kinking in individually manipulated NWs relies on favourable parameter coincidences. Conversely, in the mechanical transfer scenario, the substantial number of NWs subjected to various loading conditions allows for a significant portion of them to become kinked. Additionally, observing kinking during mechanical transfer helps rule out the e-beam's essential role in the kinking process.

Common factors exist between kinking induced by nanomanipulations and e-beam. In both scenarios, NWs were partially suspended, and oscillations were observed before kinking. Inducing kinking was not possible during a smooth nanomanipulation operation or under e-beam without the specific etched Si substrate allowing the suspension of NWs at a certain angle. Additionally, MD simulations revealed that the shear loading required for inducing growth of the kinked band is highly specific in direction. This correlates with the low reproducibility of nanomanipulation and e-beam induced kinking, suggesting that oscillations may play a crucial role, at least in the in-situ kinking of individual NWs. Following an abrupt motion, the manipulator probe and the NW oscillate in a complex manner, akin to observations under e-beam, leading to mechanical loading in various directions. Among these directions, one may be favourable for inducing the necessary atomic rearrangements that result in kinking. Moreover, kinking predominantly occurred when the protruding part of a NW contacted the Si substrate during nanomanipulations or e-beam induced oscillations. This could be another contributing factor, as NW-substrate adhesion may increase internal shear loading by securing the NW ends. Lastly, both shear loading in mechanical transfer and oscillations related to NW manipulations may entail triboheat-related temperature rise, which could be another contributing factor in the likelihood of kink formation.

Based on the above findings, it can be inferred that all three experimental scenarios share a common underlying plastic deformation mechanism responsible for kinking, which can also be reversible under specific conditions. Structural analysis using TEM and SAED images, along with MD simulation results, support the notion that this mechanism involves deformation-induced twinning. While deformation twinning is commonly observed in metallic materials and alloys, the reversible plasticity observed in covalent nanomaterials is unexpected, as they typically transition from elasticity to fracture. However, the extremely small size of the NWs, allowing for nearly defect-free crystal structures, has been suggested to enable higher stresses and strains without fracture, facilitating reversible plasticity.

5.1.8. Summary

In this study, the manipulation-induced kinking and potential unkinking of CuO NWs was investigated. Through experiments involving mechanical transfer, nanomanipulation, and electron-beam-induced oscillation, the occurrence of kinking along twin boundaries in covalent NWs is demonstrated. Remarkably, with one instance showing successful unkinking, NWs can also exhibit reversible plasticity. The importance of manipulations is in revealing a plastic deformation mechanism, involving deformation-induced twinning. Structural characterization and MD simulations confirm the role of shear loading in inducing twinning. This study marks the first observation of reversible plastic deformation in covalent NWs, offering new research directions to modify NW properties post-synthesis and enabling advancements in various applications and enabling new functionalities.

5.2. Mechanical properties of Ga_2O_3 nanowires

In this section, the elastic modulus of individual β-Ga_2O_3 NWs is investigated through two different techniques: *in situ* SEM resonance and three-point bending in AFM. Additionally, the structural and morphological characteristics of the synthesized NWs are examined using XRD, TEM and SEM. The findings presented in this section are published in **Paper II**.

5.2.1. Ga_2O_3 nanowires

For structural analysis of the as-grown NW arrays on Si (100)/SiO_2 substrates, XRD measurements were performed. The identified peaks correspond to monoclinic β-Ga_2O_3 (ICDD-PDF #41–1103), as shown in *Figure 5.10(a)*.

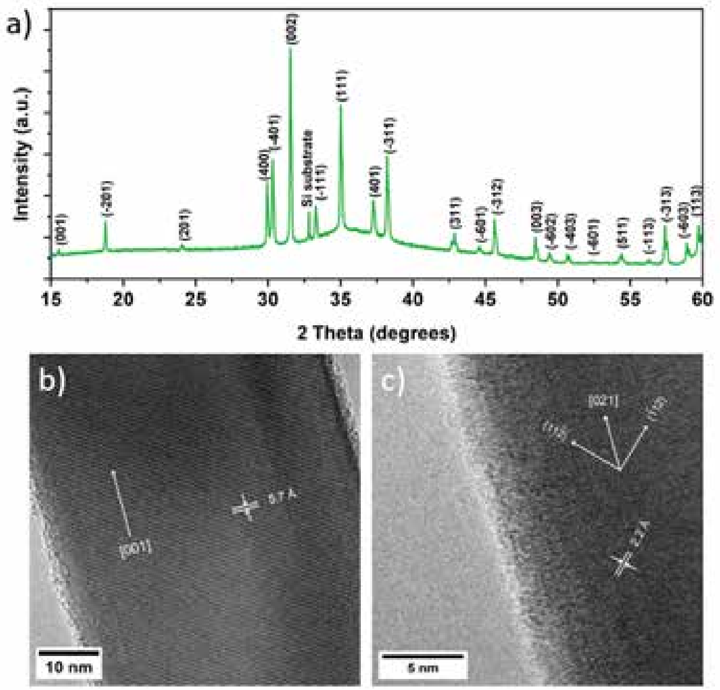

Figure 5.10. (a) X-ray diffraction pattern of β-Ga_2O_3 NWs on Si substrate; (b) TEM image of a β-Ga_2O_3 NW showing an interlayer spacing of 5.7 Å, indicating the [001] growth direction; (c) TEM image of a β-Ga_2O_3 NW showing orthogonal $(11\bar{2})$ & $(\bar{1}12)$ planes with an interlayer spacing of 2.2 Å, indicating the [021] growth direction.

Additionally, the Bragg peak at approximately 33 degrees aligns with the Si substrate (forbidden Si (200) reflection). Furthermore, TEM was employed to examine the inner crystalline structure of individual NWs (refer to *Figure 5.10(b, c)).* The as-grown NWs typically exhibit single-crystalline characteristics without discernible planar structural defects, such as twin boundaries or stacking faults. FFT was applied to the TEM images to identify crystalline planes and ascertain the growth direction of the NWs. Multiple NWs were analysed, revealing more than one growth direction, a common occurrence for β-Ga_2O_3 NWs [147]. For instance, *Figure 5.10(b)* illustrates a NW with an interlayer spacing of 5.7 Å, indicating [001] growth direction, while in another NW, as depicted in *Figure 5.10(c)*, orthogonal $(11\bar{2})$ & $(\bar{1}12)$ planes were identified, with 2.2 Å interlayer spacing, indicating [021] growth direction. The presence of NWs exhibiting various crystalline orientations suggests either the absence of one dominant preferential growth direction due to the low-symmetry monoclinic phase or the involvement of other growth mechanisms alongside VLS.

5.2.2. *In situ* SEM resonance tests

The mechanical properties of Ga_2O_3 NWs were initially assessed through *in situ* SEM resonance tests. A sequence of SEM images in *Figures 5.11(a–c)* illustrates the excitation of the first mode mechanical resonance in a Ga_2O_3 NW, characterized by a length L = 13.23 μm and width w = 102 nm, with a resonant frequency f_1 = 126.75 kHz. Under the influence of a 4V AC voltage applied to the probe, the NW demonstrates noticeable oscillations (see *Figure 5.11(b)*). Upon alignment of the generated frequency with the natural resonance frequency of the NW (see *Figure 5.11(c)*), there is a significant increase in the amplitude of NW oscillations. To ensure the correct identification of the fundamental natural resonance frequency, oscillations at half of the resonance frequency were examined for each NW, instead of parametric or forced resonance. A total of 26 NWs were measured for their resonance frequency. The width

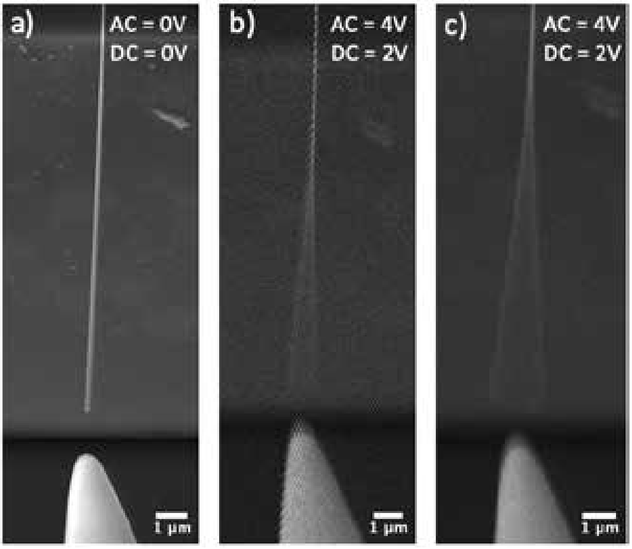

Figure 5.11. SEM images of a NW fixed at one end with a closely positioned probe tip: (a) in the absence of applied AC and DC; (b) showing observable oscillation with 4V AC and 2V DC (non-resonant condition); (c) with 4V AC and 2V DC, demonstrating resonance oscillation.

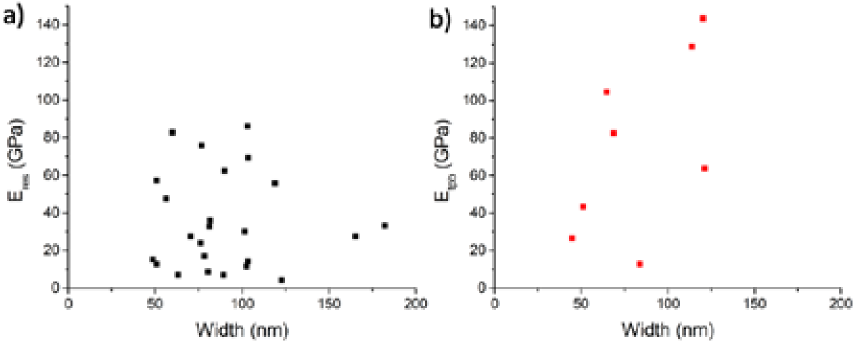

Figure 5.12. Elastic modulus plotted against the width of Ga_2O_3 NWs: (a) derived from SEM resonance examinations; (b) derived from AFM three-point bending experiments. In both cases, widths were determined from SEM images of individual NWs.

of the NWs varied from 48 nm to 183 nm, while the length ranged from 6 to 27 μm, and their resonance frequencies varied from 33 to 770 kHz. In the measurements of horizontal (y-axis) resonance oscillations, only the width of the NW was considered for the calculation of the elastic modulus.

The mean value of the elastic modulus was determined to be $E_{res} = 34.5$ GPa, significantly smaller than the reported Young's modulus for the bulk material. No correlation between the measured elastic modulus values and the geometrical dimensions of Ga_2O_3 NWs was observed (see *Figure 5.12(a)*).

5.2.3. Three-point bending tests

The results of the three-point bending tests, as illustrated in *Figure 5.12*, demonstrate considerable data scattering without a discernible dependence on geometric dimensions, mirroring the findings of the resonance technique. The calculated mean value of the elastic modulus stands at $E_{tpb} = 75.8$ GPa, which falls below the elastic modulus observed for bulk Ga_2O_3.

While the dimensions of the NWs used in the three-point bending tests were measured using SEM, the heights were derived from AFM topography data obtained from the adhered sections of the NWs at each end. In *Figure 5.13(a)*, an SEM micrograph depicts the morphology of a Ga_2O_3 NW positioned atop an inverted pyramid structure, with both ends securely fixed to enable controlled three-point bending experiments. Additionally, *Figure 5.13(b)* presents the AFM topography image of the Ga_2O_3 NW. Given that the elastic modulus is dependent on the NW height to the third power, measurement errors in height can result in significant scattering. Moreover, certain NWs exhibited non-uniform height distributions, for instance, the height of a specific NW can slightly exceed 20 nm at one end but increase to 80 nm at the other end leading to deviations from beam theory and inaccurate elastic modulus calculations in such instances.

5.2.4. Analysis of the measured elastic modulus values

Observing differences in the elastic properties of Ga_2O_3 NWs compared to bulk material, alongside significant data scatter, raises several potential explanations for this variation. Firstly, both experimental and theoretical investigations have highlighted the substantial anisotropy of β-Ga_2O_3 elastic characteristics, suggesting that Young's modulus strongly depends on the crystalline orientation direction [148–150]. This anisotropy, e.g., $E_{100} = 138$ GPa, $E_{010} = 263$ GPa, $E_{001} = 228$ GPa [149], may contribute to the scattering of measured elastic modulus values due to the varied growth directions exhibited by as-grown NWs, as determined through TEM studies.

Secondly, because the elastic modulus relies heavily on the dimensions of the nanostructure (height to the third power for three-point bending, width to the second power, and length to the fourth power for resonance frequency calculations), inaccuracies in measuring these dimensions can introduce scattering effects on the elastic modulus [151]. Furthermore, *Figure 5.14* provides a schematic representation of a β-Ga_2O_3 NW positioned over an etched inverted pyramid on a Si substrate.

The figure includes profile measurements obtained through AFM for a single NW. Notably, the height profile of the specific NW exhibits a variation, starting slightly

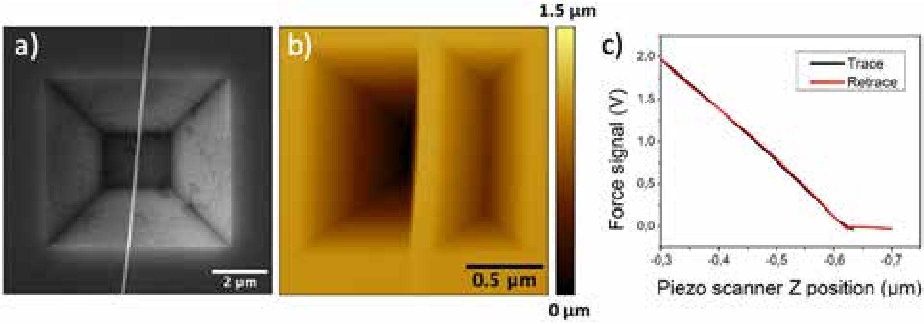

Figure 5.13. (a) SEM image depicting a Ga_2O_3 NW suspended over an inverted pyramid structure with both ends securely fixed; (b) AFM topography image of Ga_2O_3 NW suspended over the inverted pyramid structure with both ends securely fixed, revealing a measured NW height of approximately 23 nm at NW ends; (c) loading and unloading spectra, illustrating one instance of three-point bending test.

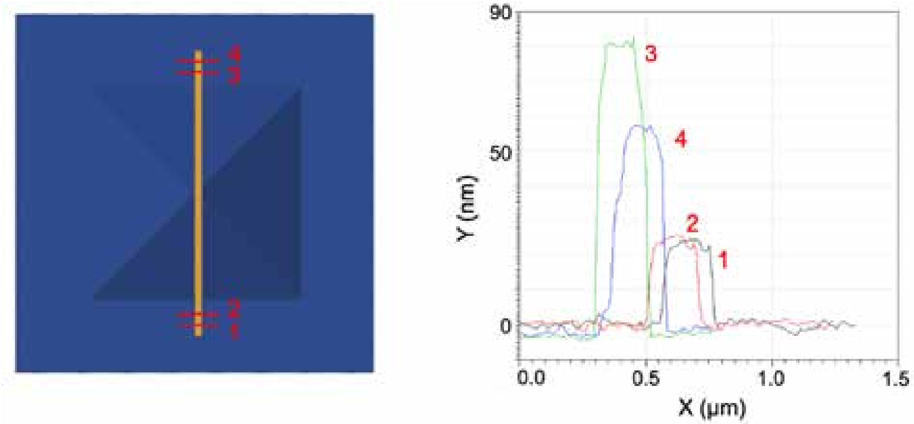

Figure 5.14. Height profiles of a Ga_2O_3 NW.

above 20 nm at one end and increasing to 80 nm at the other end. As depicted in *Figure 5.14*, NW profiles exhibit non-constant geometry, fluctuating within a 60 nm range. This variability, such as height ranging from 20 nm to 80 nm, poses challenges in accurately determining the geometry of the NW within the whole length of the NW.

Additionally, in this study, the effect is further complicated by the fact that β-Ga_2O_3 NW cross-sections often deviate from rectangular geometry (e.g., trapezoid), introducing additional errors to the calculations, which should be minimized through a thorough examination of each individual nanostructure's geometry [152]. The magnitude of the geometric measurement error typically increases significantly for smaller NWs, as the relative measurement error becomes comparable to the absolute value of the dimension, resulting in the overestimation of the elastic modulus, which may be confused with the "size effect" [153]. The onset diameter of this size effect, where the surface contribution towards NW stiffening becomes significant, has been variably reported to be around 10–40 nm and below [153, 154].

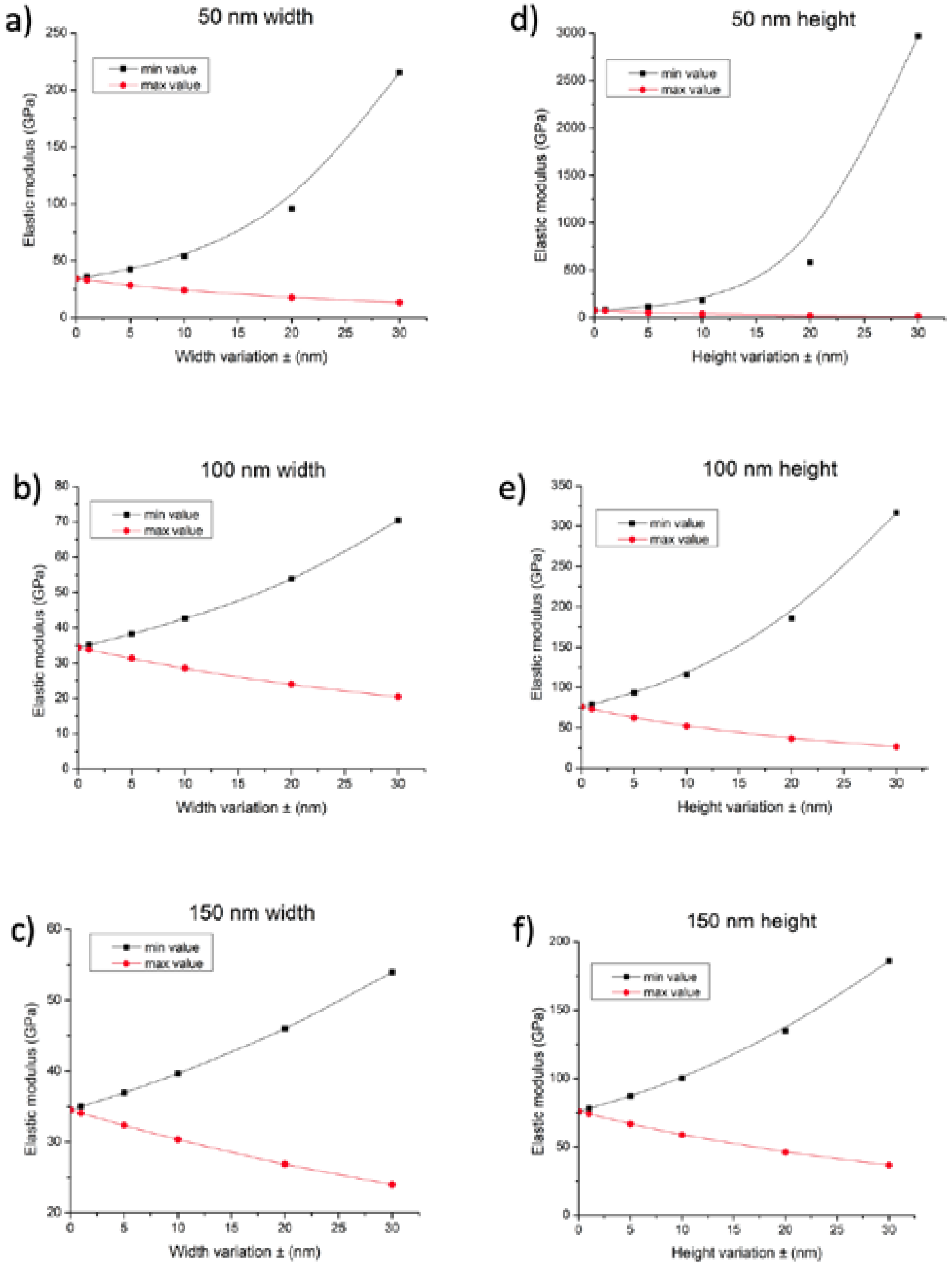

Figure 5.15. Graphs representing cross-section uncertainty error. Variations of width in SEM resonance experiments are shown in (a–c) and for variations of height in AFM three-point bending experiments are shown in (d–f). Elastic modulus values, derived from the minimal and maximal values of width and height, are labelled as “min value” and “max value”, respectively. Lines in graphs are drawn to guide the eye.

However, in this study, most NWs had widths above 50 nm, therefore, variations in elastic moduli from the bulk value due to surface contribution should be negligible. The primary source of error is attributed to non-uniform geometry (dimensions' deviations axially and deviations from rectangular cross-section, e.g., trapezoid). To model variations in elastic modulus, the range of potential geometry deviations, from minimal to maximal values, is considered.

Error simulations of the geometry uncertainty indicated that ± 25 nm width error (SEM method) and ± 15 nm height error (AFM method) for NWs with 100 nm width/height corresponds to the observed scattering in elastic modulus values in *Figure 5.15*. Despite the precision of both SEM and AFM measurements, this analysis suggests that the primary source of error stems from the non-constant cross-sectional geometry of the NW. Variations of elastic modulus depending on variations of width in SEM resonance experiments are shown in *Figure 5.15(a–c)* and for variations of height in AFM three-point bending experiments are shown in *Figure 5.15(d–f)*.

Lastly, point defects, such as oxygen vacancies, can elongate the average bond length, leading to a decrease in the elastic modulus [155–157]. For instance, Wang et al. [158] demonstrated that ZnO NWs with a higher density of oxygen vacancies, determined from photoluminescence measurements, exhibited markedly (up to 20%) lower Young's modulus. Similarly, Wang et al. [159] observed a lower (up to 16%) elastic modulus for Al_2O_3 NBs compared to the theoretical value, attributing this variance to oxygen vacancies within the NBs. In line with the prior investigation [160], as-grown Ga_2O_3 NWs display a prominent photoluminescence band associated with oxygen vacancies, suggesting a substantial concentration of such point defects, which may contribute to their lower elastic modulus values compared to the bulk material. Additionally, planar structural defects like stacking faults can impact the mechanical properties of NWs, although findings indicate that stacking faults can either decrease or increase Young's Modulus [155, 161]. The reduction of Young's Modulus in NWs relative to bulk has been reported to be as significant as threefold in WO_3 NWs [162], four to fivefold in boron NBs [163], and up to tenfold in ZnO NBs. This significant deviation from the bulk value is typically attributed to the growth-direction-dependent concentration of stacking faults and point defects in NWs and NBs, which is correlated with the nanostructure cross-section aspect ratio. For example, in ZnO nanostructures, NWs with lower width-to-height ratios exhibited higher elastic modulus values, while NBs with higher width-to-height ratios displayed a notable decrease in elastic modulus [164].

While the scattering of measured elastic moduli can be attributed to the variation in cross-section geometry and the presence of different growth directions, stemming from the low symmetry of the monoclinic Ga_2O_3 phase and resulting anisotropy in mechanical properties, the underlying cause of the significant decrease compared to the bulk value remains uncertain. An earlier investigation of the as-grown Ga_2O_3 NW photoluminescence [160] suggested a possibility of high concentration of oxygen vacancies, which could contribute to the lower elastic modulus values. TEM studies conducted on a few selected NWs did not reveal the presence of stacking faults, which might enhance elasticity. Nonetheless, to gain a comprehensive understanding of the diverse factors influencing the elastic properties of Ga_2O_3 NWs, further research involving individual nanostructures with advanced combinatory methods, such as *in situ* TEM mechanical resonance, is warranted to accurately determine geometrical parameters, crystalline orientation, and the presence of planar defects.

5.2.5. Summary

The elastic moduli of individual β-Ga_2O_3 NWs were experimentally determined using two techniques: three-point bending and mechanical resonance. The mean values obtained were 34.5 GPa from resonance and 75.8 GPa from three-point bending methods, respectively. The observed data exhibited significant scattering, attributed to variations in cross-section geometry and the presence of different growth directions, stemming from the low symmetry of the monoclinic Ga_2O_3 phase and resulting anisotropy in mechanical properties. This study underscores the necessity for precisely controlled synthesis methods for β-Ga_2O_3 NWs and thorough post-examination of their mechanical properties before considering their application in future nanoscale devices.

As the three-point bending method yields values closer to those of bulk material, it could be considered a more precise method for determining the elastic modulus of NWs. However, this is not definitive, as both methods have their advantages and disadvantages. SEM resonance measurements are conducted in a vacuum and only account for two dimensions of the NW – width and length – without determining height. A disadvantage of the resonance method is the potential for carbon deposition within the SEM chamber during measurements. On the other hand, AFM also considers height, but width is determined from SEM images, which can affect the measurement accuracy of the NW. Therefore, it can be concluded that the methods are not directly comparable.

5.3. Heat-induced fragmentation and adhesive behaviour of Au nanowires

Au NPs have gained increasing popularity in SERS applications [165–167]. Their remarkable stability in various environments, including high temperatures and pressures, makes them versatile tools in SERS measurements. They are easily fabricated and find applications across diverse fields, from sensing [168] to drug delivery [169]. Au NPs amplify Raman scattering efficiency by several orders of magnitude [170], enabling highly sensitive detection of minute amounts of molecules.

In this section, the effect of heating schemes and temperature on the formation of Au NW fragments, along with the adhesive behaviour of NPs produced through this approach, was investigated. Additionally, the feasibility of heat-induced Au NW fragmentation for patterned SERS substrate was evaluated. The findings presented in this section have been published in **Paper III**.

5.3.1. Thermal annealing of Au nanowires

The thermal behaviour of NWs was explored through controlled heating processes using a laboratory furnace in air atmosphere. Au NWs underwent two distinct heating schemes to understand their response to temperature changes and structural alterations.

In the **first scheme**, the same NW sample was gradually heated from 300 °C to 600 °C in 50 °C increments, with each temperature step lasting 30 minutes. The NW

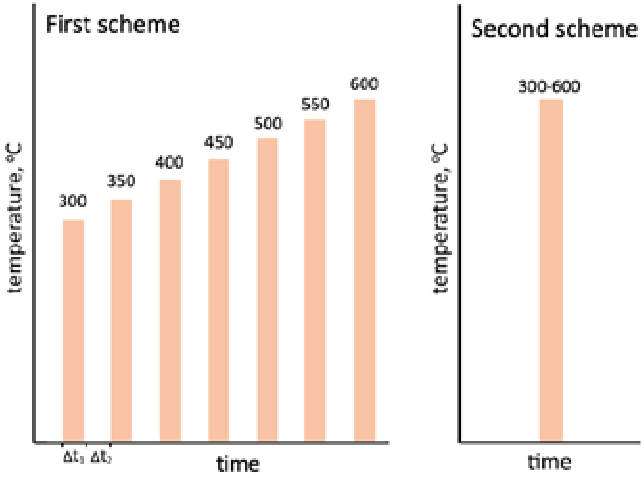

Figure 5.16. The heating schemes employed for the heat treatment of Au NWs. Δt_1 represents the 30 min duration of heat treatment, while Δt_2 indicates the cooling down and SEM imaging period, approximately 1h.

sample was placed into the furnace once it had been heated to the desired temperature. Following each heating cycle, samples were taken out of furnace, cooled down and SEM imaging was performed to examine the sample.

The **second scheme** involved rapid heating, utilizing a fresh sample for each experiment to accurately determine the temperature at which fragmentation begins. Heating was conducted between 300 °C and 600 °C, each for a duration of 30 minutes. Both heating schemes are illustrated in *Figure 5.16* for clarity.

5.3.2. Au nanoparticle characterisation

The SEM analysis was conducted on as-synthesized Au NWs and Au NRs. The width and length of both NWs and NRs were systematically measured to understand their physical characteristics and variability. The data revealed that the average length of the observed NRs (see *Figure 5.17(a)*) was 83.5 nm, with a standard deviation (SD) of 9.4 nm, indicating a range of length differences within the sample. Moreover, the NRs exhibited an average width of 18.4 nm, with a SD of 1.4 nm, indicating variability in width. On the other hand, the average length of the observed NWs (see *Figure 5.17(b)*) was found to be 1.9 µm, with a SD of 0.7 µm. Additionally, the NWs showed an average width of 50.5 nm, with a SD of 5.5 nm. These results emphasize the relatively consistent length of the NWs while demonstrating a slightly greater variability in their width.

A controlled gradual heating process was applied to the same NW sample, raising the temperature from 300 °C to 600 °C in 50 °C increments and maintaining a consistent duration of 30 minutes at each temperature step (the first heating scheme). In the SEM micrographs provided (see *Figure 5.18*), it is apparent that both the NRs and NWs demonstrate a tendency to decrease in length and increase in width due

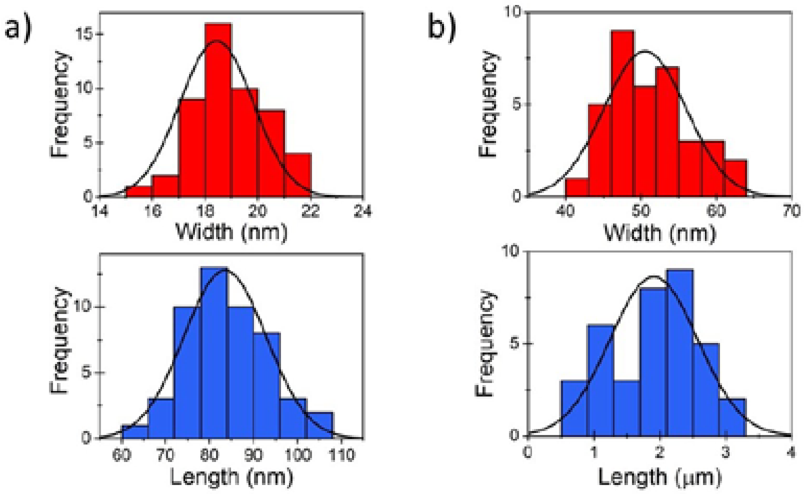

Figure 5.17. Size distribution of as-prepared: (a) Au NRs; (b) Au NWs.

to the diffusion of Au atoms. Notably, visible alterations in morphology are observed in both types of nanostructures at 400 °C. The temperature range spanning from 400 °C to 500 °C represents a period of particularly rapid transformations in both NRs and NWs.

To establish statistical validity, the dimensions of the nanostructures were systematically measured after each heating cycle (the first heating scheme). Upon analysing the nanostructure measurements, it became evident that with the gradual increase in heating temperature, the length of the structures decreased while the width increased. Around 550 °C, NRs (see *Figure 5.19(a)*) showed a tendency to transition into a more thermodynamically stable state, forming nanospheres. A similar phenomenon was observed with NWs (see *Figure 5.19(b)*), where they also exhibited a tendency to form nanospheres under comparable conditions. NWs with a significant length-to-width ratio have a higher aspect ratio, indicating that their length is much greater than their width. At lower temperatures, all atoms are constrained to vibrational motion around their equilibrium positions, ensuring that the NW retains its original structure and shape. As the temperature rises above 500 °C, the diffusive activities of atoms in the surface region become significant. Rearrangement and diffusion of surface atoms into a spherical configuration are processes facilitated by the first heating scheme, allowing sufficient time for these transformations to take place.

The second heating scheme aimed to explore the fragmentation behaviour of Au NWs under different temperature conditions. Fragmentation of metal NWs into shorter segments at elevated temperatures is a well-known phenomenon referred to as Rayleigh instability. This process occurs through the diffusion of surface atoms and is driven by the minimization of surface energy, leading to the formation of faceted fragments predominantly bounded by {111} surfaces. Initially, the surfaces of pentagonal Au wires are {100}, but they transition to the more energetically favorable {111} surfaces at the wire ends. Consequently, the NW breaks into multiple fragments or NRs.

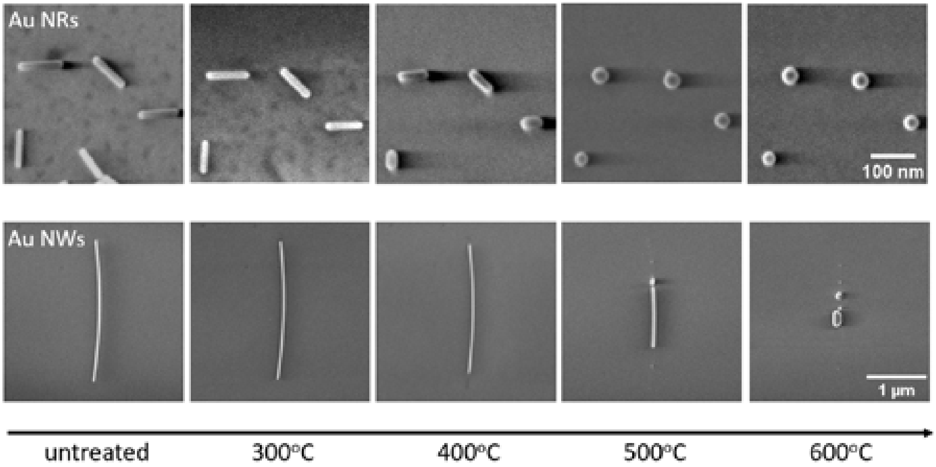

Figure 5.18. SEM micrographs of untreated and gradually thermally annealed (first heating scheme) Au NRs and NWs.

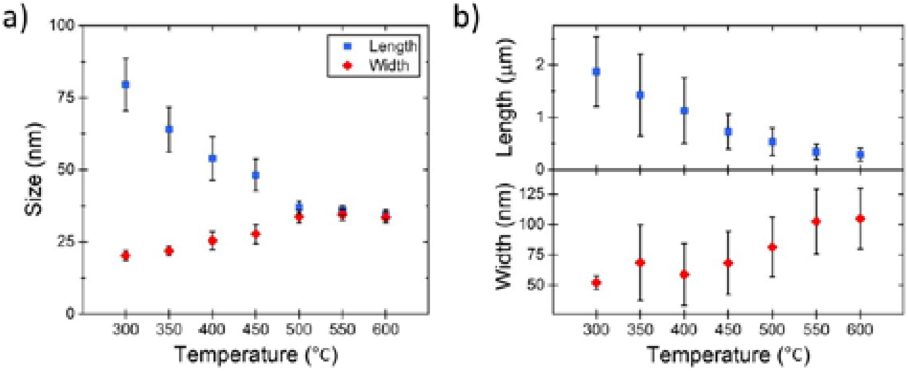

Figure 5.19. Change in particle size depending on the heating temperature for: (a) Au NRs; (b) Au NWs.

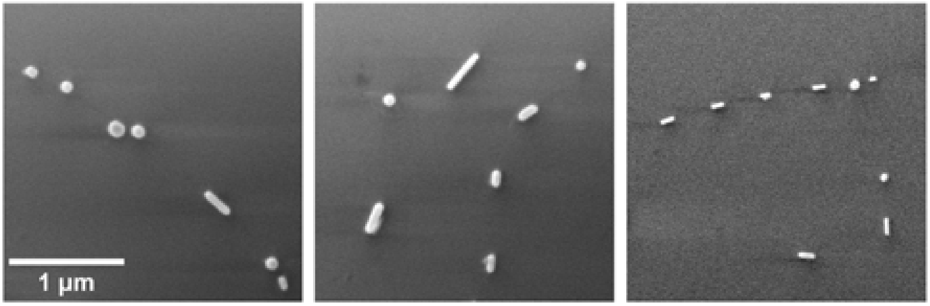

Figure 5.20. SEM micrographs of rapidly heated (the second heating scheme) NWs at 600 °C for 30 min.

Previous experiments have indicated that gradual heating allows more time for diffusion-induced shape changes, resulting in NWs transforming into nanospheres instead of fragmenting into several pieces. As depicted in *Figure 5.20*, it is evident that when rapidly heated to 600 °C for 30 minutes using the second scheme, Au NWs are fragmented into smaller segments, exhibiting periodic spacing between these fragmented sections.

5.3.3. AFM measurements

Exploring the creation of robust SERS substrates requires ensuring strong adhesion of NPs to the substrate surface, preventing their displacement or removal by dye-containing solutions. In this regard, AFM manipulations were employed to assess whether the NPs, produced through the second heating scheme at 600 °C, achieved sufficient adhesion to the substrate (*Figure 5.21*).

The mobility of the Au NPs was evaluated by measuring the power dissipated in tapping-mode AFM, a technique previously demonstrated to be effective for assessing NP mobility. The heat-induced rounding of NPs is expected to reduce the contact area, thereby decreasing friction forces, in line with the established relationship $\tau = F/A$, where τ represents contact strength, F denotes friction force, and A signifies contact area. A total of over 400 Au NPs were measured, and approximately 83.7% of these NPs showed no mobility under AFM manipulations. In *Figure 5.21*, the topography images depict the changes in fragmented Au NWs on the Si substrate before (see *Figure 5.21(a)*) and after (see *Figure 5.21(b)*) AFM manipulations, illustrating the impact of manipulations on NP arrangement and adhesion. The median power dissipated for moving a NP was 0.13 pW. These results underscore the efficacy of the proposed fabrication approach in producing stable SERS substrates with well-adhered NPs.

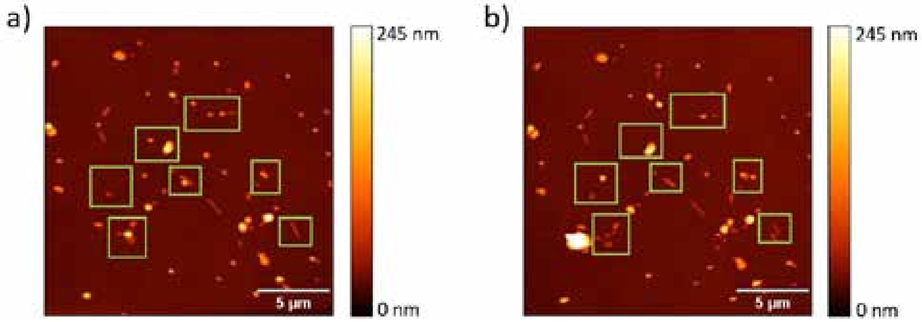

Figure 5.21. A topography image shows a 20 × 20 µm region of thermally annealed (600°C) Au NWs on the Si substrate: (a) before AFM manipulations; (b) after AFM manipulations. The green frames highlight the areas where NP displacement occurred.

5.3.4. Raman measurements

Raman measurements of Rhodamine B molecules adsorbed on a Si wafer surface were explored using Au NWs and NRs before and after thermal annealing (see *Figure 5.22*).

Despite optimizing the excitation wavelength for Rhodamine B, no significant Raman peaks associated with it were detected on the bare Si wafer surface. To enhance the Raman signal of Rhodamine B, Au NWs and NRs before and after thermal annealing at 600 °C were introduced onto the Si wafer surface. Substrates with as-prepared Au NRs and NWs displayed the main SERS peaks of Rhodamine B at 621, 1278, 1356, 1507, and 1526 cm^{-1}. Measurements for substrates with thermally annealed NRs and NWs showed an increased Raman signal for Rhodamine B, evident from the amplified Raman peaks observed in the spectra. Raman spectra of the heated NWs exhibited significantly higher intensities compared to the heated NRs. Calculated EFs showed a substantial improvement through annealing at 600 °C. Specifically, the EF for Au NRs increased from $3{,}8 \times 10^5$ to $8{,}3 \times 10^5$ after annealing, while for annealed Au NWs, it reached $1{,}6 \times 10^6$, representing nearly a 30-fold increase compared to unannealed NWs with an EF of $5{,}5 \times 10^4$.

The EF for NRs exceeded that of NWs by a factor of 7 before annealing. Additionally, the initial average diameter of NWs was nearly three times larger than that of NRs. Following annealing, the diameters of both types of NPs increased, resulting in a larger surface area and enhancing the Raman signal. Interestingly, the fragments

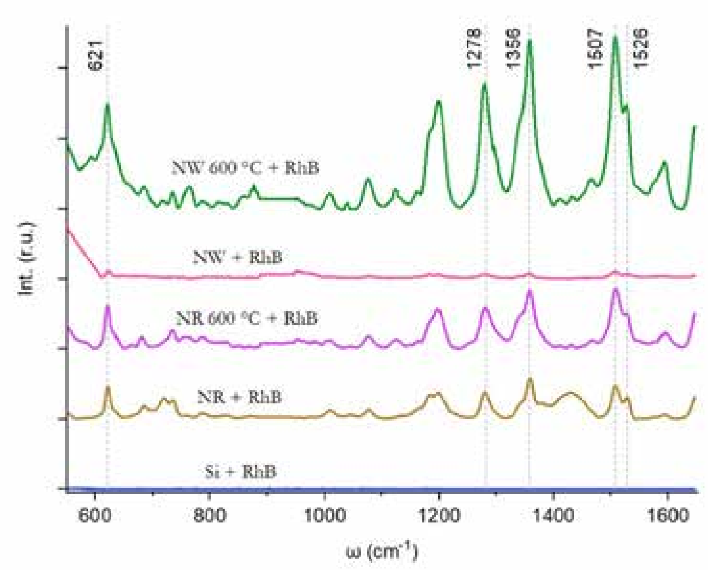

Figure 5.22. Raman scattering from Rhodamine B molecules on an oxidized Si wafer in the presence of untreated and thermally treated Au nanostructures.

derived from NWs were larger than the NPs formed from NRs. After annealing, NWs became approximately 2 times more efficient for SERS enhancement compared to NRs, likely due to their larger diameter. Thermal annealing of Au NRs led to larger and more distributed nanospheres, while rapid NW annealing at higher temperatures produced more NPs in a patterned fashion. From the data obtained, it can be inferred that shape and size are the main factors responsible for the SERS effect, consistent with previous literature [171, 172]. Benz et al. identified size and shape as key parameters for SERS enhancement of Au NPs, with enhancement growing with particle size and spherical particles being more effective in SERS enhancement compared to faceted particles [173]. Annealing changed both size and shape, making NPs bigger and more spherical, resulting in stronger SERS enhancement.

5.3.5. Summary

In this study, heat-induced fragmentation of Au NWs was effectively employed, demonstrating its potential as a reliable method for fabricating SERS substrates. Two distinct heating schemes were applied to Au NWs to understand their thermal behaviour and structural transformations. The first scheme was gradual heating of the same NW sample from 300 °C to 600 °C in 50 °C increments, with each temperature held for 30 minutes, revealing the evolution of NR and NW shapes. However, this method did not result in NW fragmentation. The second approach involved rapid heating from room temperature to target temperatures (300 °C, 400 °C, 500 °C, and 600 °C), followed by a 30-minute hold before cooling. Using this method, fragmentation of Au NWs was achieved. Significant morphological changes in NWs and NRs were observed through SEM, transitioning into nanospheres and NRs at elevated temperatures. AFM measurements confirmed the strong adhesion of NPs to the substrate, while Raman spectroscopy highlighted a substantial enhancement in the SERS effect, particularly for fragmented NWs heated at 600 °C for 30 minutes. Considering the relatively low cost of synthesizing and depositing Au NPs and the large number of substrates with a high EF that can be produced, this method is highly effective and cost-efficient for achieving strong Raman signals, even for small concentrations of substances.

5.4. Heat-induced morphological changes in Ag nanowires

In this section, the experimental outcomes of the Ag NWs deposited onto specially patterned Si substrates and subsequent heating of the samples to various temperatures in an air environment are presented. The contrasting behaviours between the suspended and adhered parts of Ag NWs during heating are examined. Additionally, in order to support the experimental findings, MD and finite element method (FEM) simulations were employed. The findings presented in this section have been published in **Paper IV**.

5.4.1. Heat treatment of the Ag nanowires

The thermal behaviour of Ag NWs was explored through controlled heating processes using a laboratory furnace. Two heating schemes were employed in this study. **Scheme 1** (see *Figure 5.23*) involved heating in 10-minute cycles at fixed temperatures followed by cooling to room temperature. The initial cycle commenced at 100 °C, with subsequent increments of 50 °C until reaching 200 °C. Further temperature increases were set at 25 °C intervals until reaching 450 °C.

Scheme 2 entailed heating freshly made samples in a single step for 10 minutes at a target temperature determined based on the results obtained from Scheme 1. The heat-treatment experiments, conducted under both heating schemes, were repeated twice using freshly prepared samples and following the same protocol for each scheme.

5.4.2. First heating scheme

There were no observable alterations in the morphology of Ag NWs at heat-treatment temperatures up to 275 °C. However, at 300 °C and above, initial signs of diffusion in NWs became apparent, characterized by splitting at locations where NWs were partially fractured during deposition (refer to *Figure 5.24*). At this stage, there was no observable distinction in the behaviour of adhered and suspended parts of NWs concerning structural integrity. The primary influential factor observed in the process was the diameter of the NWs. Generally, thinner NWs exhibited an earlier onset of diffusion.

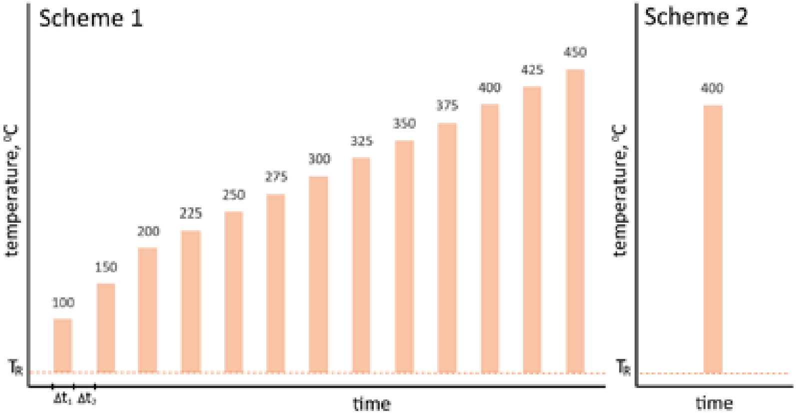

Figure 5.23. The heating schemes employed for the heat treatment of Ag NW. T_R denotes room temperature, Δt_1 = 10 min represents the duration of heat treatment, while $\Delta t_2 \approx$ 1 h indicates the resting period.

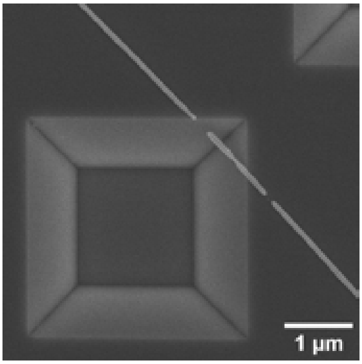

Figure 5.25. Splitting and necking of Ag NWs in the Scheme 1 after treatment at 375 °C.

Between 350 °C and 375 °C, many Ag NWs exhibited necking and complete splitting approximately in the middle of their suspended segments (see *Figure 5.25*). Beyond 400 °C, fragmentation extended to the adhered parts. This observation suggests that in heating Scheme 1, the adhered portions demonstrate greater heat resistance, enduring temperatures around 50 °C higher before fragmentation occurs compared to the suspended segments.

By 450 °C, most NWs experienced splitting in their suspended sections, with extensive fragmentation also evident in the adhered segments. NWs below 120 nm generally displayed a higher susceptibility to necking and splitting, while NWs above average 120 nm diameter exhibited greater resistance to elevated temperatures.

5.4.3. Second heating scheme

In Scheme 2, the initial stage of NW fragmentation was observed, particularly significant for analysing the response of adhered and suspended sections to heat treatment, within the temperature range of 375–400 °C (*Figure 5.26*).

Contrary to observations in Scheme 1, the behaviour of partially suspended NWs in Scheme 2 displayed a distinct pattern. Specifically, extensive fragmentation occurred in the adhered portions while the suspended segments remained intact (see *Figure 5.26*). This phenomenon was most prominent in samples treated at 400 °C, thus this temperature was selected for further investigation. Beyond this temperature, widespread fragmentation was observed in both adhered and suspended regions. Consistently, the results indicated a tendency for splitting to occur first in the middle of the suspended parts for heating Scheme 1, and in the adhered parts for heating Scheme 2.

To quantitatively assess the degree of splitting in both the adhered and suspended parts of Ag NWs, two parameters were introduced: "splits per part", representing the total number of split events separately for the adhered and suspended parts of each NW, and "splits per unit length", indicating the number of split events per length of either the adhered or suspended part. The number of splits was determined from SEM images of large areas (approximately 120 × 80 µm) captured at maximum picture resolution (6144 × 4415). This approach ensured an unbiased analysis, with all NWs

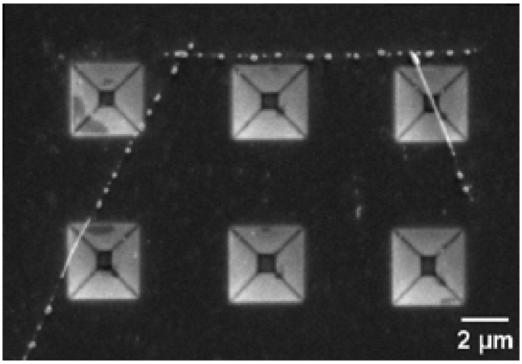

Figure 5.26. SEM image depicting Ag NWs following a single-step heat treatment (Scheme 2) at 400 °C. Fragmentation of the NWs predominantly occurred within the adhered sections.

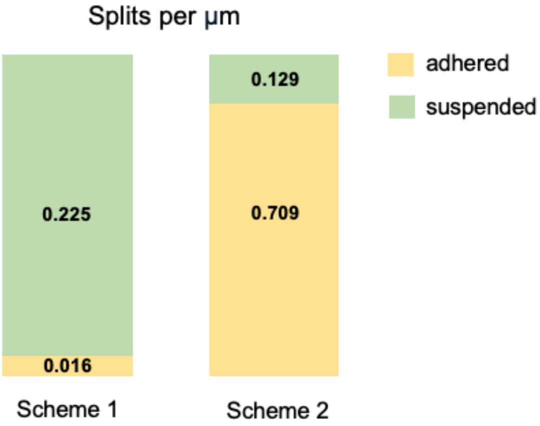

Figure 5.27. Mean values of split occurrences per unit length in both adhered and suspended parts for each heating scheme from multiple SEM images.

within the large areas being examined. Subsequently, average values for all analysed NWs were calculated separately for each heating scheme. In total, 111 adhered parts and 101 suspended parts were analysed for heating Scheme 1, and 87 adhered parts and 64 suspended parts for heating Scheme 2. The normalized results of the statistical analysis are presented in *Figure 5.27*. In heating Scheme 1, the extent of fragmentation in the suspended parts is one order of magnitude higher than that in the adhered parts, while the opposite behaviour is observed for the second heating scheme.

5.4.4. Inner structure of Ag nanowires

The Ag NWs used in this investigation exhibit a five-fold twinned crystal configuration, resulting in a pentagonal cross-sectional shape [174]. This pentagonal symmetry, considered a “forbidden” pattern in crystallography, inherently induces internal strains within the structure. These strains may act as a potential driving force leading to the heat-induced fragmentation of Ag NWs, serving as a mechanism for stress release and possibly involving recrystallization into single crystals. To assess this hypothesis, further experiments were conducted using TEM grids, allowing for the observation of the crystal structure in TEM. Remarkably, it was observed that even in the case of small fragments resulting from heat treatment, the pentagonal structure remained intact, as illustrated in *Figure 5.28*. It is noteworthy that the fragments remained in position due to contact with the thin carbon membrane of the TEM grid. This discovery suggests that the morphological alterations induced by heat in Ag NWs occur through surface diffusion mechanisms without compromising the crystal structure.

5.4.5. Mechanisms behind the heat-induced Ag nanowire splitting

Given the findings, critical factors affecting the outcomes of heat-treatment investigations include the substantially higher thermal expansion coefficient of Ag compared to Si (18.9 vs 2.8 × 10^{-6} m/(m °C)), and studies by Vlassov et al. [175] indicating strong bonding between Ag NWs and Si substrates. These factors suggest that thermal expansion of Ag NWs could induce significant mechanical stresses within the NWs, particularly at the interface with the Si substrate, potentially leading to the redistribution of Ag atoms and splitting of the NWs to relieve stress.

FEM simulations conducted in collaboration with the Institute of Technology at the University of Tartu confirmed high stresses at the NW-substrate interface and in the middle of suspended segments, providing qualitative insights into potential thermomechanical phenomena. Repeated heat-induced bending could induce fatigue and defect formation in the suspended segment, increased by heat-assisted rearrangement of Ag atoms at the substrate contact. This could lead to defects and necking in the middle of the suspended segment, consistent with experimental observations. Diffusion of atoms away from defect regions may thin the NW, potentially

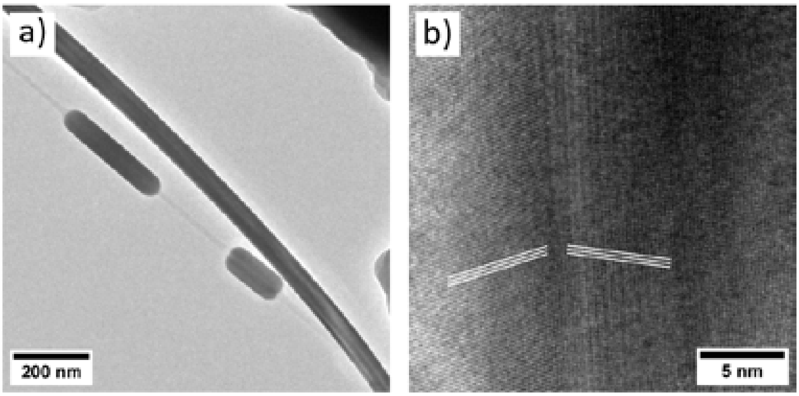

Figure 5.28. TEM micrographs of: (a) Ag NWs post single-step (Scheme 2) heat treatment; (b) inset highlighting one of the segments. The dark lines observed in the middle of the NWs correspond to a twin boundary between two crystal segments.

causing splitting before other regions, proposing a mechanism for NW splitting during heat treatment.

In Scheme 2, without heating cycles, the suspended parts are not subjected to repeated compression and tensile stresses. Similar to the general behaviour observed with heated Ag and Au NWs on flat Si substrates [176], the adhered parts split into shorter fragments. This phenomenon is commonly attributed to Rayleigh instability [95, 177, 178]. The longer endurance of suspended parts in these experiments suggests that interfacial stresses play a significant role in the fragmentation process. Moreover, in certain cases, surviving parts extend beyond the visible suspended portion, possibly due to heat-induced bending. Additionally, MD simulations, conducted with the Institute of Technology at the University of Tartu explored stress-induced defect impact on NW splitting, revealing that heating and cooling cycles in a periodic prismatic rod model with a five-fold twinned structure caused defect formation and amorphous regions, leading to necking and splitting.

5.4.6. Summary

This study investigated the effect of heat treatment on pentagonal Ag NWs partially in contact with a substrate. NWs were deposited on patterned Si substrates with varying hole sizes, resulting in some NWs partially suspended over these holes. When the temperature was increased incrementally in rapid cycles (Scheme 1), NWs split at 375 °C primarily in suspended parts, while under direct temperature increase (Scheme 2), fragmentation mainly occurred in adhered parts. Fragmentation in both parts was observed at temperatures exceeding 400 °C, attributed to thermal expansion and frictional forces. Experimental findings aligned with simulations, suggesting that heat-induced NW fragmentation involves substrate interaction beyond Rayleigh instability.

6. CONCLUSIONS

In this Dissertation, the main objective was to investigate mechanical and thermal behaviours of selected material NWs using electron microscopy nanomanipulation techniques and heating experiments.

A significant advancement in the field was achieved with the first observation of mechanically induced post-synthesis kinking in non-metallic NWs. Through three different manipulation scenarios and MD calculations, the mechanical induction of kinking and unkinking in CuO NWs was successfully demonstrated. Structural analyses using high-resolution TEM and SAED, alongside kinking angle measurements, revealed that the observed kinking in CuO NWs corresponds to twinning along the $(\bar{1}10)$ crystal plane of CuO. The findings suggest that deformation twinning may occur when external forces are applied in a specific direction. This newly discovered phenomenon opens a new route for research into post-synthesis modifications of other non-metallic NWs.

The experimental determination of the elastic moduli of individual β-Ga_2O_3 NWs using both three-point bending and mechanical resonance techniques revealed significant scattering in the obtained data. The mean values obtained were 34.5 GPa from resonance and 75.8 GPa from three-point bending methods, highlighting the challenges posed by variations in cross-section geometry and the presence of different growth directions of the β-Ga_2O_3 NWs. The observed scattering of the values of elastic moduli of individual β-Ga_2O_3 NWs underscores the necessity for precisely controlled synthesis methods for β-Ga_2O_3 NWs and thorough post-examination of their mechanical properties.

Significant differences in the thermal behaviour and structural transformations of Au NWs were observed between the two heating schemes, with the gradual heating method showing morphological changes without fragmentation, whereas the rapid heating method led to fragmentation and the formation of nanospheres and nanorods at elevated temperatures, highlighting the effectiveness of rapid heating for inducing fragmentation in Au NWs. These findings highlight the effectiveness of using fragmented Au NWs in applications such as SERS substrates.

Heat treatment-induced fragmentation of Ag NWs revealed distinct fragmentation patterns depending on the method of temperature increase, with NWs splitting primarily in suspended parts at 375 °C in rapid cycles and fragmentation occurring mainly in adhered parts under direct temperature increase, highlighting the role of substrate interaction in the fragmentation process. Experimental observations, supported by simulations, demonstrated that thermal expansion and frictional forces contribute to the fragmentation of pentagonal Ag NWs, with fragmentation occurring at temperatures exceeding 400 °C, suggesting that heat-induced NW fragmentation involves substrate interaction beyond Rayleigh instability. Continuous research into metal NW fragmentation under varying conditions and substrates could enhance control in cost-effective production methods for applications involving metal nanostructure arrays.

To sum up, the mechanical properties and thermal behaviour of NWs were investigated. Through manipulation techniques and heating experiments, significant advancements were made in understanding the structural transformations and heat-induced behaviour of NWs. These findings underscore the crucial role of manipulation methods and substrate interactions in determining the properties of nanostructures, essential for their potential applications.

7. THESES

1. Post-synthesis kinking of single-crystal CuO nanowires can be induced by mechanical manipulations, with deformation twinning along the $(\bar{1}10)$ crystal plane being the underlying mechanism.
2. The elastic modulus of β-Ga_2O_3 nanowires was determined using *in situ* scanning electron microscopy resonance and three-point bending atomic force microscopy techniques, yielding mean values of 34.5 GPa and 75.8 GPa, respectively. Variations in cross-section geometry and different growth directions contribute to the scattering of these elastic modulus values. These methods are reliable for accurate nanowire elastic modulus measurement required for nanodevice engineering.
3. The heat-induced fragmentation of Au and Ag nanowires is affected by the manner in which temperature is raised, with fewer splits per nanowire length observed during rapid heating cycles, while direct temperature elevation results in more splits per nanowire length. The controlled fragmentation of Au nanowires results in periodic, cost-effective, and easily producible substrates for surface-enhanced Raman scattering.
4. Fragmentation of suspended Ag nanowire parts is dominant when heated incrementally in rapid cycles, while fragmentation of the adhered parts primarily occurs under direct temperature elevation, which is caused by mechanical stresses that arise in nanowires as an interplay between thermal expansion and frictional forces. Ag nanowires remain morphologically stable up to 275 °C, thus Ag nanowire networks can be safely used up to 275 °C, beyond which fragmentation begins to occur.

LIST OF PUBLICATIONS

Included in dissertation

I Vlassov, S., Oras, S., **Trausa, A.**, Tiirats, T., Butanovs, E., Polyakov, B., Zadin, V. and Kyritsakis, A., 2024. Reshaping covalent nanowires by exploiting an unexpected plasticity mediated by deformation twinning. *Small, 20(1)*, p. 2304614.

II **Trausa, A.**, Oras, S., Vlassov, S., Antsov, M., Tiirats, T., Kyritsakis, A., Polyakov, B. and Butanovs, E., 2024. Elastic Modulus of β-Ga_2O_3 Nanowires Measured by Resonance and Three-Point Bending Techniques. *Beilstein J. Nanotechnol, 15,* p. 704–712.

III **Trausa, A.**, Tipaldi, C. F., Ignatane, L., Polyakov, B., Oras, S., Butanovs, E., Vanags, E. and Smits, K., 2024. Heat-Induced Fragmentation and Adhesive Behaviour of Gold Nanowires for Surface-Enhanced Raman Scattering Substrates. *ChemEngineering, 8(1)*, p. 15.

IV Damerchi, E., Oras, S., Butanovs, E., Liivlaid, A., Antsov, M., Polyakov, B., **Trausa, A.**, Zadin, V., Kyritsakis, A., Vidal, L., Mougin, K., Pikker, S. and Vlassov, S., 2024. Heat-induced morphological changes in silver nanowires deposited on a patterned silicon substrate. *Beilstein J. Nanotechnol. 15,* p. 435.

Other publications

Tipaldi, C.F., Vitols, K., Kokis, T., Trausa, A. and Sarakovskis, A., 2024. Experimental and Theoretical Comparison and Analysis of Surface-Enhanced Raman Scattering Substrates with Different Morphologies. *Applied Sciences, 14(19),* p. 9040.

Polyakov, B., Kadiwala, K., Butanovs, E., Dipane, L., Trausa, A., Bocharov, D. and Vlassov, S., 2024. Synthesis of $ZnS/Al_2O_3/TaSe_2$ Core/Shell Nanowires Using Thin Ta Metal Film Precursor. *ChemEngineering, 8(1)*, p. 25.

Vanags, E., Bite, I., Ignatane, L., Ignatans, R., Trausa, A., Tipaldi, C. F., Vilks, K. and Smits, K., 2024. Zinc Oxide Tetrapods Doped with Silver Nanoparticles as a Promising Substrate for the Detection of Biomolecules via Surface-Enhanced Raman Spectroscopy. *ChemEngineering, 8(1)*, p. 19.

Manika, I., Krasta, T., Maniks, J., Bikse, L., Susinska, J., Leimane, M., **Trausa, A.**, Grants, R. and Popov, A.I., 2023. Effect of ion-induced nuclear reactions on structure modification and radiolysis in LiF irradiated by 410 MeV 36S ions. *Optical Materials, 138*, p. 113686.

PARTICIPATION IN SUMMER SCHOOLS AND CONFERENCES

Summer schools and courses

1. Summer school “European School on Nanosciences & Nanotechonologies (ESONN)”, Grenoble, France, 27th of August – 9th of September, 2023.
2. Summer school “Training School on the MecaNano challenges”, Rome, Italy, 24–28th of July, 2023.
3. Royal Microscopy Society “Electron Microscopy Spring School”, Leeds, UK, 17th–21st of April, 2023.
4. FM&NT-NIBS 2022 summer school “Advanced topics on material spectroscopy and morphology”, Riga, Latvia, 2nd–3rd of June, 2022.
5. Online European course for PhD students and young researchers “HERCULES European School 2022”, 28th of February – 1st of April, 2022.
6. Online summer school “Micro- and nanofabrication of electronic and photonic devices”, LU CFI, RISE and KTH, 17–18th of June, 2021.

Conferences

1. International conference “Functional materials and Nanotechnologies-2024” & “Nanotechnology and Innovation in the Baltic Sea Region – 2024”. Oral presentation: “Elastic Modulus of β-Ga_2O_3 Nanowires Measured by Resonance and Three-Point Bending Techniques”, Tartu, Estonia, 6–9th of October, 2024. Received “Young Scientist Award”.
2. International conference “9th European Nanomanipulation Workshop”. Poster presentation: “Elastic Modulus of β-Ga_2O_3 Nanowires Measured by Resonance and Three-Point Bending Techniques”, Madrid, Spain, 17–19th of June, 2024.
3. The 40th Scientific Conference of the Institute of Solid State Physics, University of Latvia. Oral presentation: “Reshaping covalent nanowires by exploiting an unexpected plasticity mediated by deformation twinning”, Riga, Latvia. 5–7th of March, 2024.
4. International conference “EMRS Fall Meeting 2023”. Poster presentation: “Heat-induced Fragmentation of Gold Nanowires for Surface Enhanced Raman Scattering Substrates”, Warsaw, Poland. 18th–21st of September, 2023.
5. International conference “EMRS Fall Meeting 2022”. Poster presentation: “Au nanoparticle covered ZnO nanostructure substrates for SERS application”, Warsaw, Poland. 19th–22nd of September, 2022.
6. “Joint International Conference ‘Functional Materials and Nanotechnologies’ and ‘Nanotechnology and Innovation in the Baltic Sea region’ – FM&NT – NIBS 2022”. Poster presentation: “SERS substrates based on gold nanoparticle-coated ZnO tetrapods”, Riga, Latvia. 3rd–6th of June, 2022.
7. International conference “XXV General Assembly and Congress of the International Union of Crystallography – IUCr 2021”, Prague, Czech Republic, 14th–22nd of August, 2021.

REFERENCES

[1] W. L. F. Armarego, "Nanomaterials," in *Purification of Laboratory Chemicals*, Elsevier, 2022, pp. 586–630. doi: 10.1016/B978-0-323-90968-6.50005-9.

[2] N. Baig, I. Kammakakam, and W. Falath, "Nanomaterials: a review of synthesis methods, properties, recent progress, and challenges," *Mater Adv*, vol. 2, no. 6, pp. 1821–1871, 2021, doi: 10.1039/D0MA00807A.

[3] B. Mekuye and B. Abera, "Nanomaterials: An overview of synthesis, classification, characterization, and applications," *Nano Select*, vol. 4, no. 8, pp. 486–501, Aug. 2023, doi: 10.1002/nano.202300038.

[4] P. C. McIntyre and A. Fontcuberta i Morral, "Semiconductor nanowires: to grow or not to grow?," *Mater Today Nano*, vol. 9, p. 100058, Mar. 2020, doi: 10.1016/j.mtnano.2019.100058.

[5] K. Liu, B. Ouyang, X. Guo, Y. Guo, and Y. Liu, "Advances in flexible organic field-effect transistors and their applications for flexible electronics," *npj Flexible Electronics*, vol. 6, no. 1, p. 1, Jan. 2022, doi: 10.1038/s41528-022-00133-3.

[6] S. Wang, Z. Shan, and H. Huang, "The Mechanical Properties of Nanowires," *Advanced Science*, vol. 4, no. 4, Apr. 2017, doi: 10.1002/advs.201600332.

[7] W. Lu and C. M. Lieber, "Semiconductor nanowires," *J Phys D Appl Phys*, vol. 39, no. 21, pp. R387–R406, Nov. 2006, doi: 10.1088/0022-3727/39/21/R01.

[8] R. Sondors *et al.*, "Size Distribution, Mechanical and Electrical Properties of CuO Nanowires Grown by Modified Thermal Oxidation Methods," *Nanomaterials*, vol. 10, no. 6, p. 1051, May 2020, doi: 10.3390/nano10061051.

[9] P. Guan *et al.*, "Performance degradation and mitigation strategies of silver nanowire networks: a review," *Critical Reviews in Solid State and Materials Sciences*, vol. 47, no. 3, pp. 435–459, May 2022, doi: 10.1080/10408436.2021.1941753.

[10] H. Li, J. M. Biser, J. T. Perkins, S. Dutta, R. P. Vinci, and H. M. Chan, "Thermal stability of Cu nanowires on a sapphire substrate," *J Appl Phys*, vol. 103, no. 2, Jan. 2008, doi: 10.1063/1.2837053.

[11] M. Byakodi *et al.*, "Emerging 0D, 1D, 2D, and 3D nanostructures for efficient point-of-care biosensing," *Biosens Bioelectron X*, vol. 12, p. 100284, Dec. 2022, doi: 10.1016/j.biosx.2022.100284.

[12] S. A. Afolalu, S. B. Soetan, S. O. Ongbali, A. A. Abioye, and A. S. Oni, "Morphological characterization and physio-chemical properties of nanoparticle – review," *IOP Conf Ser Mater Sci Eng*, vol. 640, no. 1, p. 012065, Nov. 2019, doi: 10.1088/1757-899X/640/1/012065.

[13] N. Joudeh and D. Linke, "Nanoparticle classification, physicochemical properties, characterization, and applications: a comprehensive review for biologists," *J Nanobiotechnology*, vol. 20, no. 1, p. 262, Jun. 2022, doi: 10.1186/s12951-022-01477-8.

[14] M. Velický and R. A. W. Dryfe, "Electrochemistry of 2D nanomaterials," 2021, pp. 485–536. doi: 10.1016/B978-0-12-820055-1.00009-5.

[15] C. Verma, E. Berdimurodov, D. K. Verma, K. Berdimuradov, A. Alfantazi, and C. M. Hussain, “3D Nanomaterials: The future of industrial, biological, and environmental applications,” *Inorg Chem Commun*, vol. 156, p. 111163, Oct. 2023, doi: 10.1016/j.inoche.2023.111163.

[16] A. G. N. Sofiah, M. Samykano, K. Kadirgama, R. V. Mohan, and N. A. C. Lah, “Metallic nanowires: Mechanical properties – Theory and experiment,” *Appl Mater Today*, vol. 11, pp. 320–337, Jun. 2018, doi: 10.1016/j.apmt.2018.03.004.

[17] C.-Y. Hsu *et al.*, “Nanowires Properties and Applications: A Review Study,” *S Afr J Chem Eng*, vol. 46, pp. 286–311, Oct. 2023, doi: 10.1016/j.sajce.2023.08.006.

[18] D. W. Hobson, “Nanotechnology,” in *Comprehensive Biotechnology*, Elsevier, 2011, pp. 683–697. doi: 10.1016/B978-0-08-088504-9.00228-2.

[19] N. P. Dasgupta *et al.*, “25th Anniversary Article: Semiconductor Nanowires – Synthesis, Characterization, and Applications,” *Advanced Materials*, vol. 26, no. 14, pp. 2137–2184, Apr. 2014, doi: 10.1002/adma.201305929.

[20] M. Nehra *et al.*, “1D semiconductor nanowires for energy conversion, harvesting and storage applications,” *Nano Energy*, vol. 76, p. 104991, Oct. 2020, doi: 10.1016/j.nanoen.2020.104991.

[21] Y.-Z. Long, M. Yu, B. Sun, C.-Z. Gu, and Z. Fan, “Recent advances in large-scale assembly of semiconducting inorganic nanowires and nanofibers for electronics, sensors and photovoltaics,” *Chem Soc Rev*, vol. 41, no. 12, p. 4560, 2012, doi: 10.1039/c2cs15335a.

[22] S. Vlassov, S. Oras, B. Polyakov, E. Butanovs, A. Kyritsakis, and V. Zadin, “Kinking in Semiconductor Nanowires: A Review,” *Cryst Growth Des*, vol. 22, no. 1, pp. 871–892, Jan. 2022, doi: 10.1021/acs.cgd.1c00802.

[23] M. Ek and M. A. Filler, “Atomic-Scale Choreography of Vapor–Liquid–Solid Nanowire Growth,” *Acc Chem Res*, vol. 51, no. 1, pp. 118–126, Jan. 2018, doi: 10.1021/acs.accounts.7b00392.

[24] J. G. Lu, P. Chang, and Z. Fan, “Quasi-one-dimensional metal oxide materials—Synthesis, properties and applications,” *Materials Science and Engineering: R: Reports*, vol. 52, no. 1–3, pp. 49–91, May 2006, doi: 10.1016/j.mser.2006.04.002.

[25] B. Alhalaili *et al.*, “Gallium oxide nanowires for UV detection with enhanced growth and material properties,” *Sci Rep*, vol. 10, no. 1, p. 21434, Dec. 2020, doi: 10.1038/s41598-020-78326-x.

[26] M. Higashiwaki, “β-Ga2O3 material properties, growth technologies, and devices: a review,” *AAPPS Bulletin*, vol. 32, no. 1, p. 3, Jan. 2022, doi: 10.1007/s43673-021-00033-0.

[27] E. Butanovs, L. Dipane, A. Zolotarjovs, S. Vlassov, and B. Polyakov, “Preparation of functional Ga2S3 and Ga_2Se_3 shells around Ga_2O_3 nanowires via sulfurization or selenization,” *Opt Mater (Amst)*, vol. 131, p. 112675, Sep. 2022, doi: 10.1016/j.optmat.2022.112675.

[28] S. J. Pearton *et al.*, “A review of Ga_2O_3 materials, processing, and devices,” *Appl Phys Rev*, vol. 5, no. 1, Mar. 2018, doi: 10.1063/1.5006941.

[29] C. Sivakumar, G.-H. Tsai, P.-F. Chung, B. Balraj, Y.-F. Lin, and M.-S. Ho, “High-Quality Single-Crystalline β-Ga_2O_3 Nanowires: Synthesis to Nonvolatile

Memory Applications," *Nanomaterials*, vol. 11, no. 8, p. 2013, Aug. 2021, doi: 10.3390/nano11082013.

[30] B. Alhalaili *et al.*, "Gallium oxide nanowires for UV detection with enhanced growth and material properties," *Sci Rep*, vol. 10, no. 1, p. 21434, Dec. 2020, doi: 10.1038/s41598-020-78326-x.

[31] A.-C. Liu *et al.*, "State-of-the-Art β-Ga 2 O 3 Field-Effect Transistors for Power Electronics," *ACS Omega*, vol. 7, no. 41, pp. 36070–36091, Oct. 2022, doi: 10.1021/acsomega.2c03345.

[32] Y. Li *et al.*, "Efficient Assembly of Bridged β -Ga 2 O 3 Nanowires for Solar-Blind Photodetection," *Adv Funct Mater*, vol. 20, no. 22, pp. 3972–3978, Nov. 2010, doi: 10.1002/adfm.201001140.

[33] D. Guo, Q. Guo, Z. Chen, Z. Wu, P. Li, and W. Tang, "Review of Ga_2O_3-based optoelectronic devices," *Materials Today Physics*, vol. 11, p. 100157, Dec. 2019, doi: 10.1016/j.mtphys.2019.100157.

[34] M. Zhang *et al.*, "β-Ga2O3-Based Power Devices: A Concise Review," *Crystals (Basel)*, vol. 12, no. 3, p. 406, Mar. 2022, doi: 10.3390/cryst12030406.

[35] A. Afzal, "β-Ga_2O_3 nanowires and thin films for metal oxide semiconductor gas sensors: Sensing mechanisms and performance enhancement strategies," *Journal of Materiomics*, vol. 5, no. 4, pp. 542–557, Dec. 2019, doi: 10.1016/j.jmat.2019.08.003.

[36] S. Cui, Z. Mei, Y. Zhang, H. Liang, and X. Du, "Room-Temperature Fabricated Amorphous Ga 2 O 3 High-Response-Speed Solar-Blind Photodetector on Rigid and Flexible Substrates," *Adv Opt Mater*, vol. 5, no. 19, Oct. 2017, doi: 10.1002/adom.201700454.

[37] S. Wang *et al.*, "In situ synthesis of monoclinic β-Ga2O3 nanowires on flexible substrate and solar-blind photodetector," *J Alloys Compd*, vol. 787, pp. 133–139, May 2019, doi: 10.1016/j.jallcom.2019.02.031.

[38] Min-Feng Yu, M. Z. Atashbar, and X. Chen, "Mechanical and electrical characterization of /spl beta/-Ga/sub 2/O/sub 3/ nanostructures for sensing applications," *IEEE Sens J*, vol. 5, no. 1, pp. 20–25, Feb. 2005, doi: 10.1109/JSEN.2004.838669.

[39] M.-S. Jo *et al.*, "Aligned CuO nanowire array for a high performance visible light photodetector," *Sci Rep*, vol. 12, no. 1, p. 2284, Feb. 2022, doi: 10.1038/s41598-022-06031-y.

[40] R. Sondors *et al.*, "Size Distribution, Mechanical and Electrical Properties of CuO Nanowires Grown by Modified Thermal Oxidation Methods," *Nanomaterials*, vol. 10, no. 6, p. 1051, May 2020, doi: 10.3390/nano10061051.

[41] B. Polyakov *et al.*, "In situ measurements of ultimate bending strength of CuO and ZnO nanowires," *Eur Phys J B*, vol. 85, no. 11, p. 366, Nov. 2012, doi: 10.1140/epjb/e2012-30430-6.

[42] B. Polyakov, S. Vlassov, L. M. Dorogin, P. Kulis, I. Kink, and R. Lohmus, "The effect of substrate roughness on the static friction of CuO nanowires," *Surf Sci*, vol. 606, no. 17–18, pp. 1393–1399, Sep. 2012, doi: 10.1016/j.susc.2012.04.029.

[43] H. Sheng *et al.*, “Anelasticity of twinned CuO nanowires,” *Nano Res*, vol. 8, no. 11, pp. 3687–3693, Nov. 2015, doi: 10.1007/s12274-015-0868-x.

[44] S. Lal, J. H. Hafner, N. J. Halas, S. Link, and P. Nordlander, “Noble Metal Nanowires: From Plasmon Waveguides to Passive and Active Devices,” *Acc Chem Res*, vol. 45, no. 11, pp. 1887–1895, Nov. 2012, doi: 10.1021/ar300133j.

[45] M. Antsov *et al.*, “Mechanical characterisation of pentagonal gold nanowires in three different test configurations: A comparative study,” *Micron*, vol. 124, p. 102686, Sep. 2019, doi: 10.1016/j.micron.2019.102686.

[46] J. Cai *et al.*, “SERS hotspots distribution of the highly ordered noble metal arrays on flexible substrates,” *Opt Mater (Amst)*, vol. 122, p. 111779, Dec. 2021, doi: 10.1016/j.optmat.2021.111779.

[47] I. Yoon *et al.*, “Single Nanowire on a Film as an Efficient SERS-Active Platform,” *J Am Chem Soc*, vol. 131, no. 2, pp. 758–762, Jan. 2009, doi: 10.1021/ja807455s.

[48] M. Arefpour, M. Almasi Kashi, F. Khansari Barzoki, M. Noormohammadi, and A. Ramazani, “Electrodeposited metal nanowires as transparent conductive electrodes: Their release conditions, electrical conductivity, optical transparency and chemical stability,” *Mater Des*, vol. 157, pp. 326–336, Nov. 2018, doi: 10.1016/j.matdes.2018.07.048.

[49] X. Lu, Y. Zhang, and Z. Zheng, “Metal-Based Flexible Transparent Electrodes: Challenges and Recent Advances,” *Adv Electron Mater*, vol. 7, no. 5, May 2021, doi: 10.1002/aelm.202001121.

[50] J. Choi, G. Sauer, K. Nielsch, R. B. Wehrspohn, and U. Gösele, “Hexagonally Arranged Monodisperse Silver Nanowires with Adjustable Diameter and High Aspect Ratio,” *Chemistry of Materials*, vol. 15, no. 3, pp. 776–779, Feb. 2003, doi: 10.1021/cm0208758.

[51] S. G. Nuriyeva, H. A. Shirinova, K. M. Hasanov, and F. V. Hajiyeva, “Controlled Synthesis of Silver Nanowires: Production and Characterization,” *Acta Phys Pol A*, vol. 143, no. 4, pp. 279–283, Apr. 2023, doi: 10.12693/APhysPolA.143.279.

[52] C. Celle, C. Mayousse, E. Moreau, H. Basti, A. Carella, and J.-P. Simonato, “Highly flexible transparent film heaters based on random networks of silver nanowires,” *Nano Res*, vol. 5, no. 6, pp. 427–433, Jun. 2012, doi: 10.1007/s12274-012-0225-2.

[53] A. Diaz-Alvarez *et al.*, “Emergent dynamics of neuromorphic nanowire networks,” *Sci Rep*, vol. 9, no. 1, p. 14920, Oct. 2019, doi: 10.1038/s41598-019-51330-6.

[54] H. H. Khaligh and I. A. Goldthorpe, “Failure of silver nanowire transparent electrodes under current flow,” *Nanoscale Res Lett*, vol. 8, no. 1, p. 235, Dec. 2013, doi: 10.1186/1556-276X-8-235.

[55] D. P. Langley *et al.*, “Metallic nanowire networks: effects of thermal annealing on electrical resistance,” *Nanoscale*, vol. 6, no. 22, pp. 13535–13543, 2014, doi: 10.1039/C4NR04151H.

[56] H. Li, J. M. Biser, J. T. Perkins, S. Dutta, R. P. Vinci, and H. M. Chan, “Thermal stability of Cu nanowires on a sapphire substrate,” *J Appl Phys*, vol. 103, no. 2, Jan. 2008, doi: 10.1063/1.2837053.

[57] A. L. Goodwin, "Opportunities and challenges in understanding complex functional materials," *Nat Commun*, vol. 10, no. 1, p. 4461, Oct. 2019, doi: 10.1038/s41467-019-12422-z.

[58] "doitpoms." [Online]. Available: https://www.doitpoms.ac.uk/tlplib/atomic-scale-structure/printall.php

[59] W. D. Callister, *MATERIALS SCIENCE AND ENGINEERING*, 10th ed. Wiley, 2020.

[60] K. L. Duncan, Y. Wang, S. R. Bishop, F. Ebrahimi, and E. D. Wachsman, "Role of Point Defects in the Physical Properties of Fluorite Oxides," *Journal of the American Ceramic Society*, vol. 89, no. 10, pp. 3162–3166, Oct. 2006, doi: 10.1111/j.1551-2916.2006.01193.x.

[61] J. Xi, P. Zhang, C. He, H. Zang, D. Guo, and T. Li, "The role of point defects in the swelling and elastic modulus of irradiated cubic silicon carbide," *Nucl Instrum Methods Phys Res B*, vol. 356–357, pp. 62–68, Aug. 2015, doi: 10.1016/j.nimb.2015.04.059.

[62] L. Li, Z. Zhang, P. Zhang, and Z. Zhang, "A review on the fatigue cracking of twin boundaries: Crystallographic orientation and stacking fault energy," *Prog Mater Sci*, vol. 131, p. 101011, Jan. 2023, doi: 10.1016/j.pmatsci.2022.101011.

[63] R. Su *et al.*, "The influence of stacking faults on mechanical behavior of advanced materials," *Materials Science and Engineering: A*, vol. 803, p. 140696, Jan. 2021, doi: 10.1016/j.msea.2020.140696.

[64] Y. Li, Y. Wang, S. Ryu, A. F. Marshall, W. Cai, and P. C. McIntyre, "Spontaneous, Defect-Free Kinking via Capillary Instability during Vapor–Liquid–Solid Nanowire Growth," *Nano Lett*, vol. 16, no. 3, pp. 1713–1718, Mar. 2016, doi: 10.1021/acs.nanolett.5b04633.

[65] Z. He, H. T. Nguyen, L. Duc Toan, and D. Pribat, "A detailed study of kinking in indium-catalyzed silicon nanowires," *CrystEngComm*, vol. 17, no. 33, pp. 6286–6296, 2015, doi: 10.1039/C5CE00773A.

[66] S. Vlassov *et al.*, "Reshaping Covalent Nanowires by Exploiting an Unexpected Plasticity Mediated by Deformation Twinning," *Small*, vol. 20, no. 1, Jan. 2024, doi: 10.1002/smll.202304614.

[67] M. Paladugu *et al.*, "Novel Growth Phenomena Observed in Axial InAs/GaAs Nanowire Heterostructures," *Small*, vol. 3, no. 11, pp. 1873–1877, Nov. 2007, doi: 10.1002/smll.200700222.

[68] H. Zhao, A. S. Eggeman, C. P. Race, and B. Derby, "Geometrical constraints on the bending deformation of Penta-twinned silver nanowires," *Acta Mater*, vol. 185, pp. 110–118, Feb. 2020, doi: 10.1016/j.actamat.2019.11.058.

[69] S. Lee *et al.*, "Reversible cyclic deformation mechanism of gold nanowires by twinning–detwinning transition evidenced from in situ TEM," *Nat Commun*, vol. 5, no. 1, p. 3033, Jan. 2014, doi: 10.1038/ncomms4033.

[70] Y. Chen, X. An, and X. Liao, "Mechanical behaviors of nanowires," *Appl Phys Rev*, vol. 4, no. 3, p. 031104, Sep. 2017, doi: 10.1063/1.4989649.

[71] F. Östlund *et al.*, "Brittle-to-Ductile Transition in Uniaxial Compression of Silicon Pillars at Room Temperature," *Adv Funct Mater*, vol. 19, no. 15, pp. 2439–2444, Aug. 2009, doi: 10.1002/adfm.200900418.

[72] Y. Wu, Q. Rao, J. P. Best, D. Mu, X. Xu, and H. Huang, "Superior Room Temperature Compressive Plasticity of Submicron Beta-Phase Gallium Oxide Single Crystals," *Adv Funct Mater*, vol. 32, no. 48, Nov. 2022, doi: 10.1002/adfm.202207960.

[73] F. Mignerot, B. Kedjar, H. Bahsoun, and L. Thilly, "Size-induced twinning in InSb semiconductor during room temperature deformation," *Sci Rep*, vol. 11, no. 1, p. 19441, Oct. 2021, doi: 10.1038/s41598-021-98492-w.

[74] Q. Wu, W. Miao, Y. Zhang, H. Gao, and D. Hui, "Mechanical properties of nanomaterials: A review," *Nanotechnol Rev*, vol. 9, no. 1, pp. 259–273, Mar. 2020, doi: 10.1515/ntrev-2020-0021.

[75] A. Reghunadhan, N. Kalarikkal, and S. Thomas, "Mechanical Property Analysis of Nanomaterials," in *Characterization of Nanomaterials*, Elsevier, 2018, pp. 191–212. doi: 10.1016/B978-0-08-101973-3.00007-9.

[76] S. Cui, Z. Mei, Y. Zhang, H. Liang, and X. Du, "Room-Temperature Fabricated Amorphous Ga 2 O 3 High-Response-Speed Solar-Blind Photodetector on Rigid and Flexible Substrates," *Adv Opt Mater*, vol. 5, no. 19, Oct. 2017, doi: 10.1002/adom.201700454.

[77] S. Wang *et al.*, "In situ synthesis of monoclinic β-Ga2O3 nanowires on flexible substrate and solar-blind photodetector," *J Alloys Compd*, vol. 787, pp. 133–139, May 2019, doi: 10.1016/j.jallcom.2019.02.031.

[78] X.-Q. Zheng, H. Zhao, Z. Jia, X. Tao, and P. X.-L. Feng, "Young's modulus and corresponding orientation in β-Ga2O3 thin films resolved by nanomechanical resonators," *Appl Phys Lett*, vol. 119, no. 1, Jul. 2021, doi: 10.1063/5.0050421.

[79] S. Vlassov *et al.*, "Critical review on experimental and theoretical studies of elastic properties of wurtzite-structured ZnO nanowires," *Nanotechnol Rev*, vol. 12, no. 1, Feb. 2023, doi: 10.1515/ntrev-2022-0505.

[80] P. Zhou, C. Wu, and X. Li, "Three-point bending Young's modulus of nanowires," *Meas Sci Technol*, vol. 19, no. 11, p. 115703, Nov. 2008, doi: 10.1088/0957-0233/19/11/115703.

[81] B. R. Neugirg, S. R. Koebley, H. C. Schniepp, and A. Fery, "AFM-based mechanical characterization of single nanofibres," *Nanoscale*, vol. 8, no. 16, pp. 8414–8426, 2016, doi: 10.1039/C6NR00863A.

[82] N. Wu, L. Chen, Q. Wei, Q. Liu, and J. Li, "Nanoscale three-point bending of single polymer/inorganic composite nanofiber," *Journal of the Textile Institute*, vol. 103, no. 2, pp. 154–158, Feb. 2012, doi: 10.1080/00405000.2011.557187.

[83] L. Jasulaneca *et al.*, "Determination of Young's modulus of Sb 2 S 3 nanowires by in situ resonance and bending methods," *Beilstein Journal of Nanotechnology*, vol. 7, pp. 278–283, Feb. 2016, doi: 10.3762/bjnano.7.25.

[84] S. J. Marshall, S. C. Bayne, R. Baier, A. P. Tomsia, and G. W. Marshall, "A review of adhesion science," *Dental Materials*, vol. 26, no. 2, pp. e11–e16, Feb. 2010, doi: 10.1016/j.dental.2009.11.157.

[85] B. Polyakov *et al.*, "Some aspects of formation and tribological properties of silver nanodumbbells," *Nanoscale Res Lett*, vol. 9, no. 1, p. 186, Dec. 2014, doi: 10.1186/1556-276X-9-186.

[86] A. Trausa *et al.*, "Heat-Induced Fragmentation and Adhesive Behaviour of Gold Nanowires for Surface-Enhanced Raman Scattering Substrates," *ChemEngineering*, vol. 8, no. 1, p. 15, Jan. 2024, doi: 10.3390/chemengineering 8010015.

[87] P. Wang *et al.*, "The Evolution of Flexible Electronics: From Nature, Beyond Nature, and To Nature," *Advanced Science*, vol. 7, no. 20, Oct. 2020, doi: 10.1002/ advs.202001116.

[88] S. Vlassov *et al.*, "Adhesion and Mechanical Properties of PDMS-Based Materials Probed with AFM: A Review," *REVIEWS ON ADVANCED MATERIALS SCIENCE*, vol. 56, no. 1, pp. 62–78, May 2018, doi: 10.1515/rams-2018-0038.

[89] G. Guisbiers, "Advances in thermodynamic modelling of nanoparticles," *Adv Phys X*, vol. 4, no. 1, p. 1668299, Jan. 2019, doi: 10.1080/23746149.2019.1668299.

[90] M. A. Jabbareh, "A unified bond energy model for size-dependent melting temperature of freestanding and embedded nanomaterials," *Solid State Commun*, vol. 355, p. 114923, Nov. 2022, doi: 10.1016/j.ssc.2022.114923.

[91] B. Polyakov *et al.*, "Comparison of the resistivities of nanostructured films made from silver, copper-silver and copper nanoparticle and nanowire suspensions," *Thin Solid Films*, vol. 784, p. 140087, Nov. 2023, doi: 10.1016/j.tsf.2023.140087.

[92] S. Vigonski *et al.*, "Au nanowire junction breakup through surface atom diffusion," *Nanotechnology*, vol. 29, no. 1, p. 015704, Jan. 2018, doi: 10.1088/ 1361-6528/aa9a1b.

[93] M. E. Toimil Molares, A. G. Balogh, T. W. Cornelius, R. Neumann, and C. Trautmann, "Fragmentation of nanowires driven by Rayleigh instability," *Appl Phys Lett*, vol. 85, no. 22, pp. 5337–5339, Nov. 2004, doi: 10.1063/1.1826237.

[94] S. Oras *et al.*, "The effect of heat treatment on the morphology and mobility of Au nanoparticles," *Beilstein Journal of Nanotechnology*, vol. 11, pp. 61–67, Jan. 2020, doi: 10.3762/bjnano.11.6.

[95] H. Oh, J. Lee, and M. Lee, "Transformation of silver nanowires into nanoparticles by Rayleigh instability: Comparison between laser irradiation and heat treatment," *Appl Surf Sci*, vol. 427, pp. 65–73, Jan. 2018, doi: 10.1016/j. apsusc.2017.08.102.

[96] A. H. Zewail, "Four-Dimensional Electron Microscopy," *Science (1979)*, vol. 328, no. 5975, pp. 187–193, Apr. 2010, doi: 10.1126/science.1166135.

[97] D. Ganten et al., *Encyclopedic Reference of Genomics and Proteomics in Molecular Medicine*. Springer, 2006.

[98] K. Akhtar, S. A. Khan, S. B. Khan, and A. M. Asiri, "Scanning Electron Microscopy: Principle and Applications in Nanomaterials Characterization," in *Handbook of Materials Characterization*, Cham: Springer International Publishing, 2018, pp. 113–145. doi: 10.1007/978-3-319-92955-2_4.

[99] A. Alyamani and O. M. Lemine, "FE-SEM Characterization of Some Nanomaterial," in *Scanning Electron Microscopy*, InTech, 2012. doi: 10.5772/34361.

[100] R. F. Egerton, P. Li, and M. Malac, "Radiation damage in the TEM and SEM," *Micron*, vol. 35, no. 6, pp. 399–409, Aug. 2004, doi: 10.1016/j.micron.2004.02.003.

[101] M. Ezzahmouly *et al.*, "Micro-computed tomographic and SEM study of porous bioceramics using an adaptive method based on the mathematical

morphological operations," *Heliyon*, vol. 5, no. 12, p. e02557, Dec. 2019, doi: 10.1016/j.heliyon.2019.e02557.

[102] Hui Xie and S. Régnier, "Development of a Flexible Robotic System for Multiscale Applications of Micro/Nanoscale Manipulation and Assembly," *IEEE/ASME Transactions on Mechatronics*, vol. 16, no. 2, pp. 266–276, Apr. 2011, doi: 10.1109/TMECH.2010.2040483.

[103] S. Vlassov *et al.*, "Real-time manipulation of gold nanoparticles inside a scanning electron microscope," *Solid State Commun*, vol. 151, no. 9, pp. 688–692, May 2011, doi: 10.1016/j.ssc.2011.02.020.

[104] A. I. Denisyuk, A. V. Krasavin, F. E. Komissarenko, and I. S. Mukhin, "Mechanical, Electrostatic, and Electromagnetic Manipulation of Microobjects and Nanoobjects in Electron Microscopes," 2014, pp. 101–140. doi: 10.1016/B978-0-12-800264-3.00003-4.

[105] D. Dietzel *et al.*, "Interfacial friction obtained by lateral manipulation of nanoparticles using atomic force microscopy techniques," *J Appl Phys*, vol. 102, no. 8, Oct. 2007, doi: 10.1063/1.2798628.

[106] S. Rozhok and V. Chandrasekhar, "Application of commercially available cantilevers in tuning fork Scanning Probe Microscopy (SPM) studies," *Solid State Commun*, vol. 121, no. 12, pp. 683–686, Mar. 2002, doi: 10.1016/S0038-1098(02)00035-2.

[107] R. T. Emelyanov, A. S. Klimov, I. B. Olenev, E. S. Turysheva, and A. I. Avlasevich, "Investigation of the dynamics of the manipulator drive with a stepper motor," *J Phys Conf Ser*, vol. 1515, no. 4, p. 042043, Apr. 2020, doi: 10.1088/1742-6596/1515/4/042043.

[108] A. P. Prokopev, V. I. Ivanchura, and R. T. Emelyanov, "Study of the Dynamics of the Object Control System of Second Order with Respect to the Placements of the Real Poles," *Journal of Siberian Federal University. Engineering & Technologies*, vol. 11, no. 5, pp. 500–511, Aug. 2018, doi: 10.17516/1999-494X-0049.

[109] J. W. Judy, D. L. Polla, and W. P. Robbins, "A linear piezoelectric stepper motor with submicrometer step size and centimeter travel range," *IEEE Trans Ultrason Ferroelectr Freq Control*, vol. 37, no. 5, pp. 428–437, Sep. 1990, doi: 10.1109/58.105249.

[110] Y. Hu, S. Lin, J. Ma, Y. Zhang, J. Li, and J. Wen, "Piezoelectric inertial rotary actuator operating in two-step motion mode for eliminating backward motion," *Appl Phys Lett*, vol. 117, no. 3, Jul. 2020, doi: 10.1063/5.0012132.

[111] S. Vlassov *et al.*, "Reshaping Covalent Nanowires by Exploiting an Unexpected Plasticity Mediated by Deformation Twinning," *Small*, vol. 20, no. 1, Jan. 2024, doi: 10.1002/smll.202304614.

[112] "Proquest." [Online]. Available: https://www.proquest.com/openview/cf19b23a715dce8c8a0d36bb599a5785/1?pq-origsite=gscholar&cbl=18750

[113] R. Lin *et al.*, "Equivalent Electromechanical Model for Quartz Tuning Fork Used in Atomic Force Microscopy," *Sensors*, vol. 23, no. 8, p. 3923, Apr. 2023, doi: 10.3390/s23083923.

[114] J.-O. Abrahamians, L. Pham Van, and S. Régnier, "Contributed Review: Quartz force sensing probes for micro-applications," *Review of Scientific Instruments*, vol. 87, no. 7, Jul. 2016, doi: 10.1063/1.4958896.

[115] F. J. Giessibl, "High-speed force sensor for force microscopy and profilometry utilizing a quartz tuning fork," *Appl Phys Lett*, vol. 73, no. 26, pp. 3956–3958, Dec. 1998, doi: 10.1063/1.122948.

[116] D. Kajfez, "Q -Factor," in *Encyclopedia of RF and Microwave Engineering*, Wiley, 2005. doi: 10.1002/0471654507.eme333.

[117] T. Akiyama, U. Staufer, N. F. de Rooij, P. Frederix, and A. Engel, "Symmetrically arranged quartz tuning fork with soft cantilever for intermittent contact mode atomic force microscopy," *Review of Scientific Instruments*, vol. 74, no. 1, pp. 112–117, Jan. 2003, doi: 10.1063/1.1523631.

[118] T. Akiyama, U. Staufer, and N. F. de Rooij, "Self-sensing and self-actuating probe based on quartz tuning fork combined with microfabricated cantilever for dynamic mode atomic force microscopy," *Appl Surf Sci*, vol. 210, no. 1–2, pp. 18–21, Mar. 2003, doi: 10.1016/S0169-4332(02)01471-X.

[119] S. Stucklin, M. R. Gullo, T. Akiyama, and M. Scheidiger, "Atomic force microscopy for industry with the Akiyama-Probe sensor," in *2008 International Conference on Nanoscience and Nanotechnology*, IEEE, Feb. 2008, pp. 79–82. doi: 10.1109/ICONN.2008.4639250.

[120] R. F. Egerton, "The Transmission Electron Microscope," in *Physical Principles of Electron Microscopy*, Cham: Springer International Publishing, 2016, pp. 55–88. doi: 10.1007/978-3-319-39877-8_3.

[121] C. B. Carter and D. B. Williams, *Transmission Electron Microscopy;* Springer International Publishing, 2016.

[122] D. Ananthapadmanaban, "Summary of Some Selected Characterization Methods of Geopolymers," in *Geopolymers and Other Geosynthetics*, IntechOpen, 2020. doi: 10.5772/intechopen.82208.

[123] Q. Lin, X. An, H. Liu, Q. Tang, P. Dai, and X. Liao, "In-situ high-resolution transmission electron microscopy investigation of grain boundary dislocation activities in a nanocrystalline CrMnFeCoNi high-entropy alloy," *J Alloys Compd*, vol. 709, pp. 802–807, Jun. 2017, doi: 10.1016/j.jallcom.2017.03.194.

[124] A. C. Y. Liu, R. Arenal, and G. Montagnac, "In situ transmission electron microscopy observation of keV-ion irradiation of single-walled carbon and boron nitride nanotubes," *Carbon N Y*, vol. 62, pp. 248–255, Oct. 2013, doi: 10.1016/j.carbon.2013.05.062.

[125] C. Zhang, K. L. Firestein, J. F. S. Fernando, D. Siriwardena, J. E. von Treifeldt, and D. Golberg, "Recent Progress of In Situ Transmission Electron Microscopy for Energy Materials," *Advanced Materials*, vol. 32, no. 18, May 2020, doi: 10.1002/adma.201904094.

[126] D. Johnson, N. Hilal, and W. R. Bowen, "Basic Principles of Atomic Force Microscopy," in *Atomic Force Microscopy in Process Engineering*, Elsevier, 2009, pp. 1–30. doi: 10.1016/B978-1-85617-517-3.00001-8.

[127] Y. F. Dufrêne *et al.*, "Imaging modes of atomic force microscopy for application in molecular and cell biology," *Nat Nanotechnol*, vol. 12, no. 4, pp. 295–307, Apr. 2017, doi: 10.1038/nnano.2017.45.

[128] A. A. G. Requicha *et al.*, "Manipulation of nanoscale components with the AFM: principles and applications," in *Proceedings of the 2001 1st IEEE Conference on Nanotechnology. IEEE-NANO 2001 (Cat. No.01EX516)*, IEEE, pp. 81–86. doi: 10.1109/NANO.2001.966398.

[129] N. Wang and X. Zhao, "Atomic Force Microscopy – A Powerful Tool for Studying Contact Electrification," *Adv Mater Technol*, vol. 8, no. 6, Mar. 2023, doi: 10.1002/admt.202201408.

[130] S. Vlassov *et al.*, "Adhesion and Mechanical Properties of PDMS-Based Materials Probed with AFM: A Review," *REVIEWS ON ADVANCED MATERIALS SCIENCE*, vol. 56, no. 1, pp. 62–78, May 2018, doi: 10.1515/rams-2018-0038.

[131] S. Santos *et al.*, "Advances in dynamic AFM: From nanoscale energy dissipation to material properties in the nanoscale," *J Appl Phys*, vol. 129, no. 13, Apr. 2021, doi: 10.1063/5.0041366.

[132] R. García, N. F. Martínez, C. J. Gómez, and A. García-Martín, "Energy Dissipation and Nanoscale Imaging in Tapping Mode AFM," 2007, pp. 361–371. doi: 10.1007/978-3-540-36807-6_17.

[133] X. D. Bai, P. X. Gao, Z. L. Wang, and E. G. Wang, "Dual-mode mechanical resonance of individual ZnO nanobelts," *Appl Phys Lett*, vol. 82, no. 26, pp. 4806–4808, Jun. 2003, doi: 10.1063/1.1587878.

[134] P. Zhou, C. Wu, and X. Li, "Three-point bending Young's modulus of nanowires," *Meas Sci Technol*, vol. 19, no. 11, p. 115703, Nov. 2008, doi: 10.1088/0957-0233/19/11/115703.

[135] B. Polyakov *et al.*, "Mechanical properties of sol–gel derived SiO 2 nanotubes," *Beilstein Journal of Nanotechnology*, vol. 5, pp. 1808–1814, Oct. 2014, doi: 10.3762/bjnano.5.191.

[136] B. Anczykowski, B. Gotsmann, H. Fuchs, J. P. Cleveland, and V. B. Elings, "How to measure energy dissipation in dynamic mode atomic force microscopy," *Appl Surf Sci*, vol. 140, no. 3–4, pp. 376–382, Feb. 1999, doi: 10.1016/S0169-4332(98)00558-3.

[137] S. He *et al.*, "Au-on-Ag nanostructure for in-situ SERS monitoring of catalytic reactions," *Nanotechnology*, vol. 33, no. 15, p. 155701, Apr. 2022, doi: 10.1088/1361-6528/ac47d2.

[138] E. Damerchi *et al.*, "Heat-induced morphological changes in silver nanowires deposited on a patterned silicon substrate," *Beilstein Journal of Nanotechnology*, vol. 15, pp. 435–446, Apr. 2024, doi: 10.3762/bjnano.15.39.

[139] F. Mignerot, B. Kedjar, H. Bahsoun, and L. Thilly, "Size-induced twinning in InSb semiconductor during room temperature deformation," *Sci Rep*, vol. 11, no. 1, p. 19441, Oct. 2021, doi: 10.1038/s41598-021-98492-w.

[140] P. Uttam, V. Kumar, K.-H. Kim, and A. Deep, "Nanotwinning: Generation, properties, and application," *Mater Des*, vol. 192, p. 108752, Jul. 2020, doi: 10.1016/j.matdes.2020.108752.

[141] B. Tian, P. Xie, T. J. Kempa, D. C. Bell, and C. M. Lieber, "Single-crystalline kinked semiconductor nanowire superstructures," *Nat Nanotechnol*, vol. 4, no. 12, pp. 824–829, Dec. 2009, doi: 10.1038/nnano.2009.304.

[142] Z. Jiang, Q. Qing, P. Xie, R. Gao, and C. M. Lieber, "Kinked p–n Junction Nanowire Probes for High Spatial Resolution Sensing and Intracellular Recording," *Nano Lett*, vol. 12, no. 3, pp. 1711–1716, Mar. 2012, doi: 10.1021/nl300256r.

[143] L. Gan, M. Liao, H. Li, Y. Ma, and T. Zhai, "Geometry-induced high performance ultraviolet photodetectors in kinked SnO 2 nanowires," *J Mater Chem C Mater*, vol. 3, no. 32, pp. 8300–8306, 2015, doi: 10.1039/C5TC01178G.

[144] J.-W. Jiang and T. Rabczuk, "Mechanical oscillation of kinked silicon nanowires: A natural nanoscale spring," *Appl Phys Lett*, vol. 102, no. 12, Mar. 2013, doi: 10.1063/1.4799029.

[145] J.-W. Jiang, J.-H. Zhao, and T. Rabczuk, "Size-sensitive Young's modulus of kinked silicon nanowires," *Nanotechnology*, vol. 24, no. 18, p. 185702, May 2013, doi: 10.1088/0957-4484/24/18/185702.

[146] Y. Jing, C. Zhang, Y. Liu, L. Guo, and Q. Meng, "Mechanical properties of kinked silicon nanowires," *Physica B Condens Matter*, vol. 462, pp. 59–63, Apr. 2015, doi: 10.1016/j.physb.2015.01.018.

[147] X. Zou, D. Xie, Y. Sun, and C. Wang, "Nanowires mediated growth of β-Ga2O3 nanobelts for high-temperature (> 573 K) solar-blind photodetectors," *Nano Res*, vol. 16, no. 4, pp. 5548–5554, Apr. 2023, doi: 10.1007/s12274-022-5243-0.

[148] X.-Q. Zheng, H. Zhao, Z. Jia, X. Tao, and P. X.-L. Feng, "Young's modulus and corresponding orientation in β-Ga2O3 thin films resolved by nanomechanical resonators," *Appl Phys Lett*, vol. 119, no. 1, Jul. 2021, doi: 10.1063/5.0050421.

[149] A. S. Grashchenko, S. A. Kukushkin, V. I. Nikolaev, A. V. Osipov, E. V. Osipova, and I. P. Soshnikov, "Study of the Anisotropic Elastoplastic Properties of β-Ga2O3 Films Synthesized on SiC/Si Substrates," *Physics of the Solid State*, vol. 60, no. 5, pp. 852–857, May 2018, doi: 10.1134/S1063783418050104.

[150] Y. Yao, Y. Sugawara, K. Sasaki, A. Kuramata, and Y. Ishikawa, "Anisotropic mechanical properties of β-Ga2O3 single-crystal measured via angle-dependent nanoindentation using a Berkovich indenter," *J Appl Phys*, vol. 134, no. 21, Dec. 2023, doi: 10.1063/5.0180389.

[151] M. Nasr Esfahani and B. E. Alaca, "A Review on Size-Dependent Mechanical Properties of Nanowires," *Adv Eng Mater*, vol. 21, no. 8, Aug. 2019, doi: 10.1002/adem.201900192.

[152] J. Kosmaca *et al.*, "Young's modulus and indirect morphological analysis of Bi 2 Se 3 nanoribbons by resonance measurements," *Nanotechnology*, vol. 28, no. 32, p. 325701, Aug. 2017, doi: 10.1088/1361-6528/aa79cd.

[153] S. Vlassov *et al.*, "Critical review on experimental and theoretical studies of elastic properties of wurtzite-structured ZnO nanowires," *Nanotechnol Rev*, vol. 12, no. 1, Feb. 2023, doi: 10.1515/ntrev-2022-0505.

[154] S. Vlassov *et al.*, "Complex tribomechanical characterization of ZnO nanowires: nanomanipulations supported by FEM simulations," *Nanotechnology*, vol. 27, no. 33, p. 335701, Aug. 2016, doi: 10.1088/0957-4484/27/33/335701.

[155] S. Wang, Z. Shan, and H. Huang, “The Mechanical Properties of Nanowires,” *Advanced Science*, vol. 4, no. 4, Apr. 2017, doi: 10.1002/advs.201600332.

[156] K. L. Duncan, Y. Wang, S. R. Bishop, F. Ebrahimi, and E. D. Wachsman, “Role of Point Defects in the Physical Properties of Fluorite Oxides,” *Journal of the American Ceramic Society*, vol. 89, no. 10, pp. 3162–3166, Oct. 2006, doi: 10.1111/j.1551-2916.2006.01193.x.

[157] J. Xi, P. Zhang, C. He, H. Zang, D. Guo, and T. Li, “The role of point defects in the swelling and elastic modulus of irradiated cubic silicon carbide,” *Nucl Instrum Methods Phys Res B*, vol. 356–357, pp. 62–68, Aug. 2015, doi: 10.1016/j.nimb.2015.04.059.

[158] X. Wang *et al.*, “Growth Conditions Control the Elastic and Electrical Properties of ZnO Nanowires,” *Nano Lett*, vol. 15, no. 12, pp. 7886–7892, Dec. 2015, doi: 10.1021/acs.nanolett.5b02852.

[159] S. Wang, Q. Huang, Y. Wu, and H. Huang, “Unique structure and surface-related elastic modulus of alumina nanobelts,” *Nanotechnology*, vol. 27, no. 47, p. 475701, Nov. 2016, doi: 10.1088/0957-4484/27/47/475701.

[160] E. Butanovs, M. Zubkins, R. Nedzinskas, V. Zadin, and B. Polyakov, “Comparison of two methods for one-dimensional Ga2O3-ZnGa2O4 core–shell heterostructure synthesis,” *J Cryst Growth*, vol. 618, p. 127319, Sep. 2023, doi: 10.1016/j.jcrysgro.2023.127319.

[161] S. Dai *et al.*, “Elastic Properties of GaN Nanowires: Revealing the Influence of Planar Defects on Young’s Modulus at Nanoscale,” *Nano Lett*, vol. 15, no. 1, pp. 8–15, Jan. 2015, doi: 10.1021/nl501986d.

[162] K. H. Liu, W. L. Wang, Z. Xu, L. Liao, X. D. Bai, and E. G. Wang, “In situ probing mechanical properties of individual tungsten oxide nanowires directly grown on tungsten tips inside transmission electron microscope,” *Appl Phys Lett*, vol. 89, no. 22, Nov. 2006, doi: 10.1063/1.2397547.

[163] H. Ni and X. D. Li, “Synthesis, Structural and Mechanical Characterization of Amorphous and Crystalline Boron Nanobelts,” *Journal of Nano Research*, vol. 1, pp. 10–22, Jan. 2008, doi: 10.4028/www.scientific.net/JNanoR.1.10.

[164] M. Lucas, W. Mai, R. Yang, Z. L. Wang, and E. Riedo, “Aspect Ratio Dependence of the Elastic Properties of ZnO Nanobelts,” *Nano Lett*, vol. 7, no. 5, pp. 1314–1317, May 2007, doi: 10.1021/nl070310g.

[165] B. Andreiuk *et al.*, “Design and synthesis of gold nanostars-based SERS nanotags for bioimaging applications,” *Nanotheranostics*, vol. 6, no. 1, pp. 10–30, 2022, doi: 10.7150/ntno.61244.

[166] A. C. Marques *et al.*, “Bottom-up microwave-assisted seed-mediated synthesis of gold nanoparticles onto nanocellulose to boost stability and high performance for SERS applications,” *Appl Surf Sci*, vol. 561, p. 150060, Sep. 2021, doi: 10.1016/j.apsusc.2021.150060.

[167] A. Kapara, V. Brunton, D. Graham, and K. Faulds, “Investigation of cellular uptake mechanism of functionalised gold nanoparticles into breast cancer using SERS,” *Chem Sci*, vol. 11, no. 22, pp. 5819–5829, 2020, doi: 10.1039/D0SC01255F.

[168] A. K. Pathak, A. B. M. Rahman, V. K. Singh, and S. Kumari, "Sensitivity Enhancement of a Concave Shaped Optical Fiber Refractive Index Sensor Covered with Multiple Au Nanowires," *Sensors*, vol. 19, no. 19, p. 4210, Sep. 2019, doi: 10.3390/s19194210.

[169] O. Inal, U. Badilli, A. S. Ozkan, and F. Mollarasouli, "Bioactive hybrid nanowires for drug delivery," in *Hybrid Nanomaterials for Drug Delivery*, Elsevier, 2022, pp. 269–301. doi: 10.1016/B978-0-323-85754-3.00012-5.

[170] A. Jakhmola *et al.*, "Sustainable synthesis and theoretical studies of polyhedral gold nanoparticles displaying high SERS activity, NIR absorption, and cellular uptake," *Mater Today Chem*, vol. 26, p. 101016, Dec. 2022, doi: 10.1016/j.mtchem.2022.101016.

[171] X. X. Han, R. S. Rodriguez, C. L. Haynes, Y. Ozaki, and B. Zhao, "Surface-enhanced Raman spectroscopy," *Nature Reviews Methods Primers*, vol. 1, no. 1, p. 87, Jan. 2022, doi: 10.1038/s43586-021-00083-6.

[172] H.-L. Wang, E.-M. You, R. Panneerselvam, S.-Y. Ding, and Z.-Q. Tian, "Advances of surface-enhanced Raman and IR spectroscopies: from nano/microstructures to macro-optical design," *Light Sci Appl*, vol. 10, no. 1, p. 161, Aug. 2021, doi: 10.1038/s41377-021-00599-2.

[173] F. Benz *et al.*, "SERS of Individual Nanoparticles on a Mirror: Size Does Matter, but so Does Shape," *J Phys Chem Lett*, vol. 7, no. 12, pp. 2264–2269, Jun. 2016, doi: 10.1021/acs.jpclett.6b00986.

[174] S. Vlassov, M. Mets, B. Polyakov, J. Bian, L. Dorogin, and V. Zadin, "Abrupt elastic-to-plastic transition in pentagonal nanowires under bending," *Beilstein Journal of Nanotechnology*, vol. 10, pp. 2468–2476, Dec. 2019, doi: 10.3762/bjnano.10.237.

[175] S. Vlassov, S. Oras, M. Antsov, J. Butikova, R. Lõhmus, and B. Polyakov, "Low-friction nanojoint prototype," *Nanotechnology*, vol. 29, no. 19, p. 195707, May 2018, doi: 10.1088/1361-6528/aab163.

[176] S. Vigonski *et al.*, "Au nanowire junction breakup through surface atom diffusion," *Nanotechnology*, vol. 29, no. 1, p. 015704, Jan. 2018, doi: 10.1088/1361-6528/aa9a1b.

[177] M. E. Toimil Molares, A. G. Balogh, T. W. Cornelius, R. Neumann, and C. Trautmann, "Fragmentation of nanowires driven by Rayleigh instability," *Appl Phys Lett*, vol. 85, no. 22, pp. 5337–5339, Nov. 2004, doi: 10.1063/1.1826237.

[178] J.-H. Kim, J. Ma, S. Jo, S. Lee, and C. S. Kim, "Enhancement of Antibacterial Performance of Silver Nanowire Transparent Film by Post-Heat Treatment," *Nanomaterials*, vol. 10, no. 5, p. 938, May 2020, doi: 10.3390/nano10050938.

ACKNOWLEDGEMENTS

I would like to express my sincere gratitude to the following people for their invaluable support and contributions to this Dissertation:

My supervisor Dr. Edgars Butanovs, for his endless support, insightful discussions, valuable suggestions, and understanding. His guidance has been essential throughout this journey.

Dr. Boris Polyakov, for generously sharing his expertise and knowledge of the techniques used in this Dissertation. His example as a curious and dedicated scientist has been truly inspiring.

Dr. Krišjānis Šmits, for his support throughout my doctoral studies.

Dr. Andris Anspoks, for his belief in me and support.

Dr. Sergei Vlassov, for his ideas and discussions. I am truly grateful for his inspiration and contributions to my research. He will be dearly missed.

Dr. Sven Oras, for his collaborative work on AFM experiments and PhD-related memes.

Elyad Damerchi, for his support with experimental data.

Special thanks to Dr. Tauno Tiirats, Prof. Veronika Zadin, and Dr. Andreas Kyritsakis for their contributions to MD modelling and fruitful discussions.

Čiro Federiko Tipaldi, for his assistance with Raman measurements.

My colleagues and work-friends Līga Ignatāne, Edgars Vanags, Reinis Ignatāns, Kārlis Vilks, Kevon Kadiwala, and Aleksejs Zolotarjovs, for scientific discussions and emotional support.

My mother Sandra Šagarova and stepfather Aleksandrs Šagarovs, for their love, care and efforts to understand and support my academic pursuits.

In loving memory of my father, Normunds Trauss, whose endless curiosity influenced me as a child. Though he's not here to see my achievements, his adventurous spirit remains alive in me.

My friends Paula Zariņa-Šteinerte, Laura Mežule, Armands Eglītis, Līga Jasulaņeca and Ieva Rotkovska, for their unwavering support and encouragement throughout this journey. Their friendship has been a source of strength.

I would like to acknowledge financial support from European Regional Development Fund projects No. 1.1.1.1/21/A/053 and No. 1.1.1.1/21/A/055, European Union's Horizon 2020 Framework Programme H2020-WIDESPREAD-01-2016-2017-TeamingPhase2 under grant agreement No. 739508, project CAMART^2.